Energy of the Quasi-free Electron in Repulsive Atomic and Molecular Fluids

by

Yevgeniy Lushtak

A dissertation submitted to the Graduate Faculty in Chemistry
in partial fulfillment of the requirements
for the degree of Doctor of Philosophy,
The City University of New York.

2013

This manuscript has been read and accepted for the
Graduate Faculty in Chemistry in satisfaction of the
dissertation requirements for the degree of Doctor of Philosophy.

Date

Dr. Cherice M. Evans,
Chair of Examining Committee

Date

Dr. Maria C. Tamargo,
Executive Officer

Dr. Gary L. Findley

Dr. Lawrence W. Johnson

Dr. Jianbo Liu
Supervisory Committee

THE CITY UNIVERSITY OF NEW YORK

Abstract

Energy of the Quasi-free Electron in Repulsive Atomic and Molecular Fluids

by

Yevgeniy Lushtak

Advisor: Dr. Cherice M. Evans

The ability to predict accurately the energy $V_0(\rho)$ of the quasi-free electron along the entire density (ρ) range of a supercritical fluid has applications in determining the ideal thermodynamic conditions for chemical reactions involving charged species. The previously established field ionization method of extracting $V_0(\rho)$ from the fluid density dependent shift $\Delta(\rho)$ in the ionization energy of a dopant molecule has led to the discovery of a novel effect on $V_0(\rho)$ occurring near the critical isotherm of the fluid. Unfortunately this method has limitations in determining $V_0(\rho)$ in fluids with low critical temperatures as well as fluids opaque to vacuum ultraviolet radiation. Thus, accurate determination of $V_0(\rho)$ in repulsive fluids (i.e., those possessing a positive zero kinetic energy electron scattering length) using field ionization is difficult.

The new method developed in this study, namely field enhanced photoemission, allows for the direct determination of the quasi-free electron energy from the density dependent shift in the work function of a metal electrode submerged in the fluid. This mitigates the problems posed by field ionization while producing results with similar precision. Field enhanced photoemission was verified by measuring $V_0(\rho)$ of Ar, an attractive fluid (i.e., one with a negative zero kinetic energy electron scattering length) studied extensively in the past by field ionization, before applying the method to the study of $V_0(\rho)$ in the repulsive fluids Ne, He and N_2. The new results showed a distinct critical point effect on $V_0(\rho)$, which was accurately modeled with the local Wigner-Seitz approach developed for attractive fluids. Thus, this work extends our theoretical model to repulsive fluids.

Unlike the attractive fluids studied in the past, the quasi-free electron energy in the repulsive fluids presented here is strictly positive. A careful analysis of the terms contributing to $V_0(\rho)$ within the local Wigner-Seitz model leads one to expect the quasi-free electron energy to be positive in repulsive fluids in general. A discussion of fluid density dependent behavior of the kinetic and potential energy terms contributing to $V_0(\rho)$ is presented along with an explanation of the evolution of the shape of the $V_0(\rho)$ curves for the fluids studied.

Acknowledgments

I would first like to thank my Major Professor, Dr. Cherice M. Evans, for her guidance and support during all of the stages of this project. I am also grateful to Dr. Gary L. Findley for elucidating some of the finer points of the local Wigner-Seitz model and for helping me to improve my writing. I also thank Dr. Jianbo Liu and Dr. Lawrence W. Johnson for the helpful feedback I received during annual committee meetings. I would like to express my gratitude to the undergraduates who worked on this project: Ms. Ollieanna Burke, Mrs. Samantha Dannenberg-Lushtak, Ms. Gabrielle Germain, Mr. Charles Payne, and Mr. Holden Smith, without whom the data acquisition process would have been much more difficult. We also thank the staff at the University of Wisconsin Synchrotron Radiation Center for maintaining the stainless steel Seya-Namioka beamline and for providing assistance in performing the various upgrades required to reach temperatures necessary for the studies presented here.

All of the measurements presented here were performed at the University of Wisconsin Synchrotron Radiation Center (NSF DMR-0537588) in Stoughton, WI. This work was supported by grants from the Petroleum Research Fund (45728-B6), from the Louisiana Board of Regents Support fund (LEQSF (2006-09)-RD-A-33), from the

Professional Staff Congress – City University of New York (62386-00 40), and from the National Science Foundation (NSF CHE-0956719).

Contents

List of Tables

List of Figures

Chapter 1

Introduction

Supercritical fluids (SCFs) are increasingly important in industrial [1–11] and environmental remediation [10–17] applications, because these fluids are considered environmentally friendly solvents [10, 18–20] that can be recaptured and reused. Since fluid density, viscosity, solubility and diffusivity can be tailored by adjusting the pressure and temperature, SCFs constitute controllable, tunable solvents. Competition between solute (dopant)/fluid (perturber) and perturber/perturber interactions in an SCF has been used to explain the narrow nanoparticle size distributions [21–24] and high structural purity of pharmaceutical compounds [25, 26] prepared in these solvents. The myriad factors (i.e., tunability, pressure, temperature, solubility, transport coefficients, fluid correlation lengths, etc.) that affect chemical reactions in near critical point fluids, make understanding of chemical processes in these systems troublesome [3, 27–29]. The difficulty in isolating these controlling factors necessitates choosing simpler model systems. With this in mind, we set out to investigate electron/fluid interactions as a function of increasing bulk (and local) solvent density. Since nanomaterials are formed by competition between repulsive solute/solvent interactions and attractive solvent/solvent interactions, our study focused on measurement of the quasi-free electron energy in fluids having repulsive electron/fluid interactions (i.e., He, Ne and N_2).

Previously, there have been two methods for measuring the quasi-free electron energy $V_0(\rho)$ in a fluid of density ρ, namely photoinjection (or photoemission) [30–37] from an electrode immersed in the fluid, and field ionization [31, 38–45] of high-n Rydberg states of a dopant molecule dissolved in the fluid.

$V_0(\rho)$ data obtained by direct photoemission measurements do not extrapolate to zero energy at zero density and possess significant experimental scatter [32–37,46,47]. To alleviate these problems, Reininger and co-workers [38–43] developed dopant field ionization, where the quasi-free electron energy is extracted from the fluid density dependent shift in the ionization energy of a dopant molecule with the use of a calculated parameter $P_+(\rho)$ [45,48–57]. ($P_+(\rho)$ is the ensemble average dopant core polarization energy and is calculated from the dopant/fluid and neat fluid radial distribution functions.)

Field ionization measurements produce precise data for the quasi-free electron energy $V_0(\rho)$ that led to the discovery of a novel critical point effect on $V_0(\rho)$ [45, 48–57]. Unfortunately, because of the difficulties imposed by the need for a dopant molecule, the applicability of this technique is limited. Once the range of fluids in which $V_0(\rho)$ could be determined using field ionization was exhausted, we elected to revisit photoinjection, since it is a direct measurement technique (i.e., it does not require a dopant).

We developed field enhanced photoemission (FEP), a method that utilizes the same principles as photoinjection. This new method, however, produces precise quasi-free electron energy data that extrapolate to zero energy at zero density. FEP has allowed us to determine $V_0(\rho)$ in He and N_2, fluids that could not have been analyzed with dopant field ionization. We were also able to show that the local Wigner-Seitz model [45–58] originally developed for attractive fluids was capable of predicting $V_0(\rho)$ in repulsive fluids as well. (We define attractive fluids as those with a negative zero kinetic energy electron scattering length and repulsive fluids as those with a positive zero kinetic energy electron scattering length.)

Chapter 2 first presents a largely qualitative discussion of the properties of dense fluids. We define attractive and repulsive electron/fluid potentials. We also discuss the types of mobility the solvated electron can possess in these fluids. Finally, we introduce the zero kinetic energy electron scattering length, an important parameter involved in the local Wigner-Seitz model that is used to interpret the data presented here.

In Chapter 3, we discuss the quasi-free electron energy, detailing the difficulties associated with direct photoinjection, and describe extraction of $V_0(\rho)$ from field ionization measurements in detail. We then present the limitations of field ionization when applied to repulsive fluids, which are the focus of this dissertation, and develop the theory behind the new field enhanced photoemission method. We also outline the experimental method of data analysis involved in this latter technique. Finally, we discuss various experimental methods of determining the energy of a solvated electron and present the local Wigner-Seitz model, a method that allows one to model $V_0(\rho)$ accurately at noncritical temperatures and on the critical isotherm.

All pertinent experimental information can be found in Chapter 4, where we discuss the different sample cells and cooling methods used to obtain the field ionization and FEP data presented here. This chapter also contains fluid and dopant information, such as sample sources and purities, as well as dopant parameters used in the field ionization data analyses.

Chapter 5 presents all of our novel experimental results. We start with field ionization measurements of Ne, the first repulsive fluid studied by our group. We then discuss an attempt to determine $V_0(\rho)$ in He using the same technique. After discovering that dopant field ionization is unsuited to measure $V_0(\rho)$ in fluids requiring very low temperatures, as well as in those opaque to vacuum ultraviolet light, we present FEP studies of He and N_2. The studies of $V_0(\rho)$ in Ne, He and N_2 presented here are the first ever extensive profiles of the quasi-free electron energy in these fluid across a broad density range. Critical point effects on $V_0(\rho)$ in these fluids are observed and accurately reproduced by the local Wigner-Seitz model, which verifies the applicability of this theoretical technique for simple repulsive fluids.

Chapter 2

Characteristics of Dense Fluids

Electrons in a low density gas behave as free particles, scattering off atoms or molecules while maintaining finite (but relatively high) electron mobilities [59]. However, as the density of the gas increases, new behaviors emerge [60]. In some fluids, an electron may be forced to localize in a cavity, surrounded by fluid atoms or molecules, drastically lowering the electron mobility since the entire cavity must propagate through the medium [59] (or the electron must tunnel between cavities [61]). In others the electron is quasi-free, possessing an energy different from that in a vacuum but maintaining a reasonably high mobility and a wavefunction not constrained to a cavity [59, 62–65]. Since our interests lie in determining the energy of an excess electron in a dense fluid, we begin by describing what happens when an electron interacts with one constituent of the fluid, which we then ultimately extrapolate to a dense fluid.

When a slow moving electron encounters a spherically symmetric square-well potential [$V(r) = U_0$ for $r < r_0$ and $V(r) = 0$ for $r \geq r_0$], such as that of a hard sphere, the scattering interaction will be predominantly s-wave. The wavefunction of such an electron is [66]

$$\begin{aligned} F(r) &= K \sin\,(kr) \qquad\quad , \quad r < r_0 \\ &= N_E \sin\,(k_0 r + \delta)\ , \quad r \geq r_0\ , \end{aligned} \tag{2.1}$$

where the reduced radial wavefunction $F(r)$ is the radial wavefunction $R(r)$ multiplied by r; N_E is a normalization factor; k and k_0 are the scattering wave vectors of the electron inside and outside the potential well, respectively, with $k^2 = 2m_eE/\hbar^2$ and $k_0^2 = 2m_e\left(E + U_0\right)/\hbar^2$, where m_e is the mass of the electron; and K and δ are parameters ensuring continuity at $r = r_0$. The parameter δ is of particular interest and is termed the phase shift. The conditions of $F(r)$ and $dF(r)/dr$ being continuous at $r = r_0$ can be combined into [66]

$$k \cot\,(kr_0) \;=\; k_0 \cot\,(k_0 r_0 + \delta)\ . \tag{2.2}$$

When the kinetic energy of the electron is near zero, the radial wavefunction does not change much at threshold. In the continuum region ($E > 0$), with k_0 near zero, $F(r)$ is a slowly-varying function of r, since δ must vanish proportionally to r_0. Therefore, we can define a new parameter A as [66]

$$A \;\equiv\; -\,\frac{\delta}{k_0}\ . \tag{2.3}$$

A is termed the scattering length and is used to obtain the low energy cross-section σ of the fluid constituent via [66]

$$\sigma \;=\; \frac{4\pi}{k_0^2}\sin^2\,\delta \;\simeq\; 4\pi A^2\ . \tag{2.4}$$

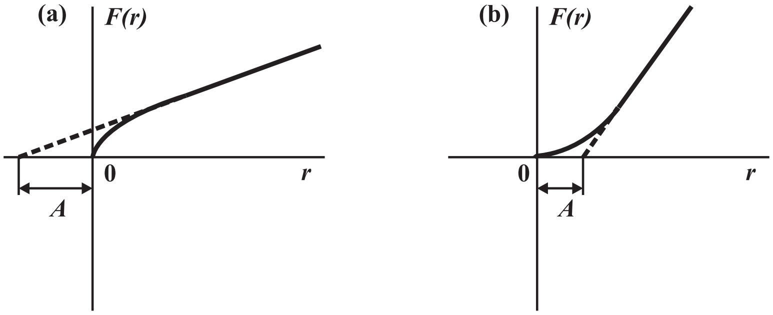

Figure 2.1: Reduced radial wavefunction $F(r)$ with $l = 0$ and $E \simeq 0$ for a short-ranged potential. Note the straight line segments when $r \geq r_0$. (a) is for an attractive potential; (b) is for a repulsive potential. Adapted from [66].

The physical significance of the scattering length can be readily seen in Fig. 2.1 in terms of the reduced radial wavefunction $F(r)$. When the kinetic energy of the electron is near zero (i.e., the electron is moving slowly), $F(r)$ in the $r \geq r_0$ region is proportional to $(r - A)$. Fig. 2.1a corresponds to a potential that is attractive within $r < r_0$, while Fig. 2.1b corresponds to a potential that is repulsive within $r < r_0$. (Note that the radial wavefunction $F(r)$ extended tangentially from the $r \geq r_0$ region determines the scattering length A. Fluid constituents with negative electron scattering length have an attractive electron/constituent potential, while those with a positive electron scattering length have a repulsive potential.)

As the density of the fluid increases, the fluid constituents cluster around the excess electron. If the constituents possess an attractive electron/constituent potential, the fluid constituents are pulled closer to the electron and, as can be seen in Fig. 2.2, an electron can find itself on the outside of a fluid cluster. Therefore, in an attractive fluid one is likely to find delocalized (or quasi-free) electrons that exhibit a relatively large electron mobility [59, 60, 62, 63].

If the electron/constituent potential is repulsive, however, two things can occur: the electron can either become quasi-free or localized. The fluid constituents can

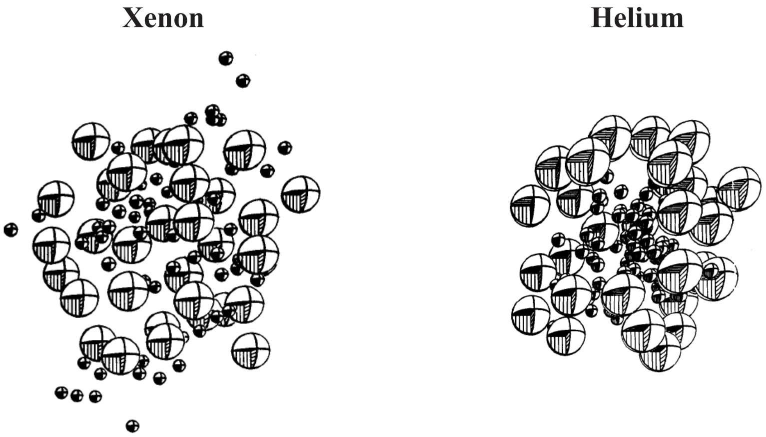

Figure 2.2: Snapshots of a quantum-mechanically modeled excess electron in classically modeled xenon and helium. The repulsive He traps electrons in a cavity, while in the attractive Xe electrons are quasi-free. Adapted from [59].

cluster around an electron, pushing it further into a cavity. The repulsive potential between electrons and the fluid constituents, and the attractive potential between the constituents themselves work together to keep an electron from escaping this cavity. The cavity geometry is determined by a competition of the repulsive potential and the surface tension of the fluid [63]. In a repulsive fluid, an electron confined to a cavity tends to be lower in energy and tends to have much longer drift times (lower mobilities), since the whole cavity moves with the electron [62–65]. However, electrons with sufficient energy can still be found to be delocalized in the conduction band of the fluid. Repulsive fluids therefore possess two mobility components: a fast quasi-free electron mobility and a slow localized mobility.

In our research, we are interested in measuring the energy $V_0(\rho)$ of the bottom of the conduction band in repulsive fluids. Thus, care must be taken to provide the excess electron with enough energy to prevent trapping in a cavity. (The energy of an electron trapped in a cavity is an interesting problem in its own right, but one that is outside the scope of the present work.) In this work, the energy needed to prevent trapping is provided by a strong DC electric field.

The zero kinetic energy electron scattering length A parameterizes the hard sphere potential of an atom or molecule and is crucial in setting the boundary conditions for determining the zero point kinetic energy $E_k(\rho)$ of the quasi-free electron, as will be discussed in some detail below. The zero kinetic energy electron scattering length can be extracted from the shift of a dopant's ionization energy in the low density fluid, using the Alekseev/Sobel'man extension of the Fermi model [45, 48, 67–69], or

$$\Delta(\rho) \;=\; \left(\frac{2\pi\hbar^2}{m_e}\right)\left[A - 9.87\left(\frac{m_e}{2\pi\hbar^2}\right)\left(\frac{\alpha e^2}{2}\right)^{\frac{2}{3}}(\hbar v)^{\frac{1}{3}}\right]\rho\,. \tag{2.5}$$

In eq. (2.5), $\Delta(\rho)$ is the fluid density dependent shift of the dopant ionization energy; $\hbar$ is the reduced Planck constant; m_e is the mass of the electron; A is the zero kinetic energy electron scattering length; e is the charge of the electron; α is the fluid polarizability; v is the thermal speed of the fluid constituents; and ρ is the bulk density of the fluid. Since all the parameters in eq. (2.5) except for A are known, one can determine the zero kinetic energy electron scattering length by obtaining $\Delta(\rho)$ measurements at various low fluid densities. Fig. 2.3 displays $\Delta(\rho)$ of CH_3I in selected fluids; the slopes of these lines, as well as the extracted scattering lengths, are collected in Table 2.1.

2.1 Attractive Fluids

As mentioned above, attractive fluids possess a negative zero kinetic energy electron scattering length A. Other notable features of attractive fluids include their gener-

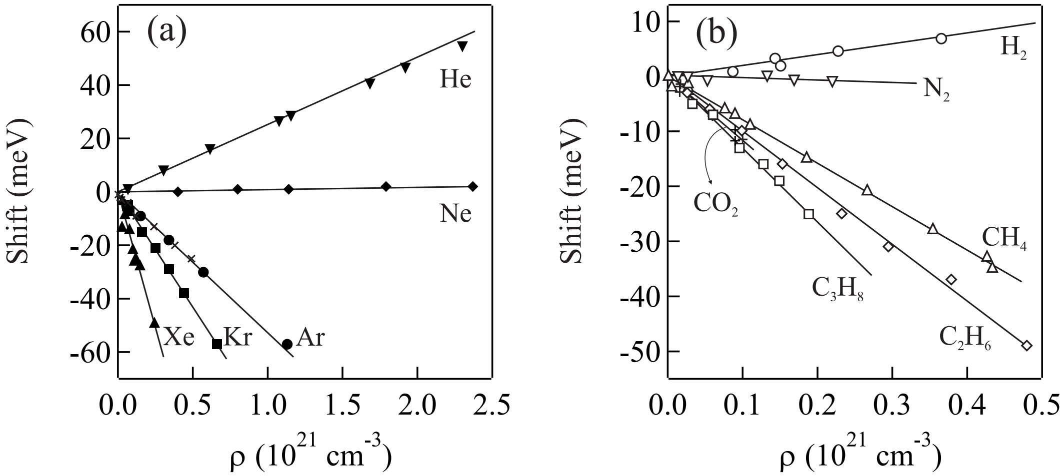

Figure 2.3: The fluid density dependent shift of the ionization energy of CH_3I for various atomic (a) and molecular (b) fluids at low fluid densities ρ [45]. The lines represent linear least squares analysis of the data to eq. (2.5).

ally negative quasi-free electron energy $V_0(\rho)$ [46, 49–55] and their relatively high critical and triple point temperatures. Therefore, $V_0(\rho)$ in these fluids lends itself to easy extraction from dopant field ionization measurements provided that the fluid is

Table 2.1: Experimental total shift rates Δ/ρ and zero-kinetic-energy electron scattering lengths A. All experimental data were obtained at ambient temperature (approximately 25°C).

Fluid	(10^{-23} eV cm^3) Δ/ρ	(Å) A	Reference
He	2.44	0.57	[70]
H_2	1.62	0.49	[71]
N_2	0.00	0.19	[72]
Ne	0.09	0.090	[70]
Ar	-4.75	-0.82	[73]
CH_4	-7.86	-1.38	[74]
Kr	-8.60	-1.60	[70]
C_2H_6	-10.1	-1.76	[74]
CF_4	-8.65	-1.80	[76]
CO_2	-11.8	-2.24	[75]
C_3H_8	-12.9	-2.28	[74]
Xe	-16.8	-3.24	[77]
SF_6	-24.7	-4.84	[76]
c-C_4F_8	-29.6	-6.18	[76]

not itself opaque to the vacuum ultraviolet radiation required to ionize the dopant. Building on Reininger's earlier work [38–43], our group has studied $V_0(\rho)$ in many such fluids, where we have shown that the local Wigner-Seitz approach [46, 49, 51–55] (to be discussed in Section 3.3.3) is an excellent method for predicting $V_0(\rho)$ along noncritical and critical isotherms.

2.2 Repulsive Fluids

Repulsive fluids possessing positive zero kinetic energy electron scattering lengths and positive $V_0(\rho)$ [47, 56–58] tend to have low critical and triple point temperatures, making some of them difficult if not impossible to analyze using dopant field ionization because of limited dopant solubility. It was with these fluids in mind, as well as with fluids opaque in the vacuum ultraviolet spectral range, that the field enhanced photoemission [46, 47, 58] technique presented here was developed to measure $V_0(\rho)$ directly.

Chapter 3

Quasi-Free Electron Energy

3.1 Introduction

As discussed in Chapter 2, an electron in a dense fluid can be either quasi-free, possessing a delocalized wavefunction, or trapped in a cavity bounded by fluid constituents. The present work focuses on measuring and modeling the energy of the quasi-free electron in dense atomic and molecular repulsive fluids. There have been two methods of measuring the quasi-free electron energy $V_0(\rho)$ in a fluid of density ρ, namely photoinjection [30–37] from a metal electrode immersed in the fluid, and field ionization [31, 38–45] of high-n Rydberg states of a dopant molecule dissolved in the fluid.

Photoinjection is a direct measurement of the quasi-free electron energy,

$$V_0(\rho) \;=\; \phi(\rho) \;-\; \phi_0 \;, \tag{3.1}$$

where $\phi(\rho)$ is the photoemission threshold of a metal immersed in the fluid and ϕ_0 is the work function of the metal. Unfortunately, $V_0(\rho)$ measurements obtained by direct photoinjection do not always extrapolate to zero energy at zero fluid density and possess significant experimental scatter (cf. Fig. 3.1). The experimental scatter can be explained by surface roughness and by oxide and fluid constituent coating of

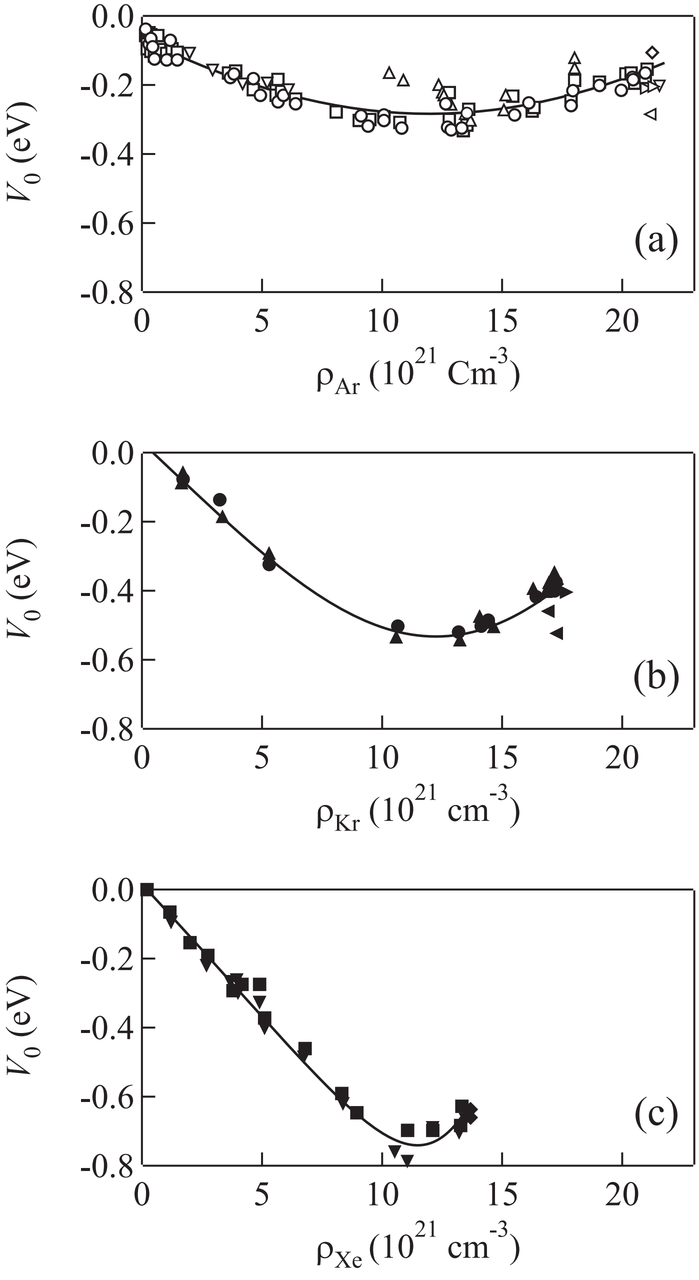

Figure 3.1: $V_0(\rho)$ of fluids obtained from various photoinjection measurements, as a function of fluid number density ρ. (a) Ar: (○, □) [32] with different evaluations, (△) [33], (◇) [34], (◁) [35], (▷) [36], and (▽) [78]. (b) Kr: (▲, ●) [37] with different evaluations, (◀) [34], and (▶) [36]. (c) Xe: (■, ▼) [37] with different evaluations, and (♦) [34]. The lines are provided as a visual aid.

the electrode. Moreover, the lack of extrapolation to zero energy at zero density is likely due to researchers using a published work function for the electrode rather than establishing a temperature dependent reference work function (cf. Section 3.3 below) for each electrode used.

Dopant field ionization (DFI) was developed to address these difficulties [31, 38–45]. DFI extracts the quasi free electron energy from the shift in the ionization energy of an impurity (i.e., a dopant) and produces very precise data (cf. Fig. 3.2). The high precision of $V_0(\rho)$ data obtained with dopant field ionization allowed our group to observe a novel critical point effect on $V_0(\rho)$ [50–57]. This technique will be discussed in detail in Section 3.2 below.

However, since dopant field ionization requires a dopant molecule, it is not a viable technique for determining $V_0(\rho)$ across the entire density range of most repulsive fluids, since solubility, fluid opacity and the characteristic blue shift of the dopant ionization energy [47, 57, 58] make the selection of an appropriate dopant difficult if not impossible [46]. With these limitations in mind, we developed a new experimental technique, termed field enhanced photoemission. This technique uses photoemission from an electrode immersed in a fluid as in direct photoinjection, while addressing the various problems encountered with this latter method. (As will be seen in Fig. 3.7, field enhanced photoemission, which is discussed in detail below, produces $V_0(\rho)$ data on a par with dopant field ionization, without any need for a dopant.)

Modeling the behavior of an excess electron in a dense fluid is a tricky problem. It is much less well understood in comparison to the behavior of an electron in low density gases and crystalline solids. In crystalline solids, the symmetry of the

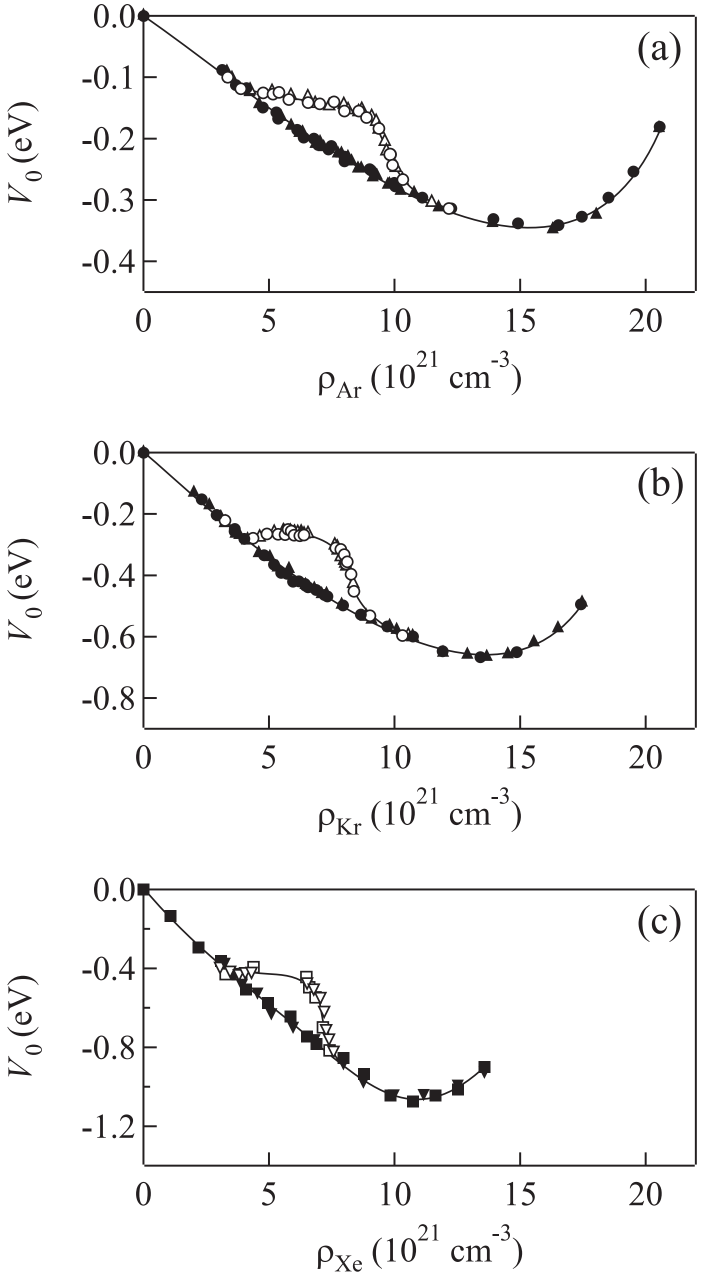

Figure 3.2: The quasi-free electron energy $V_0(\rho)$ for (a) Ar [50–52], (b) Kr [50, 53] and (c) Xe [54] at non-critical temperatures (solid markers) and on an isotherm near the critical isotherm of the perturber (open markers), extracted from eq. (3.2), as a function of fluid number density ρ. (▲ [50], △ [51, 53] represent data extracted from CH_3I field ionization, (● [50], ○ [52,53]) are data obtained from C_2H_5I field ionization, (■ [54], □ [54]) are data determined from N, N-dimethylaniline field ionization, and (▼ [54], ▽ [54]) represent data from trimethylamine field ionization. The lines are provided as a visual aid.

medium reduces the complexity of the problem. And, as mentioned in Chapter 2, in low density gases the problem can be reduced to an electron scattering off a single fluid constituent. While arguments similar to those presented in Chapter 2 can qualitatively describe the behavior of an excess electron, the quantitative modeling of this behavior in dense fluids is difficult. Despite this difficulty, several methods do exist for determining the energy of an excess electron in a dense fluid. Some of these methods [45–47, 49–55, 57–59, 79–81], including the local Wigner-Seitz approach developed by our group [45–47, 49–55, 57, 58], will be presented in the later sections of this chapter.

3.2 Experimental Methods and Analysis

3.2.1 Dopant Field Ionization

The quasi-free electron energy can be obtained from the shift $\Delta(\rho)$ in the ionization energy of a dopant molecule. Because of the large orbital nature of a high-n Rydberg state, the fluid/electron and fluid/dopant core interactions can be separated [45, 67, 69]. Therefore, $\Delta(\rho)$ can be written as a sum of interactions [48–57, 82]

$$\Delta(\rho) \;=\; P_{+}(\rho) \;+\; V_0(\rho), \tag{3.2}$$

where $P_{+}(\rho)$ is the adiabatic ensemble average fluid/dopant core polarization energy arising from the fluid constituent distribution around the neutral dopant molecule [78], and $V_0(\rho)$ is the quasi-free electron energy in the fluid. (We should note here that the density of a dopant is always kept small so that the likelihood of interaction between two dopant molecules is insignificant; thus no dopant density effects need be considered.) The ensemble average dopant core/fluid polarization energy is obtained from [45, 48–57]

$$P_{+}(\rho) \; = \; -4\pi\rho \int_{0}^{\infty} \; g_{\mathrm{D}}(r)\, w_{+}\, r^{2} dr \; , \tag{3.3}$$

where $g_{\mathrm{D}}(r)$ is the dopant/fluid radial distribution function determined by direct integration of the Orstein-Zernike relation with a Percus-Yevick closure [83], and w_{+} is the dopant core/fluid interaction potential given by [45, 48–57]

$$w_{+}(r) \; = \; -\, \frac{1}{2}\, \alpha\, e^{2} \, \sum_{i}^{N} r_{i}^{-4}\, f_{+}(r_{i}) \; , \tag{3.4}$$

where r_i is the distance to the ith fluid constituent, while $f_{+}(r_i)$ is a screening function that accounts for the diminished interaction between the ith fluid constituent and the dopant core due to dipoles induced in other fluid constituents. The screening function is given by [45, 84]

$$f_{+}(r) = 1 - \alpha\pi\rho \int_{0}^{\infty} ds\, \frac{1}{s^{2}}\, g(s) \; \int_{|r-s|}^{r+s} dt\, \frac{1}{t^{2}}\, f_{+}(t)\, g_{\mathrm{D}}(r)\, \theta(r,s,t) \; , \tag{3.5}$$

where s and t are distances between the fluid constituent of interest and other fluid constituents, $g(r)$ is the fluid constituent/fluid radial distribution function, and

$$\theta(r,s,t) = 3(s^{2} + t^{2} - r^{2})\,(s^{2} - t^{2} + r^{2})/(2s^{2}) + (r^{2} + t^{2} - s^{2}) \; . \tag{3.6}$$

Note that the quantity $P_{+}(\rho)$ depends on the dopant/fluid radial distribution function as well as the on neat fluid radial distribution function.

The interaction between the high-n electron and the cationic core can be described by a Coulomb potential (i.e., $-e^{2}/r$). When an electric field is applied, the angular momentum states become coupled. As can be seen in Fig. 3.3, this coupling lowers the ionization energy in comparison to the zero field limit. We shall refer to the shift

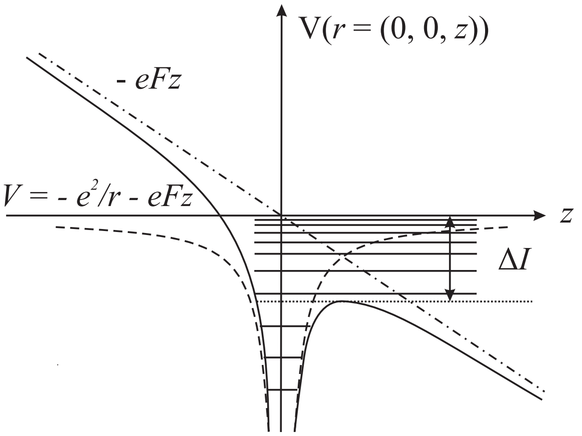

Figure 3.3: Field ionization of Rydberg states. (- - -) Coulomb potential ($-e^2/r$), (- · -) external electric field on z direction, (— curve) core-electron potential under the electric field. Note ΔI is the lowering of the ionization limit.

in ionization energy as ΔI. The high-n Rydberg states with binding energies less than ΔI will be ionized by the electric fields but lower-n Rydberg states will not.

The classical field ionization limit of a hydrogen atom is given by $\Delta I = -2F^{1/2}$ [45] (in atomic units). However, the work presented here utilizes the field ionization of molecular Rydberg states, and therefore we must define the classical field ionization limit for a molecule. Since rotational and vibrational effects contribute to the ionization energy, the field ionization limit becomes [31, 45]

$$\Delta I = -c_0 F^{1/2} \tag{3.7}$$

where c_0 is a dopant dependent constant that must be determined empirically. Since, unlike photoinjection data, dopant field ionization measurements are not affected by the structure of the electrode or by electrode coating, our group [45, 48–57] and others [38–43] have been able to obtain extensive sets of $\Delta(\rho)$ data [30, 31, 42, 44, 85–91] with significantly less scatter than seen in photoinjection. Precise $\Delta(\rho)$ measurements in conjunction with accurate $P_+(\rho)$ calculations allow one to reliably determine $V_0(\rho)$ from eq. (3.1). It has been shown that while $\Delta(\rho)$ certainly depends on the choice of a dopant and, to a certain extent, on temperature, $V_0(\rho)$ is completely dopant independent [45, 56].

Intensity normalized photoionization spectra of neat CH_3I obtained at various electric fields are shown as a function of incident radiation energy in Fig. 3.4a. While one can clearly see the changes in the spectra as a function of the electric field, precisely determining the energy of a field ionization peak is difficult. Thus, a field ionization spectrum is obtained by subtracting intensity normalized dopant photoionization spectra obtained at two different applied electric fields. The variation of F_H leads to a characteristic energetic shift of the easily observed field ionization peak in the field ionization spectrum (cf. Fig. 3.4b). (The field ionization peak corresponds to high-n Rydberg states ionized by F_H but not by F_L.) This shift, plotted against the sum of the square roots of the electric fields, yields a straight line (cf. Fig. 3.4c) defined by [38–43, 45, 48–57]

$$I_F(\rho) \;=\; I_0(\rho) \;-\; c_0 \left(\sqrt{F_L} + \sqrt{F_H}\right) \;, \tag{3.8}$$

where $I_F(\rho)$ is the dopant ionization energy altered by the electric field and the dense fluid medium, $I_0(\rho)$ is the zero field ionization energy of the dopant and c_0 is a dopant dependent empirical constant.

In order to reduce any error introduced by normalization, three different energy regions of the photoionization spectra are chosen for intensity normalization. The energy of the peak in each of the three resulting field ionization plots is calculated by three nonlinear Gaussian fits. Therefore, the field ionization energy for every set of two photoinization spectra is determined from an average of nine energy values.

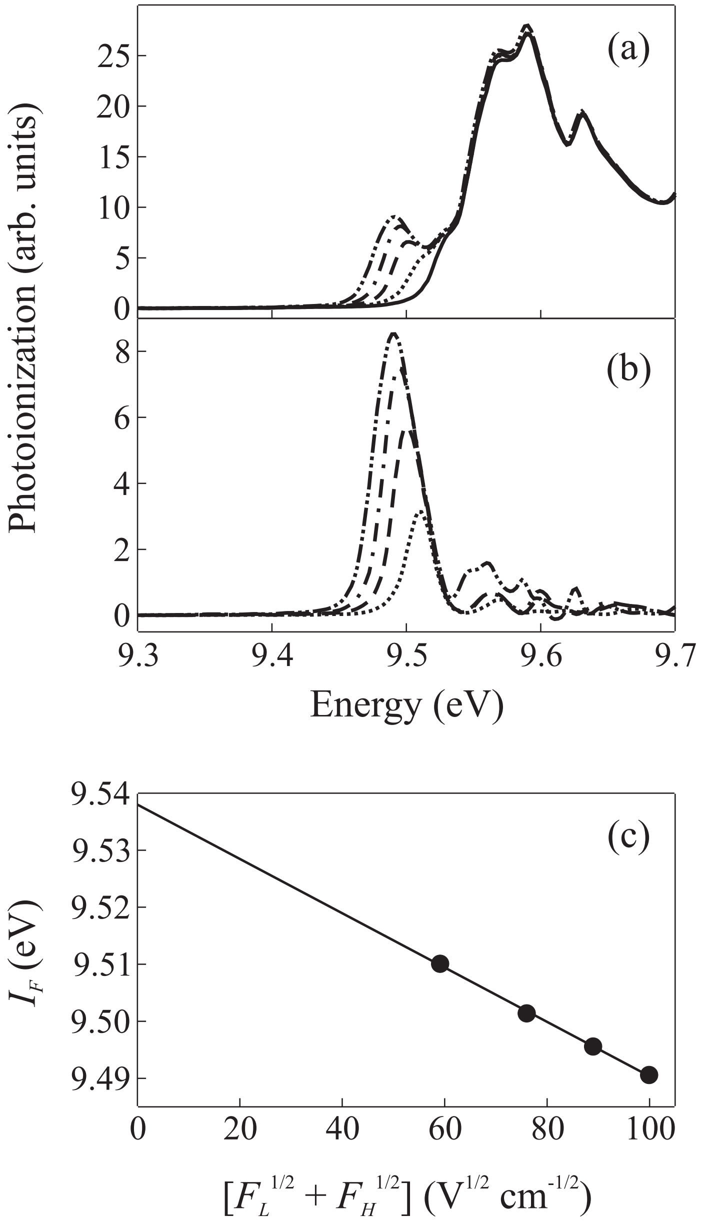

Figure 3.4: Field ionization study of 0.10 mbar CH_3I. (a) Photoionization spectra at (—) 0.33 kV/cm, (···) 1.7 kV/cm, (- - -) 3.3 kV/cm, (- · -) 5.0 kV/cm, and (- ·· -) 6.7 kV/cm after intensity normalization, necessary to correct for secondary ionization. (b) Field ionization spectra obtained with $F_L = 0.33$ kV/cm and with various F_H [see (a)]. (c) The energy I_F of the field ionization peak plotted as a function of the square root of the electric fields. See text for discussion.

Once $I_F(\rho)$ for the experimental data and c_0 have been determined, eq. (3.8) is used to obtain the zero field ionization energy of the dopant at a given fluid density, $I_0(\rho)$. Finally, the fluid dependent shift $\Delta(\rho)$ of the dopant ionization energy is obtained from [38–43, 45, 48–57]

$$\Delta(\rho) \;=\; I_0(\rho) \;-\; I_g \tag{3.9}$$

where I_g is the ionization energy of the dopant in the gas phase, which is determined from field ionization data of a neat dopant. (See section 4.4.1 for c_0 and I_g values for the dopants involved in this work.)

Dopant field ionization enabled our group to measure $V_0(\rho)$ across the entire density range from low density to the density of the triple point fluid at various temperatures in a host of fluids [45, 48–56] and, for this dissertation, in Ne [57] (cf. Chapter 5). The study presented here and the ones completed previously showed a pronounced change in $V_0(\rho)$ occurring near the critical temperature and around the critical number density, as is clearly seen in Fig. 3.2. However, this method has limitations that make it difficult to implement in the determination of $V_0(\rho)$ in most repulsive fluids.

In general, repulsive fluids have lower critical temperatures than do attractive fluids. Therefore, the appropriate dopant would have to stay in solution at extremely low temperatures (around 5.2 K for He, for instance) in order to maintain a photoionization signal. The ionization energy of the dopant also must be below the cut-off energy of the cell window (cf. Chapter 4) along the entire density range of the fluid, and since repulsive fluids tend to have strictly positive quasi-free electron energies, this poses a problem in that the ionization energy of a dopant may be above this cut-off energy. In addition to the window cut-off energy limitation, the ionization energy of the dopant must occur in a spectral region where the fluid itself is transparent. Thus, the quasi-free electron energy in two of the three systems presented in this work, namely helium-4 and molecular nitrogen, simply cannot be determined using dopant field ionization. ^{4}He possesses a very low critical temperature and an extremely positive $V_0(\rho)$ (cf. Chapter 5 for a detailed discussion), and N_2 absorbs strongly in the spectral region of interest.

In addition to the difficulties outlined above, the calculated parameter $P_+(\rho)$ is required to extract $V_0(\rho)$ from the experimentally obtained data (cf. eq. (3.3)). One can see from eq. (3.5) that accurate dopant/fluid and fluid/fluid radial distribution functions need to be calculated in order to produce an accurate $P_+(\rho)$, and therefore one must have very good dopant/fluid and fluid/fluid intermolecular potentials available to determine $V_0(\rho)$ precisely.

3.2.2 Field Enhanced Photoemission

Since all of the difficulties involved in dopant field ionization arise from the need for a dopant, we have devised a technique, namely field enhanced photoemission (FEP), that utilizes the direct $V_0(\rho)$ measurement method of photoinjection (i.e., eq. (3.1)) while mitigating the problems prevalent in this approach. We shall first derive the functional form for photoemission from a metal electrode in a vacuum under the influence of an electric field, and then make the adjustments necessary to insure that this functional form is applicable to a precise study of $V_0(\rho)$ in a dense fluid.

A DC electric field applied normal to an electrode surface changes the potential barrier encountered by a photoemitted electron. The potential seen by the electron

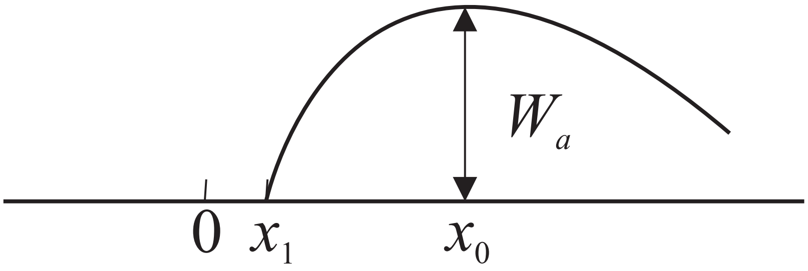

Figure 3.5: Schematic of the potential barrier experienced by an electron that is photoemitted from a cathode. The metal surface is at $x = 0$. x_1 is the point at which the external potential goes to zero, and we assume that the potential seen by the electron is approximately zero at distances shorter than x_1. See text for discussion. Adapted from [92].

is (cf. Fig. 3.5) [92, 93]

$$V = \phi_0 - (e^2/4x) - eFx , \tag{3.10}$$

where ϕ_0 is the difference between the potential energy of the electron in the metal and at $x = \infty$ in the absence of an electric field (i.e., the zero field work function of the electrode); x is the distance from the origin (i.e., the electrode surface); and F is the magnitude of the applied electric field. If we take $\phi_0 = \chi_0 - \epsilon_F$, with ϵ_F being the Fermi energy, then χ_0 is the total potential barrier height [94]. The work function of the cathode is given by the maximum of the potential seen by the electron. The maximum of eq. (3.10), determined by taking its derivative with respect x, is $\phi_0 - e^{3/2}F^{1/2}$. Therefore, in the presence of an electric field of magnitude F, $\phi_0 - e^{3/2}F^{1/2}$ is the work function while $\chi_0 - e^{3/2}F^{1/2}$ is the maximum total potential barrier height. The photocurrent can be written as [92, 93]

$$i \propto \int_{\chi_0 - e^{3/2}F^{1/2} - h\nu}^{\infty} dW N(W) P(W, h\nu) D(W, F) , \tag{3.11}$$

where W is the normal energy of the electron (i.e., the energy corresponding to the velocity component normal to the electrode surface); $N(W)$ is the number of electrons with a given normal energy; $P(W, h\nu)$ is the probability that an electron with a given normal energy will absorb a photon with an energy $h\nu$; and $D(W, F)$ is the probability that an electron with a normal energy W will escape under an electric field of magnitude F after having absorbed a photon with an energy $h\nu$. Note that $\chi_0 - e^{3/2}F^{1/2} - h\nu$ sets the lower limit of integration, and therefore only electrons with enough energy to overcome the potential barrier upon absorbing a photon are considered.

Provided that the photon energy is in the neighborhood of the photoemission threshold, $P(W, h\nu)$ can be assumed to be independent of the normal energy [93]. $D(W, F)$ can be taken as unity to a good approximation [93, 94], and any increase in photocurrent due to a larger field arises from the shift in the threshold energy rather than from a direct field dependent change of $D(W, F)$ [93]. Thus, the photocurrent can be rewritten as [93, 94]

$$i \propto \int_{\chi_0 - e^{3/2}F^{1/2} - h\nu}^{\infty} dW\, N(W)\ . \tag{3.12}$$

In a gas of particles obeying Fermi-Dirac statistics, the portion of particles having velocity components in the ranges $(u, u + du)$, $(v, v + dv)$, and $(w, w + dw)$ is given by [94, 95]

$$n(u, v, w)\, du\, dv\, dw \ = \ 2\left(\frac{m}{h}\right)^3 \frac{du\, dv\, dw}{\exp\{\frac{1}{2}m\,(u^2 + v^2 + w^2) - \epsilon^*\}/k_B T + 1}\ , \tag{3.13}$$

where $\epsilon^* \simeq \epsilon_F$ [94] is a constant ensuring the correct number of particles per unit volume; k_B is the Boltzmann constant; and T is the temperature. For our purposes, the particles are electrons and the velocity component u is normal to the electrode surface. Since eq. (3.12) requires the portion of electrons with a certain minimum energy normal to the electrode surface, this portion is obtained from [94]

$$N(u)\,du \;=\; 2\left(\frac{m}{h}\right)^3 du \int_0^\infty \int_0^{2\pi} \frac{ds\,d\theta\,s}{\exp\left\{\frac{1}{2}m\left(u^2+s^2\right)-\epsilon^*\right\}/k_BT+1}\;, \tag{3.14}$$

where we have changed the coordinates to an (s,θ,u) cylindrical system. Carrying out the integration gives [94]

$$N(u)\,du \;=\; \frac{4\pi k_BT}{m}\left(\frac{m}{h}\right)^3 \ln\left[1+\exp\left(\epsilon^*-\frac{1}{2}mu^2\right)/k_BT\right] du\;. \tag{3.15}$$

Note that we can easily recast eq. (3.12) with i as a function of u since $W=\frac{1}{2}mu^2$. Thus eq. (3.12) becomes

$$i \;\propto\; k_BT\int_{\frac{1}{2}mu^2=\chi_0-e^{3/2}E^{1/2}-h\nu}^{\infty} du\,\ln\left[1+\exp\left(\epsilon^*-\frac{1}{2}mu^2\right)/k_BT\right]. \tag{3.16}$$

The integration limits in the above expression can be simplified by making the substitution $y=(\epsilon^*-\chi+e^{3/2}F^{1/2}+h\nu+\frac{1}{2}mu^2)$, yielding

$$i \;\propto\; \left(k_BT\right)^{3/2}\int_0^\infty dy\,\frac{\ln\left[1+\exp\left(-y+\left(h\nu+e^{3/2}F^{1/2}-\phi_0\right)/k_BT\right)\right]}{\sqrt{y+(\chi_0-h\nu-e^{3/2}F^{1/2})/k_BT}}\;. \tag{3.17}$$

Since one of the assumptions made previously is that the photon energy is near the photoemission threshold, $h\nu+e^{3/2}F^{1/2}-\phi_0$ is comparable to k_BT, and the numerator in eq. (3.17) cannot be simplified. However, $\chi_0-h\nu-e^{3/2}F^{1/2}$ is much larger than $y\,k_BT$ and y can be neglected in the denominator, producing [93]

$$i \;\propto\; \frac{\left(k_BT\right)^2}{\left(\chi_0-h\nu-e^{3/2}F^{1/2}\right)^{1/2}}\int_0^\infty dy\,\ln\left[1+\exp\left(-y+\left(h\nu+e^{3/2}E^{1/2}-\phi_0\right)/k_BT\right)\right]. \tag{3.18}$$

The integral in eq. (3.18) cannot be evaluated exactly unless $h\nu=\phi_0-e^{3/2}F^{1/2}$. However, we can set $\mu\equiv(h\nu+e^{3/2}F^{1/2}-\phi_0)/k_BT$, expand the expression in powers of μ, and integrate each term separately. When $\mu \leq 0$,

$$i \propto \frac{(k_B T)^2}{(\chi_0 - h\nu - e^{3/2}F^{1/2})^{1/2}} \left[e^{\mu} - \frac{e^{2\mu}}{2^2} + \frac{e^{3\mu}}{3^2} \dots \right] . \tag{3.19}$$

However, this region is of little interest since the limits of integration give the photocurrent only when $\mu \geq 0$. On the high energy side of the threshold, more effort is required to reach a useful functional form. Upon rearrangement and an evaluation of the integral portion of eq. (3.18) term by term, we get

$$i \propto \frac{(k_B T)^2}{(\chi_0 - h\nu - e^{3/2}F^{1/2})^{1/2}} \left[\frac{\pi^2}{6} - \frac{1}{2}\mu^2 - \left(e^{-\mu} - \frac{e^{-2\mu}}{2^2} + \frac{e^{-3\mu}}{3^2} \dots \right) \right] . \tag{3.20}$$

The exponential terms in eq. (3.20) can be omitted provided that the applied electric field is large [93]. Additionally, provided that the photon energy is in the neighborhood of the threshold, $\chi_0 \gg h\nu + e^{3/2}F^{1/2}$ and the $(\chi_0 - h\nu - e^{3/2}F^{1/2})$ term can be taken as constant [93]. Thus, for photon energies larger than the threshold, yet in the vicinity of the threshold [46, 47, 92–94],

$$i = C\, {k_B}^2 T^2 \left[\frac{1}{6}\pi^2 + \frac{1}{2{k_B}^2 T^2} \left(h\nu - \phi_0 + \sqrt{e^3 F} \right)^2 \right] . \tag{3.21}$$

where C is an empirical constant that depends on the fraction of electrons that can absorb a photon and escape.

When the metal electrode (Pt for these studies) is immersed in a fluid as opposed to a vacuum, the fluid interacts with the electrode, thereby changing the potential step experienced by an escaping electron. Furthermore, the photoemitted electron undergoes multiple scattering events, thus reducing the number of electrons detected. In this instance, $C \to B(T, \rho)$. Moreover, changes in the relative fluid permittivity $\varepsilon_r(T, \rho)$ as a function of density and temperature must also be considered in accounting for the effects of the applied electric field. Under these conditions, eq. (3.21) becomes [46,47]

$$i \;=\; B(T,\rho)\, {k_B}^2\, T^2 \left[\frac{1}{6}\pi^2 \;+\; \frac{1}{2{k_B}^2 T^2}\, \left(h\nu - \phi(\rho) + \sqrt{\frac{e^3 F}{\varepsilon_r(T,\rho)}}\right)^2\right] \;, \qquad (3.22)$$

where $\phi(\rho)$ is the Pt work function in the presence of the fluid, and $\varepsilon_r \;\equiv\; \varepsilon(T,\rho)/\varepsilon_0$ is the temperature and density dependent relative permittivity of the fluid, with ε_0 being the permittivity of the vacuum.

The functional form of eq. (3.22) can be used to directly fit a photoemission spectrum of an electrode immersed in a dense fluid medium to obtain the density dependent photoemission threshold $\phi(\rho)$. If one rearranges the equation to yield a second order polynomial, however, it becomes evident that $\phi(\rho)$ depends on two polynomial coefficients, necessitating an absolutely immaculate fit in order to determine the threshold precisely. Since experimental data always possess some noise and since the fit may not be perfect due to small deviations from theory, one could not hope to achieve the precision required to conclusively show, for example, a critical point effect on $V_0(\rho)$ that is often smaller than 0.1 eV.

Researchers in the past used various forms of eq. (3.22) to obtain $V_0(\rho)$ in dense fluids [32–37,94]. Two notable approaches are logarithm plots and square root plots. In logarithm plots, the natural logarithm of the relative photocurrent (i.e., photocurrent normalized by lightsource flux) is plotted against photon energy to get rid of the multiplicative constant, and the function is fitted by non-linear least squares analysis. The square root plot method operates under the assumption that $\pi^2/6$ is much smaller than $(2k_B^2T^2)^{-1}\ (h\nu - \phi(\rho))^2$ as long as the photon energy is somewhat higher than $\phi(\rho)$. The square root of the relative photocurrent yields an approximately linear region to the blue of the threshold, and this linear region is used to determine $\phi(\rho)$. Both of these methods generally produce $V_0(\rho)$ values that are approximately correct but have a large amount of scatter and do not always extrapolate to zero energy in vacuum (compare Fig. 3.1 to 3.2).

We elected to take a different analytical approach. The bracketed kernel of eq. (3.22) can be rearranged to yield

$$\frac{1}{6}\pi^2 + \frac{1}{2{k_B}^2T^2}\left((h\nu - \phi(\rho))^2 - (h\nu - \phi(\rho))\sqrt{\Lambda} + \Lambda\right) , \tag{3.23}$$

where $\Lambda = e^3F/(\varepsilon_r(T,\rho))$. (Note that the second-order term in eq. (3.23) is field independent.) Thus, if we obtain two spectra at different applied electric fields and subtract them, we get, after some rearrangement [46, 47],

$$\frac{\Delta i}{B(T,\rho)} = [h\nu - \phi(\rho)]\left(\sqrt{\Lambda_H} - \sqrt{\Lambda_L}\right) + \frac{1}{2}(\Lambda_H - \Lambda_L) . \tag{3.24}$$

In eq. (3.24), the subscripts L and H denote the low and high applied electric fields, respectively. Additional rearrangement of eq. (3.24) yields a linear functional form [46, 47, 58]

$$h\nu = b\,\Delta i_E + a , \tag{3.25}$$

where the slope is $b = 1/B(T,\rho)$,

$$\Delta i_E = \frac{\Delta i}{\sqrt{\Lambda_H} - \sqrt{\Lambda_L}} , \tag{3.26}$$

and the intercept $a(\rho)$ is

$$a(\rho) = \phi(\rho) - \frac{1}{2}\left(\sqrt{\Lambda_H} + \sqrt{\Lambda_L}\right) . \tag{3.27}$$

Thus, the field enhanced photoemission (FEP) signal is a graph of photon energy as a function of Δi_E. When the linear region of this signal is fitted by a linear least squares analysis, the intercept $a(\rho)$ yields the work function $\phi(\rho)$ in the zero field limit. The quasi-free electron energy is then determined from

$$V_0 = \phi(\rho) - \phi_0 , \tag{3.28}$$

where ϕ_0 is the reference work function, also obtained using the FEP analysis.

The quasi-free electron energy in a dense fluid is determined via FEP as follows. A set of four (or five) Pt photoemission spectra is recorded at each fluid density (cf. Fig. 3.6a). The spectra recorded at lower electric fields are then subtracted from those recorded at higher electric fields to produce Δi_E. Photon energy is plotted as a function of Δi_E (cf. Fig. 3.6b) producing six (or ten, respectively) FEP plots. The FEP signal is fitted to eq. (3.25) and the resulting energy axis intercept a is graphed as a function of $\Lambda_H^{1/2} + \Lambda_L^{1/2}$ (cf. Fig. 3.6c). These plots are then used to extrapolate the zero field limit photoemission threshold $\phi(\rho)$ by a linear regression. Finally, eq. (3.28) is used to determine $V_0(\rho)$. Since this technique utilizes six (or ten, respectively) FEP plots to determine $\phi(\rho)$, the scatter is significantly reduced.

The problem of not extrapolating to zero energy at zero density is easily solved by appropriately choosing ϕ_0 in eq. (3.28). If the published work function for the metal is chosen, one is likely to observe some deviation from zero energy when the electrode is in vacuum. Since the electrode for photoemission measurements has to be very thin ($\sim$ 10 nm), it is usually made by chemical vapor deposition or sputter coating the metal onto a MgF_2 or LiF window. The result is a roughly uniform coating that is not smooth and is certainly not a single crystal. Moreover, since

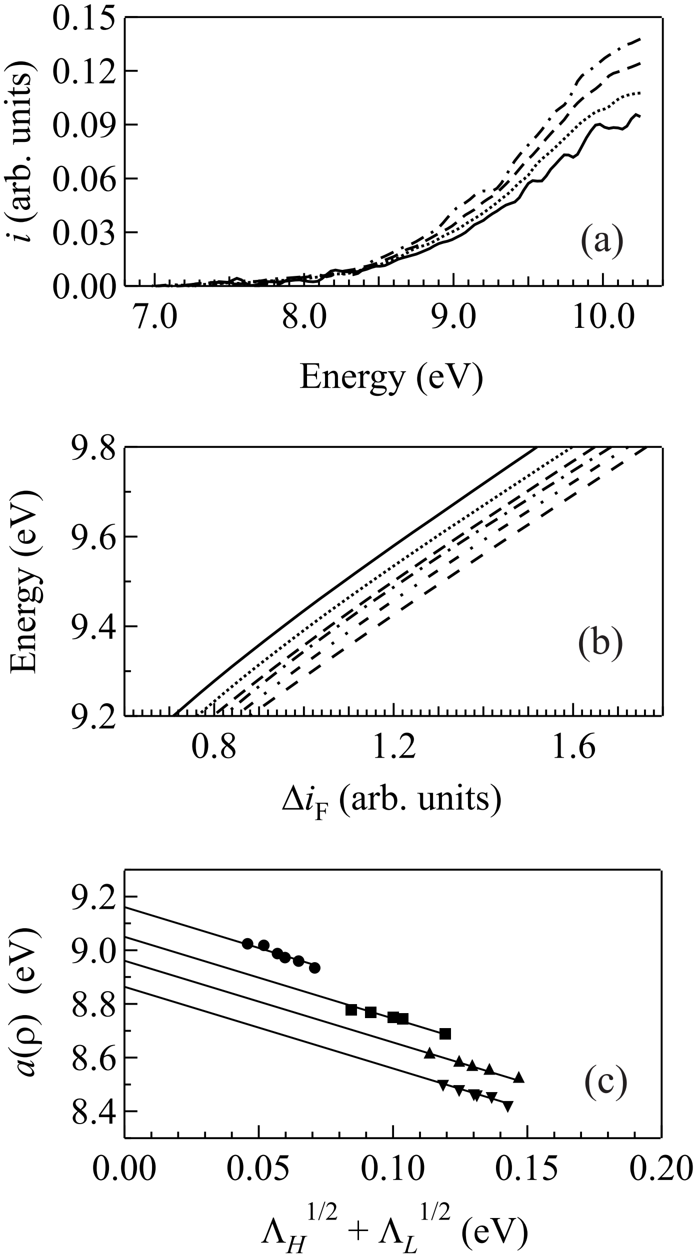

Figure 3.6: Field enhanced photoemission study of argon at T = 158 K and $\rho = 11.0 \times 10^{21}$ cm^{-3}. (a) Photoemission spectra recorded at applied fields of (—) 20 kV/cm, (···) 25 kV/cm, (- -) 30 kV/cm, and (- · -) 35 kV/cm. (b) Photon energy as a function of Δi_E. (c) The intercept $a(\rho)$ of representative FEP plots. The number densities are (●) 4.1×10^{19} cm^{-3}, (■) 4.1×10^{21} cm^{-3}, (▲) 7.1×10^{21} cm^{-3}, and (▼) 1.1×10^{22} cm^{-3}.

windows do break, each new electrode is different. After preparation, the electrode usually is not stored under vacuum and thus accumulates an oxide coating. When immersed in the fluid, fluid constituents coat the electrode changing the height of the potential barrier encountered by the electron. These factors can easily shift the work function of the electrode by a few eV from the published value, since even during the different stages of preparation of a perfectly smooth single crystal electrode, the work function changes significantly [96]. Because the observed work function is not likely to correspond closely to the published values, each photoemitting electrode was characterized here by obtaining a set of spectra at a very low fluid density, on the order of $\rho = 10^{20}$ cm^{-3}, at every temperature, and of course for every fluid studied. The resulting work function is taken as the reference ϕ_0 in eq. (3.28).

Fig. 3.7, in which the panel (c) depicts the quasi-free electron energy in argon obtained using field enhanced photoemission measurements, clearly shows that this new technique possesses precision vastly superior to direct photoemission and on a par with dopant field ionization. FEP was successfully used here to determine $V_0(\rho)$ in He and N_2, and a detailed discussion of the quasi-free electron energy in these fluids will be found in Chapter 5.

3.3 Theoretical Modeling

3.3.1 Wigner-Seitz Model

The Wigner-Seitz model [79,80], originally developed for solid state physics, serves as the basis for many treatments of $V_0(\rho)$. The symmetry of a perfect crystal allows one to isolate each crystal constituent in an identical Bravais lattice cell. One such type of cell is the Wigner-Seitz cell, consisting of all points in space closer to the lattice point

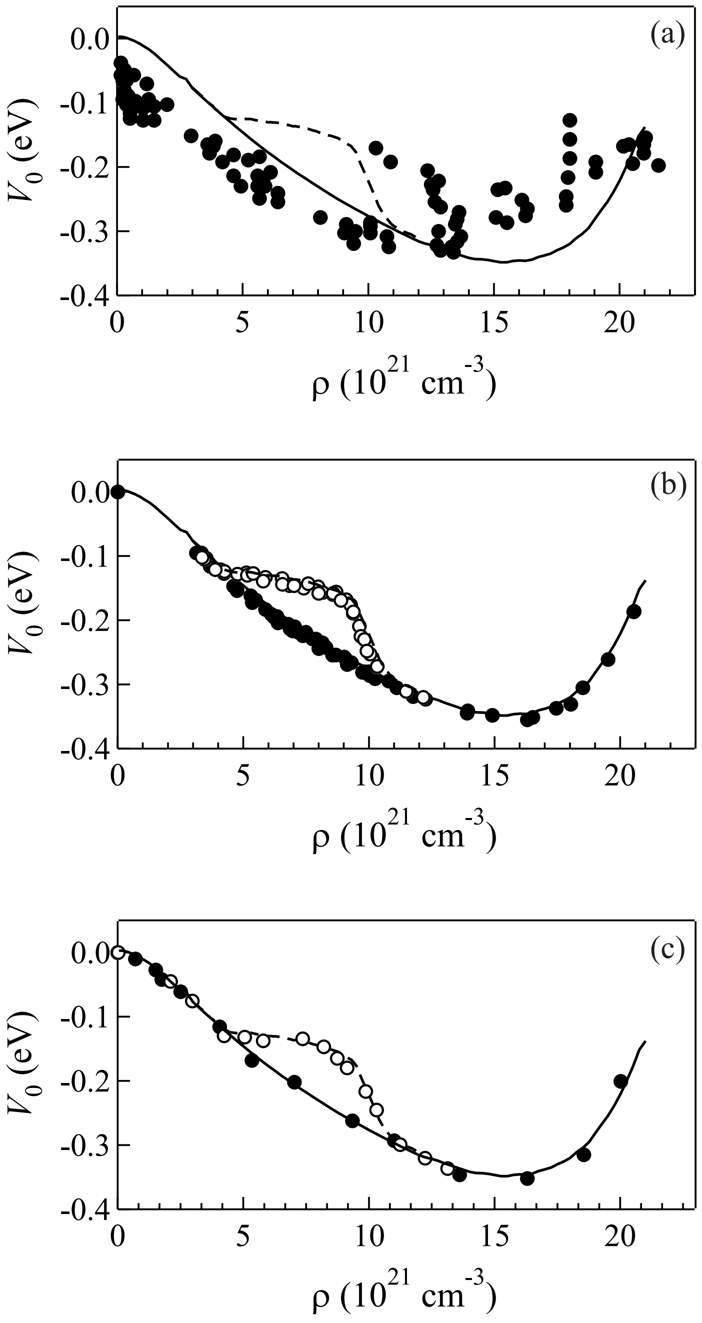

Figure 3.7: The quasi-free electron energy $V_0(\rho)$ in argon determined using (a) photoemission [30–32], (b) dopant field ionization [50–52] and (c) field enhanced photoemission [46]. Solid markers represent data obtained on noncritical isotherms while open markers represent data obtained on an isotherm near the critical isotherm. The lines are a local Wigner-Seitz calculation [50–52].

(i.e., crystal constituent) in question than to other lattice points. A Wigner-Seitz cell is a polyhedron the faces of which are constructed from planes bisecting lines between the lattice point in question and the neighboring lattice points. The symmetry of the crystal allows one to determine the energy of the system by solving the Shrödinger equation in one Wigner-Seitz cell rather than in the entire crystal. Commonly, the polyhedral cells are replaced with spheres of the same volume. The radius of the spherical cell is determined from the bulk density ρ of the crystal via [79, 80, 95]

$$r_s = \left(\frac{3}{4\pi\rho}\right)^{1/3} . \tag{3.29}$$

A one-electron potential V within a Wigner-Seitz cell is now a spherically symmetric potential $V(r)$ with a translational symmetry [79, 80, 95]

$$V(r) = V\,(r + 2r_s)\ . \tag{3.30}$$

Of course, when the Wigner-Seitz model is applied to a dense fluid the periodicity of constituents is lost and eq. (3.30) becomes an average translational symmetry. Because of this symmetry, however, the derivative of the electron wavefunction vanishes at the boundary of the Wigner-Seitz sphere. Therefore, one can solve

$$\nabla^2\psi + \frac{2m}{\hbar^2}[V_0 - V(r)]\psi = 0 \tag{3.31}$$

with the boundary condition

$$\left(\frac{\partial\psi}{\partial r}\right)\bigg|_{r=r_s} = 0 \tag{3.32}$$

to obtain the wavefunction in every cell along with the ground state energy of the quasi-free electron. (We use scattering boundary conditions rather than the one in eq. (3.32) to solve eq. (3.31); see below for discussion.) The choice of $V(r)$ separates the different Wigner-Seitz based approaches to modeling $V_0(\rho)$.

3.3.2 Computer Simulation

A common approach to simulating an excess electron in a fluid is by treating the electron as a flexible ring of beads within Monte Carlo and molecular dynamics methods (see, e.g., [59, 81]). The fluid constituent interactions are modeled with an appropriate pairwise potential (usually Lennard-Jones) and the electron bead/fluid constituent interactions are treated with a pairwise pseudo-potential. These pairwise potentials allow one to determine the change in potential energy of the system due to the excess electron. The change in potential energy in conjunction with the kinetic energy of the electron ring gives the total change in energy due to the excess electron, or $V_0(\rho)$.

Since the electron is represented by a ring of beads, the position of the particle is somewhat uncertain, mimicking electron delocalization. The spatial spread of the electron beads can be examined in order to determine the extent of delocalization and to predict whether its ground state will be quasi-free or confined to a fluid cavity. The geometry of a cavity, given by the spatial positions of the fluid constituents, can be used to calculate the energy levels available to the confined electron by solving the Shrödinger equation for an electron in a spherically symmetric square well potential.

We are currently developing methods of measuring the energy of the electron cavity and thus will be using molecular dynamics to model electron cavities in a variety of dense fluid systems in the future. Since the energy of the quasi-free electron in a repulsive fluid is higher than the energy of an electron trapped in a cavity [59–65, 81], simulations discussed above tend to favor the more stable localized state. The quasi-free electron is therefore better modeled using the local Wigner-Seitz treatment, as discussed below.

3.3.3 Local Wigner-Seitz Model

A new approach, namely the local Wigner-Seitz model, was developed to describe the striking change in $V_0(\rho)$ observed in various near critical point fluids [45, 48–57]. This treatment has been very successful in modeling $V_0(\rho)$ in dense fluids from low density to the density of the triple point liquid, at both noncritical and near-critical temperatures, and owes its success to several key alterations to the Wigner-Seitz model. The main changes are the redefinition of the symmetry of the problem by an interaction radius determined locally rather than from the bulk density (i.e., eq. (3.29)), a sophisticated way of calculating the ensemble average polarization energy of the electron, a new choice in the definition of $V(r)$, an introduction of a thermal correction to the quasi-free electron energy, and finally, an introduction of a phase shift parameter that accounts for the local dynamic polarization of the fluid by the excess electron and reflects the scattering boundary condition used in determining the kinetic energy of the electron. Within the local Wigner-Seitz model [45–58],

$$V_0(\rho) = P_-(\rho) + E_k(\rho) + \frac{3}{2}k_B T \ , \tag{3.33}$$

where $P_-(\rho)$ is the ensemble average electron/fluid polarization energy, $E_k(\rho)$ is the zero-point kinetic energy of the quasi-free electron, and $(3/2)k_B T$ is the thermal energy of the quasi-free electron. It is important to note that the only direct temperature dependence of $V_0(\rho)$ comes from the thermal correction. This was experimentally shown to be correct in [56]. The ensemble average electron/fluid polarization energy is calculated similarly to the dopant core/fluid polarization energy $P_+(\rho)$ outlined in eqs. (3.3) - (3.5) [45, 49, 50], under the assumption that the quasi-free electron moves much faster than the individual fluid constituents:

$$P_-(\rho) = -4\pi\rho \int_0^\infty g(r)\, w_-(r)\, r^2\, dr \ , \tag{3.34}$$

where $g(r)$ is the fluid radial distribution function, and $w_-(r)$ is the electron/fluid interaction potential. The radial distribution function is determined by direct integration of the Orstein-Zernike relation with a Percus-Yevick closure [83] using the appropriate fluid /fluid potential (see Chapter 5 for a discussion of the potentials chosen for the systems presented in this work). The electron/fluid interaction potential is given by [84]

$$w_-(r) \;=\; -\,\frac{1}{2}\,\alpha\, e^2 \,\sum_i^N r_i^{-4}\, f_-(r_i) \ , \tag{3.35}$$

where r_i is the distance to the ith fluid constituent and $f_-(r)$ is a screening function given by [84]

$$f_-(r) = 1 - \alpha\pi\rho \int_0^\infty ds\, \frac{1}{s^2}\, g(s) \int_{|r-s|}^{r+s} dt\, \frac{1}{t^2}\, f_-(t)\, \theta(r,s,t) \ , \tag{3.36}$$

which, similarly to $f_+(r)$ in eq. (3.4), accounts for the repulsive interactions between dipoles in the fluid induced by the excess electron. (In eq. (3.36), θ is defined again by eq. (3.6).) Any critical point behavior in $P_-(\rho)$ arises from variations in $g(r)$ near the critical density and temperature.

The zero-point kinetic energy $E_k(\rho)$ is obtained from solving the Schrödinger equation for the quasi-free electron in a dense fluid [45, 47, 49–58, 88]

$$\nabla^2\psi \;+\; \frac{2m_e}{\hbar^2}\left(V_0(\rho) \;-\; \frac{3}{2}k_BT \;-\; V(r)\right)\psi \;=\; 0 \ , \tag{3.37}$$

where $V_0(\rho)$ is given by eq. (3.33) and $V(r)$ is the spherically symmetric potential that describes the interaction of the electron and the neat fluid. The solution makes use of scattering boundary conditions, where the minimum electron-fluid constituent distance is given by the zero kinetic energy electron scattering length A of the fluid (cf. Chapter 2), and the maximum distance is given by the average fluid constituent/fluid constituent separation. The local Wigner-Seitz model assumes that [45, 48]

$$V(r) \;=\; P_{-}(\rho) \;+\; V_{loc}(r) \;, \tag{3.38}$$

with $P_{-}(\rho)$ given by eq. (3.34) and with $V_{loc}(r)$ being a short-ranged dynamic polarization potential of the fluid. Using the definitions of $V_0(\rho)$ and $P_{-}(\rho)$ given by eqs. (3.33) and (3.34), eq. (3.37) can be rewritten as [45, 48]

$$\nabla^2\psi \;+\; \frac{2m_e}{\hbar^2}\left(E_k(\rho) \;-\; V_{loc}(r)\right)\psi \;=\; 0 \;. \tag{3.39}$$

At this point, it is helpful to define a wavevector

$$k_0 \;\equiv\; \frac{\sqrt{2m_e E_k}}{\hbar} \;, \tag{3.40}$$

which allows one to write the asymptotic solution to eq. (3.39) as [45, 48]

$$\psi(r) \;\sim\; \frac{1}{r}\,\sin(k_0 r \;+\; \eta_0) \;, \tag{3.41}$$

where η_0 is the phase shift caused by the short ranged dynamic potential $V_{loc}(r)$.

As mentioned in Chapter 2, at high densities the minimum distance between the excess electron and a fluid constituent is given by the absolute value of the zero kinetic energy electron scattering length $|A|$, while the translational symmetry of the model determines the maximum interaction distance. Since a dense fluid is not homogenous, especially near the critical point, an interaction range determined locally is more accurate than one determined from the bulk density ρ. With this in mind, since the local density $\rho(r)$ is given by [45, 97, 98],

$$\rho(r) \;=\; \rho\, g(r)\;, \tag{3.42}$$

the maximum interaction distance becomes, [45–47, 49–55, 57, 58]

$$r_\ell \;\equiv\; \left(\frac{3}{4\pi g_{max}\rho}\right)^{1/3} \tag{3.43}$$

where g_{max} is the maximum of the neat fluid radial distribution function. (We are assuming that interactions in the first solvent shell dominate.) Thus, the local Wigner-Seitz radius r_ℓ corresponds to half of the distance between two neighboring fluid constituents in the first solvent shell of the fluid, and the total range r_b for the local potential V_{loc} is defined by [45, 48]

$$r_b \;=\; r_\ell \;-\; |A|\;. \tag{3.44}$$

As with the Wigner-Seitz model, the average translational symmetry requires that

$$V_{loc}(r) \;=\; V_{loc}\,(r \;+\; 2r_b)\;. \tag{3.45}$$

Applying this boundary condition to the asymptotic wavefunction in eq. (3.41) yields [45, 48]

$$\sin\left(k_0 r \;+\; \eta_0\right) \;=\; \sin\left[k_0(r \;+\; 2r_b) \;+\; 3\eta_0\right]\;. \tag{3.46}$$

Therefore [45, 48],

$$\eta_0 \;=\; m\pi \;-\; k_0(r_\ell \;-\; |A|) \tag{3.47}$$

relates the phase shift η_0, the wavevector k_0, and the scattering length A. If $m = 0$, eq. (3.47) becomes [45,48]

$$\eta_0 \;=\; -\, k_0\,(r_\ell \;-\; |A|)\;. \tag{3.48}$$

We can now define the zero-point kinetic energy of the quasi-free electron in eq. (3.40) as [45,48]

$$E_k(\rho) \;=\; \frac{\hbar^2 k_0^2}{2m_e} \;=\; \frac{\hbar^2 \eta_0^2}{2\,m_e(r_\ell - |A|)^2}\;. \tag{3.49}$$

Therefore, any critical point behavior in $E_k(\rho)$ will result from a change in r_ℓ near the critical density along the critical isotherm due to density fluctuations reflected in g_{max}. Eq. (3.49) allows the energy of a quasi-free electron in a dense fluid to be written as [45,48]

$$V_0(\rho) \;=\; P_-(\rho) \;+\; \frac{\hbar^2 \eta_0^2}{2\,m_e(r_\ell - |A|)^2} \;+\; \frac{3}{2}k_B T\;. \tag{3.50}$$

The dynamic phase shift η_0 is the only empirical parameter in the local Wigner-Seitz model. Provided that η_0 is accurately determined by fitting $V_0(\rho)$ to the experimental data obtained at noncritical temperatures and $P_-(\rho)$ and g_{max} are determined with appropriate fluid constituent/fluid constituent potentials, the critical point effect on $V_0(\rho)$ is accurately predicted by this model (cf. Chapter 5).

Chapter 4

Experiment

The experiments presented in this dissertation were performed on the 1 m Stainless Steel Seya-Namioka beamline (SS-Seya) located on bending magnet 5 at the University of Wisconsin Synchrotron Radiation Center (SRC). The monochromator is equipped with a high energy (5 – 35 eV) grating with a resolution of $\sim$ 10 meV in the spectral region of interest (5 – 12 eV). The photon flux from the monochromator was monitored for consistency using a Ni mesh intersecting the beam prior to its entry into the sample cell. The copper sample cell was mounted inside an ultra high vacuum sample chamber. The cell was equipped with a LiF or a MgF_2 window capable of withstanding up to 100 bar of pressure. The electric field was supplied by a Bertan Series 225 Current Limited High Voltage Power Supply capable of supplying a potential of up to 5000 V with a limit current of 0.5 mA. The sample chamber pressure was maintained in the 10^{-10} (lower temperatures) to 10^{-8} (higher temperatures) Torr range by an ion pump attached to the bottom of the chamber. The chamber is separated from the beamline by a differential pumping station and a safety valve set to close if the sample chamber pressure exceeds mid 10^{-8} Torr.

The monochromator is controlled by LabView software supplied by SRC. The software pauses to record the signal from the two Kiethley devices (reading the pho-

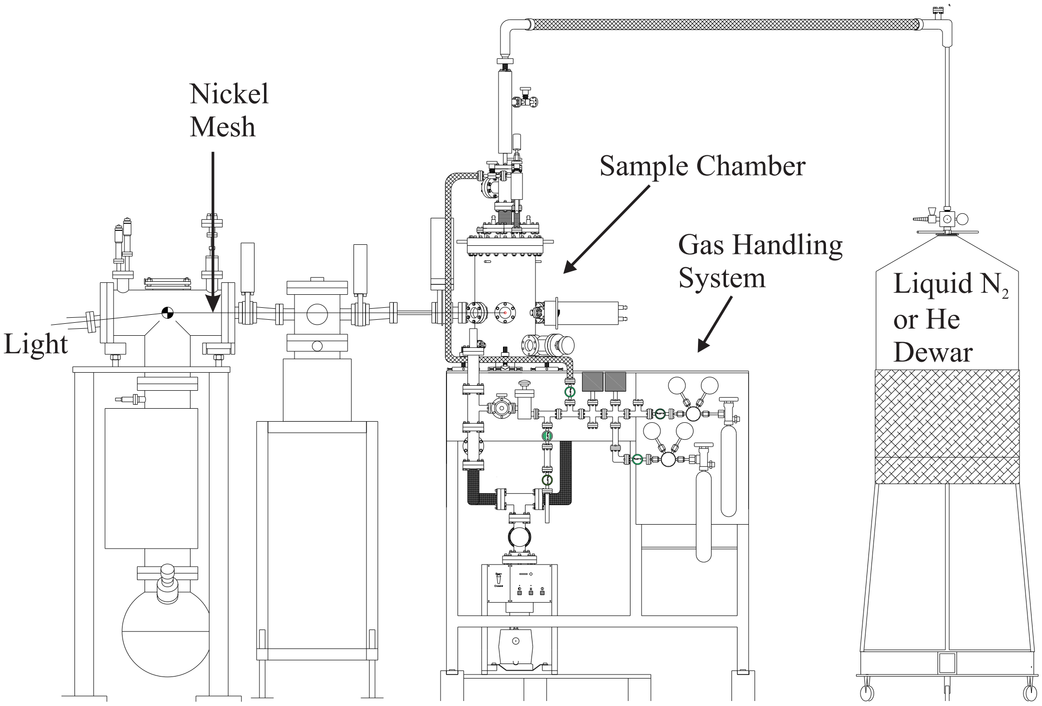

Figure 4.1: Schematic of the sample chamber used the experiments presented here. The experimental setup for the $V_0(\rho)$ measurements in He and N_2 employed a closed cycle cryostat and a XYZ manipulator mounted on the same chamber.

tocurrent from the Ni mesh and the cell, Figs. 4.1 and 4.2, respectively) before moving to the next monochromator step. The beam current in the SRC storage ring is also recorded. The output of the software is a text file containing the monochromator steps in various units, the beam current, and the readings from the two Kiethley devices. The text files are then transferred to another computer for analysis and long term storage.

4.1 Dopant Field Ionization

The dopant field ionization measurements presented here utilized the 3 mm cell, with 3 mm being the stainless steel electrode spacing. This cell (cf. Fig. 4.2a) is equipped with parallel MgF_2 windows and two parallel plate electrodes placed above and below

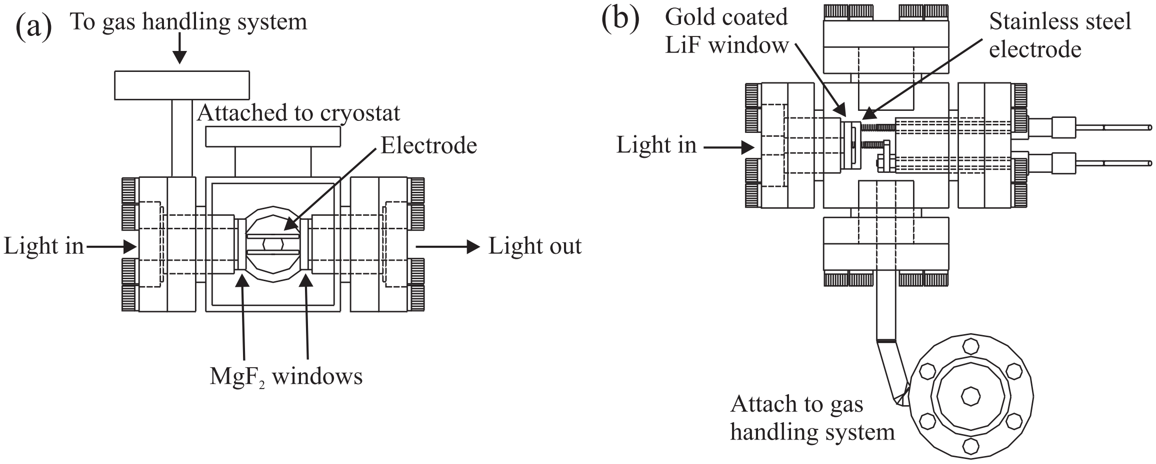

Figure 4.2: (a) Side view of 3 mm cell. (b) Top view of 1 mm cell. See text for discussion.

the path of the light, perpendicular to the windows. A voltage is applied to one of the electrodes, and the photocurrent is measured from the other one. 16,700 V/cm was the highest electric field achievable in the 3 mm cell since the high voltage power supply is capable of supplying a potential of ±5000 V to one of the electrodes. The photocurrent was measured using a Kiethley 485 picoammeter. Two spectra are taken at each fluid density, as is necessitated by the analysis procedure outlined in Chapter 3. These spectra are normalized by the output from the Ni mesh to account for beam current decay over time and for changes in monochromator flux.

Fig. 4.3 depicts a typical configuration of the gas handling system (GHS) used in field ionization measurements. (In order to elucidate the discussion below, the dense fluid being studied will be referred to as the perturber.) We should note here that if the dopant is a gas at room temperature, a small bottle of dopant is attached to the gas handling system via a regulator and a valve (similar to the way the perturber bottle is attached in Fig. 4.3).

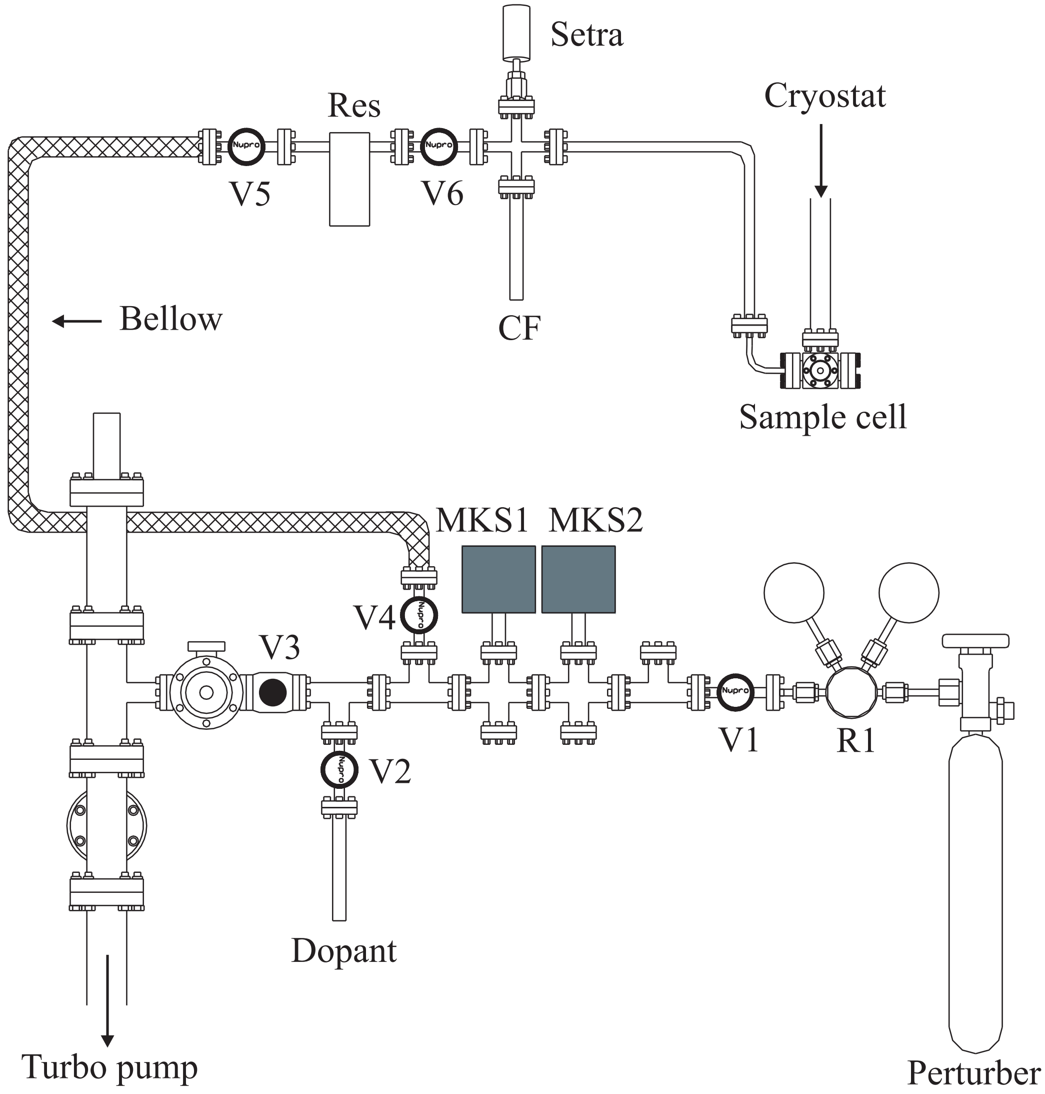

Figure 4.3: Schematic representation for a typical arrangement of the gas handling system. V1 - V6: valves; R1: dual stage regulator; MKS1: pressure manometer (maximum range: 10 mbar); MKS2: pressure manometer (maximum range: 1 bar); Res: reservoir; Setra: pressure manometer (maximum range: 200 bar); and CF: cold finger.

The dopant and the perturber are added in three stages. First, a small amount of dopant ($1 - 10$ mbar) is introduced into the sample cell and the cell closed at V6. The excess dopant is then evacuated by opening V3. Once the GHS has returned to an acceptable pressure (low 10^{-7} Torr), the perturber is added by pressurizing the GHS to the desired pressure. If necessary, a liquid nitrogen dewar is placed around the reservoir to collect more fluid and ultimately to achieve higher pressures in the cell than in the GHS. Finally, to ensure uniform dopant distribution in the sample, the sample is mixed: With V6 closed, a liquid N_2 dewar is placed around the cold finger in order to collect as much of the sample as possible, then the cold finger is warmed with a heat gun. This procedure is repeated three times. For a more detailed description of adding the perturber and the dopant, see [45, 76].

4.2 Field Enhanced Photoemission

The field enhanced photoemission experiments are performed in the 1 mm cell (cf., Fig. 4.2b). The 1 mm cell is equipped with either a MgF_2 or a LiF window. The window possesses a 10 nm thick strip of sputter deposited platinum along its diameter, which serves as the photoemitting electrode. The other electrode, placed in parallel configuration at a distance of 1 mm, is stainless steel. A positive potential of up to 5000 V (amounting to an electric field of 50 kV/cm in the cell) is applied to the stainless steel electrode, and the photocurrent is measured from the platinum strip with a Keithley electrometer (a Keithley 617 in the case of He and a Keithley 6514 in the case of N_2). Photon flux from the monochromator is additionally recorded in the spectral region of interest using a GaAsP photodiode placed in the path of the photons since the first photoemission threshold of the Ni mesh occurs in this spectral region. (The GaAsP photoresponse cannot be measured during a typical scan since the photodiode prevents the beam from entering the cell. This measurement is usually performed while the system is being baked.)

A minimum of four spectra is recorded at every fluid density. These spectra are normalized by the beam current in the SRC storage ring and then by the monochromator flux recorded using the photodiode. Minor changes in electron beam alignment in the SRC storage ring sometimes cause deviations from ideal radiation alignment in the SS-Seya. The mesh current is monitored during every scan in order to detect alignment problems.

To minimize errors arising from work function changes because of the uneven electrode surface as well as oxide and fluid coating, each electrode was characterized on every isotherm and every time a window was changed by obtaining and analyzing a set of spectra at a very low fluid number density ($\sim 1 \times 10^{20}$ cm^{-3}). The resulting photoemission threshold was treated as the reference work function ϕ_0 for a given temperature and fluid (cf. Section 3.3).

A similar gas handling system is used for field enhanced photoemission studies as that depicted in Fig. 4.3. Since no dopant is required, the addition of the fluid to the sample cell is rather straightforward and is accomplished by pressurizing the GHS to the necessary pressure while keeping the reservoir cool in order to use the least amount of gas to fill the cell.

4.3 Temperature Control

Both experimental methods discussed above require precise temperature control, especially while obtaining data on near critical isotherms. Near the critical point, small

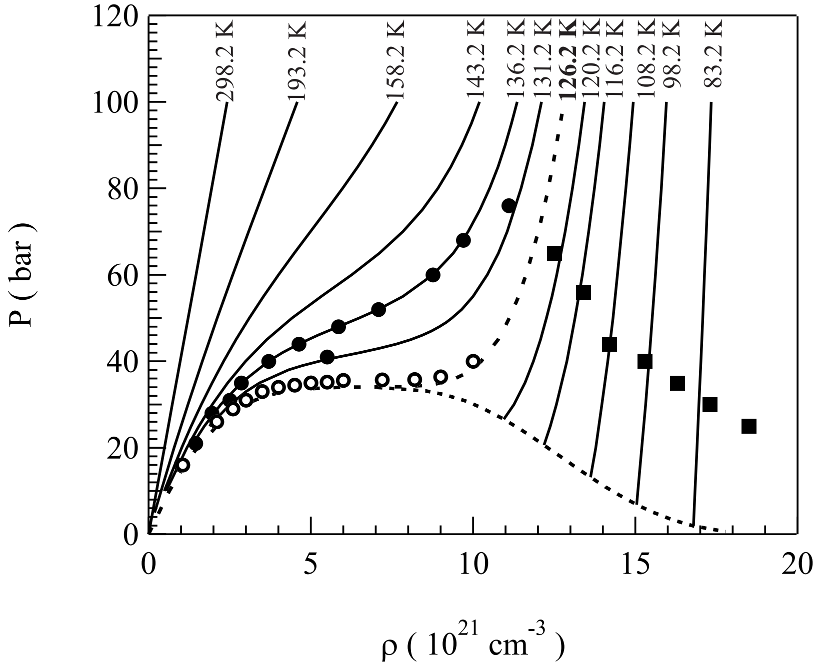

Figure 4.4: $P-\rho$ phase diagram of nitrogen showing several non-critical isotherms (—), the critical isotherm (- - -), and the vapor pressure curve (· · ·) [99, 103]. (●) and (■) present typical thermodynamic conditions for obtaining non-critical experimental data above and below the critical isotherm respectively, while (○) indicate the thermodynamic conditions for the experimental data obtained near the critical point.

changes in temperature produce pronounced shifts in the number density; thus, it is imperative to keep the temperature as stable as possible. Two cryostats, an open flow cryostat and a closed cycle cryostat (to be discussed below) were used in the experiments presented here. In both cases, the cell temperature was monitored at the bottom and top of the cell and regulated with a digital temperature controller. The controller adjusted the amount of current flowing through a resistive heater to reach and maintain the required temperature.

Fig. 4.4 depicts a prototypical $P-\rho$ phase diagram used to determine the temperatures and pressures required to obtain the desired number densities. The spectra that were recorded at number densities that can be reached with above-critical temperatures (shown as (●)), without exceeding 100 bar in the cell, were obtained on as few isotherms as possible. The spectra measured at number densities that required below-critical temperatures (shown as (■)) were recorded on separate isotherms since the isotherms in the latter region are steep and do not span a broad density range. The higher number of experimental points on the critical isotherm ensures that the critical point effect is well documented.

4.3.1 Open Flow Cryostat

The neon, argon and low density helium studies were performed using the open flow cryostat depicted in Fig. 4.1. The sample cell (cf. Fig. 4.2) was attached to a cryostat that simultaneously cooled with liquid nitrogen or helium and heated with a resistive heater. The temperatures below the cell and above the cell were measured using a Si diode and a Pt resistor, respectively, and were regulated by a Lakeshore 330 Autotuning Temperature Controller. This system was able to maintain temperatures to within ±0.5 K for most samples after initial stabilization. However, the difficulty of temperature stabilization near the critical density required temperatures to be maintained to within ±0.2 K. This was accomplished by manually controlling the flow of liquid cryogen.

4.3.2 Closed Cycle Cryostat

Since the above cryostat cannot attain a cell temperature below ∼77 K and ∼15 K with N_2 and He as coolants, respectively, and since liquid He is prohibitively expensive, an Advanced Research Systems DE-204SB 4K closed cycle ^{4}He cryostat was purchased and installed. This cryostat does not require manual flow control and maintains the cell temperature to within ±0.05 K. In the case of He, a near-critical temperature of 6.5 K ($T_c = 5.2$ K) was achieved by allowing the cell to cool for 24 hours, with a copper thermal shield surrounding the sample cell. The temperatures necessary to investigate N_2 did not require a thermal shield.

4.4 Sample Sources and Purities

4.4.1 Dopants

Methyl iodide (Sigma Aldrich 99.5%), nitric oxide (Matheson Gas Products, 99.995%), and oxygen (Matheson Gas Products 99.998%) were attempted as dopants in dense He and Ne. CH_3I, being a liquid at room temperature was outgassed by freezing with liquid nitrogen, evacuating the dopant cold finger volume above the solid with the turbo pump and thawing the dopant with a heat gun (this process was performed three times). NO and O_2 were used without further purification. The criteria for choosing these dopants were (1) an ionization energy below the cut-off energy of the crystal window (10.8 eV and 11.8 eV for MgF_2 and LiF, respectively) and (2) a sufficiently high vapor pressure at ambient temperature to allow introduction into the sample cell in ample quantity. O_2 was the most successful dopant used since it remained in solution at lower temperatures (cf. Chapter 5 for a detailed discussion of dopant field ionization in Ne and He). All dopants were tested for impurities in the spectral region of interest by photoabsorption or photoionization.

Table 4.1 contains the first gas phase ionization energy and the field ionization constant for the dopants used in the work presented here. Note that the first ionization energy of O_2 is higher than the energy cut-off of both available window materials. All of the measurements utilizing oxygen as a dopant required a temperature below 73

Table 4.1: The first ionization energy I_g and the field ionization constant c_0 for all the dopants involved in the experiments presented here.

Dopant	(eV) I_g	(eV cm$^{1/2}$ V$^{-1/2}$) c_0
CH_3I	9.538 ± 0.005	$4.3 \pm 0.1 \times 10^{-4}$
O_2	12.065 ± 0.005	$4.2 \pm 0.7 \times 10^{-4}$
NO	9.254 ± 0.003	$3.0 \pm 0.2 \times 10^{-4}$

K [57] to maintain a photoionization signal, since the window cut-off shifts to higher energies as the temperature is lowered.

4.4.2 Fluids

Neon (99.9995% Matheson Gas Products, used with CH_3I as dopant and 99.999% Airgas, used with O_2 and NO), argon (Matheson Gas Products 99.9999%), Helium (Matheson Gas Products 99.9999%) and nitrogen (Matheson Gas Products and Airgas, 99.9999%) were used without further purification. Prior to any measurements, the system was baked at 80 °C so that a base pressure of low 10^{-8} or high 10^{-9} Torr at room temperature could be achieved. All fluids were checked for impurities in the spectral region of interest by photoabsorption or photoionization.

The number density of the fluid being investigated was determined for each photoionization or photoemission spectrum from the temperature and pressure in the cell using the Strobridge [99] equation of state (EOS). The coefficients for Ne, Ar, He, and N_2 were obtained from [100], [101], [102], and [103], respectively. The EOS was used to construct a phase diagram such as that shown in Fig. 4.4, which determines the pressures and temperatures required for measurements.

Chapter 5

Quasi-Free Electron Energy in Repulsive Fluids

In this chapter, we present the quasi-free electron energy in He, Ne and N_2. $V_0(\rho)$ in Ne was extracted from field ionization of O_2. This was the first extensive study of $V_0(\rho)$ in a repulsive fluid and served as a test of the local Wigner-Seitz model. In Section 5.1.2, we discuss attempts to measure the quasi-free electron energy in helium with dopant field ionization as well as why these attempts ultimately met with failure. The sections that then follow present $V_0(\rho)$ in helium and nitrogen obtained by field enhanced photoemission. All experimental data were successfully modeled by the local Wigner-Seitz approach (cf. Section 3.3.1).

5.1 Atomic Fluids

5.1.1 Dopant Field Ionization: Neon [57]

Our group and others previously investigated the quasi-free electron energy in Ar [38, 39, 41, 43, 51, 52, 55], Kr [40, 42, 53, 55], and Xe [42, 54, 55]. The critical point effect observed by us in these fluids allowed for the development of the local Wigner-Seitz model [48–57, 82] that accurately predicts the behavior of $V_0(\rho)$ across a wide density and temperature range. The three rare gases studied previously, however, are attractive. Neon, on the other hand, possesses a small but positive zero kinetic energy electron scattering length (cf. Table 2.1), making it slightly repulsive and a perfect system in which to evaluate the applicability of the local Wigner-Seitz approach to repulsive fluids.

In general, there is a dearth of reliable $V_0(\rho)$ data for repulsive fluids because of the previously discussed experimental difficulties attendant upon the low temperatures and high pressures required to obtain higher number densities. Neon was a very good entry point into the realm of repulsive fluids since its critical temperature is 44.4 K, which can be reached with an open cycle He cryostat. Combined with the right choice of dopant, a field ionization study of neon was possible.

We used field ionization of high-n O_2 Rydberg states in order to determine the O_2 ionization threshold in Ne with minimal scatter across a density range from low Ne density to the density of the triple point liquid (cf. Section 3.2.1 for a detailed discussion of the dopant field ionization method). The applied electric fields were optimized to produce the best field ionization signal for each Ne density, with $F_L = 4.6 - 8.3$ kV/cm and $F_H = 8.3 - 13$ kV/cm. (Since the time scale required for electron localization [104] in these high electric fields is significantly longer than that for the dopant photoionization process, electron localization in Ne does not occur during these measurements. O_2 can form a stable negative ion in some solvents [105], with a rate constant that depends both on the solvent density and on the electric field strength. At the electric field strengths chosen for this experiment, we observed no changes in the field ionization spectra indicative of negative ion formation.) All

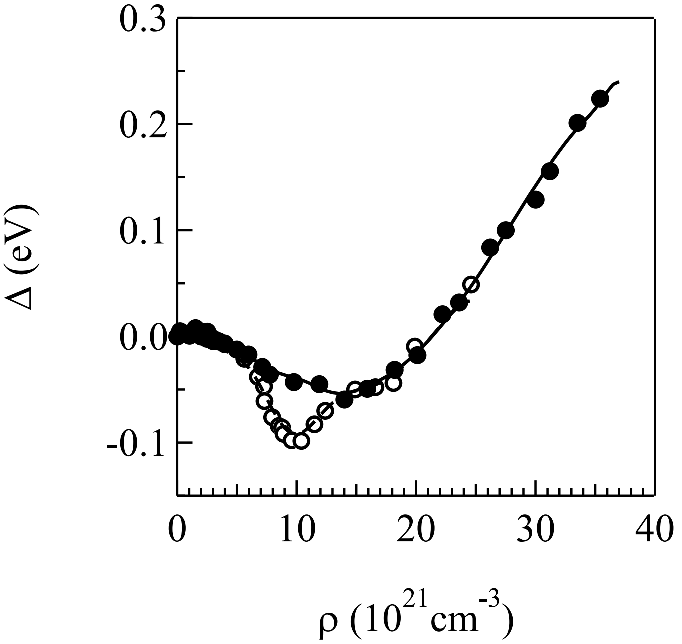

Figure 5.1: Ne induced shift $\Delta(\rho)$ of the O_2 ionization energy as a function of Ne number density ρ. (●) and (○) represent data obtained at noncritical temperatures and on an isotherm near the critical isotherm, respectively. The lines result from a fit to the local Wigner-Seitz model, as discussed below. The markers are approximately the size of the total experimental error.

measurements were performed at temperatures below 73 K in order to shift the energy cut-off of the LiF window to above the ionization energy of O_2.

Fig. 5.1 shows $\Delta(\rho)$ as a function of Ne number density ρ. The total error for these measurements is given by a sum of the field correction error, the quality-of-fit error (for fitting a field ionization spectrum to a Gaussian line shape), and the error arising from the energy uncertainty due to the resolution of the monochromator in the spectral region of interest (i.e., ±5 meV). The total experimental error is between 15 and 25 meV for the entire density range.

Although field ionization allows one to determine the fluid induced shift $\Delta(\rho)$ accurately at all Ne number densities, this shift does not represent the quasi-free

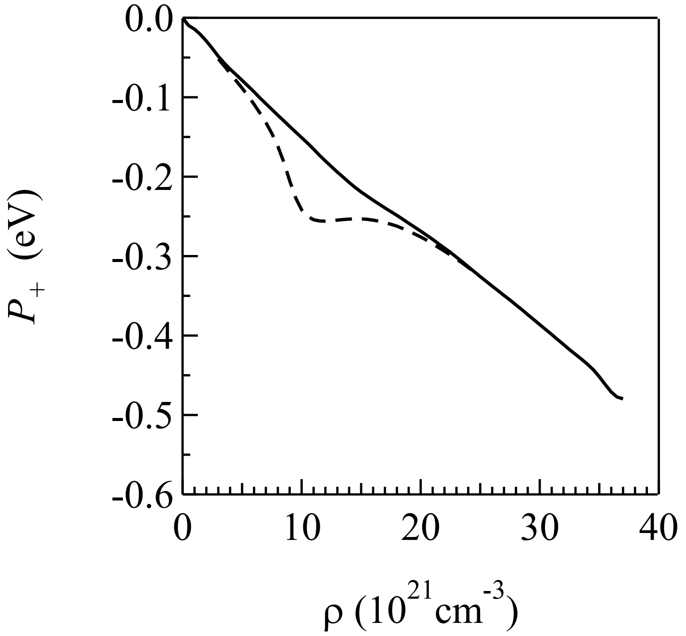

Figure 5.2: The ensemble-averaged O_2^+/Ne polarization energy $P_+(\rho)$ calculated from eq. (3.3), as a function of Ne number density ρ. The solid and dashed lines represent calculations at noncritical temperatures and on an isotherm near the critical isotherm, respectively.

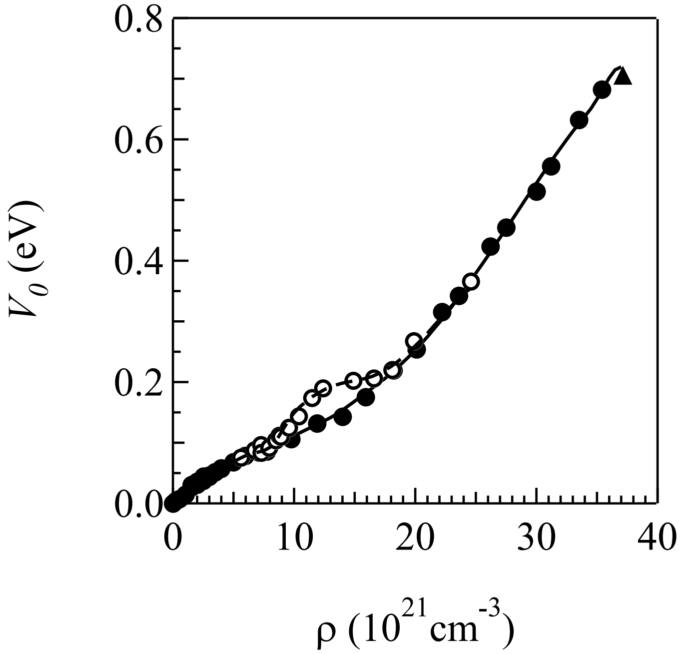

Figure 5.3: The quasi-free electron energy in $V_0(\rho)$ Ne as a function of Ne number density. Solid markers represent data extracted from eq. (5.1) for noncritical isotherms, while the open markers are data obtained on an isotherm near the critical isotherm (i.e., $T_r = T/T_c \leq 1.02$, where $T_c = 44.4$ K). (▲) represents a direct determination of $V_0(\rho)$ for the triple point liquid [36]. The lines are local Wigner-Seitz calculations (see text for discussion).

electron energy in $V_0(\rho)$. The relationship between $\Delta(\rho)$ and $V_0(\rho)$ is [48–57, 82]

$$V_0(\rho) \; = \; \Delta(\rho) \; - \; P_+(\rho) \; , \tag{5.1}$$

where $P_+(\rho)$ is the ensemble average O_2^+/Ne polarization energy given by eq. (3.3). The O_2/Ne radial distribution function $g_{\mathrm{D}}(r)$ and the Ne/Ne radial distribution function $g(r)$ were calculated using the coupled Percus-Yevick equations [49, 83] for dilute binary systems using Lennard-Jones 6-12 potentials for both the Ne/Ne and O_2/Ne interactions. (The Ne/Ne potential parameters [106] were $\sigma = 2.782$Å and $\varepsilon/k_B = 37.3$ K. The O_2/Ne potential parameters were determined from the Sikora combining rules [45, 107], although small (i.e., $< 1\%$) adjustments were made in the parameters to obtain the best fit to experiment. The final O_2/Ne Lennard-Jones 6-12 potential parameters were $\sigma = 3.128$ Å and $\varepsilon/k_B = 50.5$ K.) $P_+(\rho)$ determined from eq. (3.3) is plotted as a function of Ne number density ρ in Fig. 5.2.

Fig. 5.3 presents $V_0(\rho)$ as extracted from the data of Fig. 5.1 using eq. (5.1) and the $P_+(\rho)$ of Fig. 5.2. Note that even though $\Delta(\rho)$ possesses a negative region in the $\rho_r < 20 \times 10^{21}$ cm^{-3} range as well as a negative critical point effect, $V_0(\rho)$ is very much positive across the entire density range (unlike $V_0(\rho)$ in the previously studied rare gases [48, 50–55]), and possesses a positive critical point effect similar to that observed in other rare gases (cf. 3.2). The negative region in $\Delta(\rho)$ can be attributed to an initial slow rise in $V_0(\rho)$ coupled with a steady negative $P_+(\rho)$. $P_+(\rho)$ is also responsible for the rather strong negative critical point effect on $\Delta(\rho)$. The increased fluid constituent clustering around O_2 at the critical point, combined with the fact that O_2 and Ne are both non-polar species, produces a strong reduction in $P_+(\rho)$.

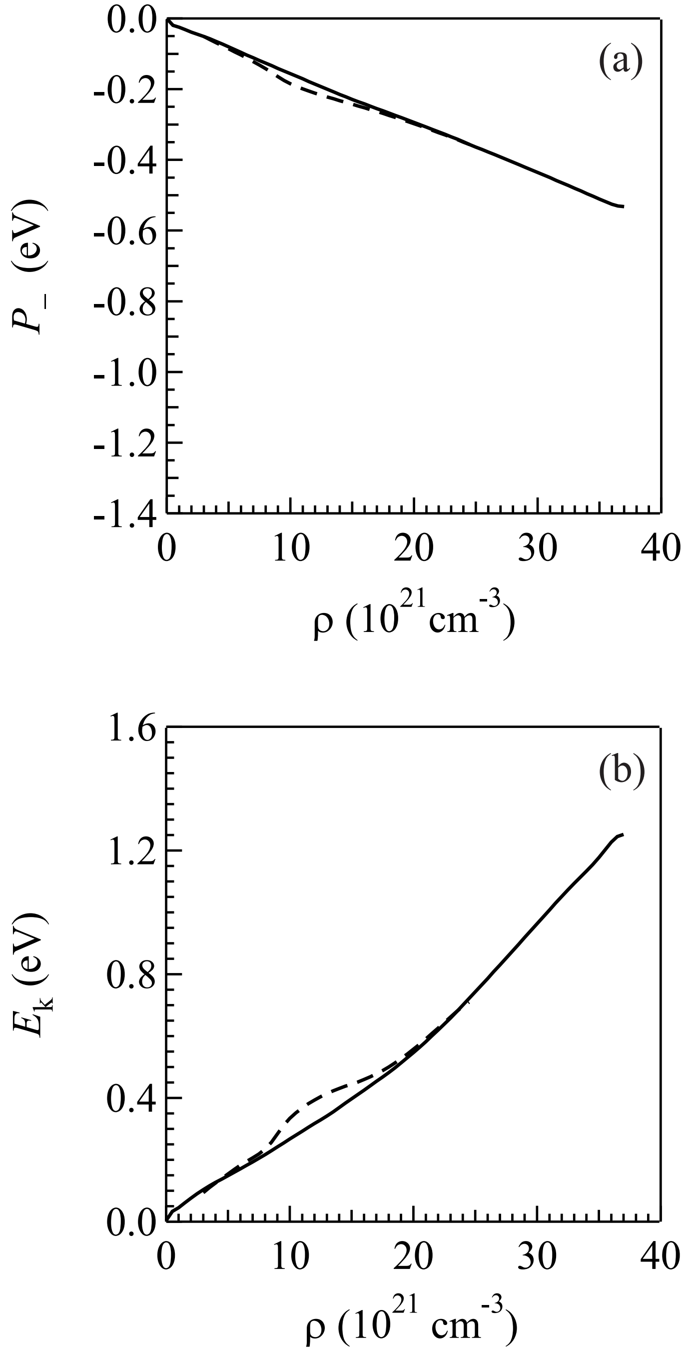

Figure 5.4: (a) The ensemble average electron/fluid polarization energy, and (b) the zero point kinetic energy of the quasi-free electron in Ne calculated using eqs. (3.34) and (3.49), respectively. The solid and dashed lines represent calculations at noncritical temperatures and on an isotherm near the critical isotherm, respectively.

The lines in Fig. 5.3 are the results of the local Wigner-Seitz calculations using eq. (3.33), with the $P_{-}(\rho)$ and $E_k(\rho)$ functions evaluated from eqs. (3.34) and (3.49) and displayed in Figs. 5.4a and 5.4b, respectively. The scattering length and the phase shift necessary for determining $E_k(\rho)$ were $A = 0.10$ Å [69] and $\eta_0 = 0.65$, respectively. ($V_0(\rho)$ was also modeled at selected densities using a Morse potential [108] for the Ne/Ne interactions. This led to no appreciable improvement in the quality of the fit to the experimental data.)

The critical point effect seen here and in other fluids [48–57,82] previously studied can be explained as follows. The increased correlation length in the fluid at the critical point affects both $P_{-}(\rho)$ and $E_k(\rho)$, since they both depend on the radial distribution function $g(r)$ of the neat fluid. At the critical point, $g(r)$ exhibits an enhancement in its first peak followed by an increase in magnitude of the first dip. This reflects the increased fluid constituent clustering found at the critical point [29]. $P_{-}(\rho)$ is obtained from eq. (3.34) by integrating along the entire radial distribution function, and therefore the critical point effect on $P_{-}(\rho)$ is minor.

The zero-point kinetic energy $E_k(\rho)$ on the other hand, depends on the local density within the first solvent shell through the local Wigner-Seitz radius r_ℓ (which is half the average distance between two individual fluid constituents in the first solvent shell of the fluid). The magnitude $|A|$ of the electron scattering length represents the minimum distance between the electron and a single fluid constituent, while the local Wigner-Seitz radius represents the maximum distance between the electron and a single fluid constituent in the first solvent cell. Thus, $r_\ell - |A|$ gives the size of the "box" in which the quasi-free electron is confined during the electron/fluid constituent interaction. Around the critical point, the increased clustering of fluid constituents (marked by an enhancement in the first peak of $g(r)$) produces a smaller r_ℓ, severely limiting the box size. Since $E_k(\rho)$ is inversely proportional to this box size, the decrease in r_ℓ near the critical point (due to an increase in the local density) leads to a larger $E_k(\rho)$. The critical effect on $E_k(\rho)$ is rather large and always dominates any negative effect on $P_-(\rho)$.

Table 5.1 contains rare gas atomic data that, in conjunction with Figs. 5.4a and 5.4b, can be used to explain the strictly positive nature of $V_0(\rho)$ in Ne. Fig. 5.4a shows that the magnitude of the polarization energy $P_-(\rho)$ at the density of the triple point liquid is ~ -0.5 eV, which is significantly smaller than that for the attractive rare gases. This is due to the polarization volume α scaling of $P_-(\rho)$ (cf. eqs. (3.34) and (3.35)): The more polarizable heavier rare gases exhibit a much larger (in magnitude) $P_-(\rho)$. While $|A|$ is larger for attractive rare gases, the much larger atomic radii ensure that $r_\ell - |A|$ stays large, forcing a smaller $E_k(\rho)$. Therefore, $V_0(\rho)$ is strictly negative in the attractive rare gases [51–55]. A combination of a smaller $P_-(\rho)$ and a larger $E_k(\rho)$ are responsible for the strictly positive $V_0(\rho)$ in Ne and, as is discussed below, in other dense repulsive fluids.

Table 5.1: Properties of rare gases, where r_a is the atomic radius and ρ_t is the density of the triple point liquid.

Fluid	α (Å^3)	r_a (Å)	A (Å)	$P_-(\rho_t)$ (eV)	References
He	0.204	0.31	0.57	-0.19	[47, 70, 109]
Ne	0.392	0.38	0.090	-0.53	[57, 70, 109]
Ar	1.63	0.71	-0.82	-1.0	[51, 52, 73, 109]
Kr	2.46	0.88	-1.60	-1.1	[53, 70, 109]
Xe	4.01	1.08	-3.24	-1.6	[54, 77, 109]

Clearly, the local Wigner-Seitz model works equally well for the repulsive gas Ne as it does for the attractive gases [49–55], and fits the extracted $V_0(\rho)$ both for the noncritical temperatures and on an isotherm near the critical isotherm, thereby establishing the possible general applicability of the local Wigner-Seitz approach to repulsive fluids.

5.1.2 Failure of Dopant Field Ionization for Helium [56]

Previously, very few experimental studies of the quasi-free electron energy in dense He existed because of the difficulties inherent in obtaining accurate, low noise $V_0(\rho)$ data at low temperatures [46, 56, 110]. In fact, the only direct experimental studies of $V_0(\rho)$ are for liquid densities [111–116] or in low density He [110]. Since our group has experimentally determined $V_0(\rho)$ in other rare gases [50–57] and verified that the local Wigner-Seitz model applies to the repulsive fluid Ne [57], He–being the lightest rare gas and possessing a very repulsive electron-atom potential–was the next logical system to investigate.

Initially, we attempted to determine $V_0(\rho)$ in He across the entire density range from low density to the density of the helium gas/liquid helium I/liquid helium II triple point via dopant field ionization [56]. Ultimately, we were able to maintain a photoionization current up to a maximum helium density of 5×10^{21} atoms/cm^3. Methyl iodide, nitric oxide and oxygen were the dopants used. As can be seen from Fig. 5.5, no room temperature measurement was performed with $\rho > 3 \times 10^{21}$ atoms/cm^3. If one consults the phase diagram for He (cf. Fig. 5.6), it becomes clear that the room temperature isotherm is simply too steep, and densities larger than 3×10^{21} atoms/cm^3 cannot be reached with He pressures below 100 bar.

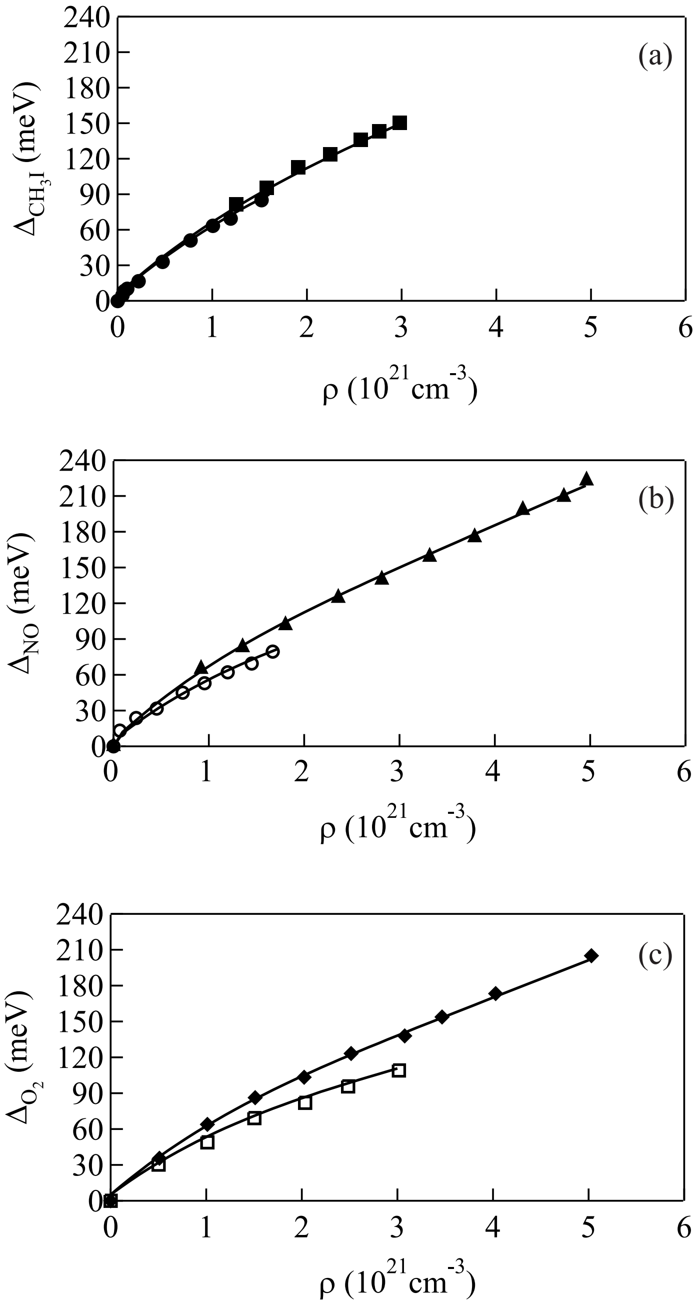

Figure 5.5: He induced shift $\Delta_{\mathrm{D}}(\rho)$ of the dopant ionization energy as a function of He number density ρ at various temperatures. D = CH_3I, NO and O_2. Temperatures are (●,○) 298 K, (■,□) 173 K, (▲) 93 K, and (◆) 73 K. The lines result from eq. (3.2) with $P_+(\rho)$ calculated from eq. (3.3) and $V_0(\rho)$ determined from eq. (3.33). The average total experimental error is $\sim$ 9 meV for all data points shown.

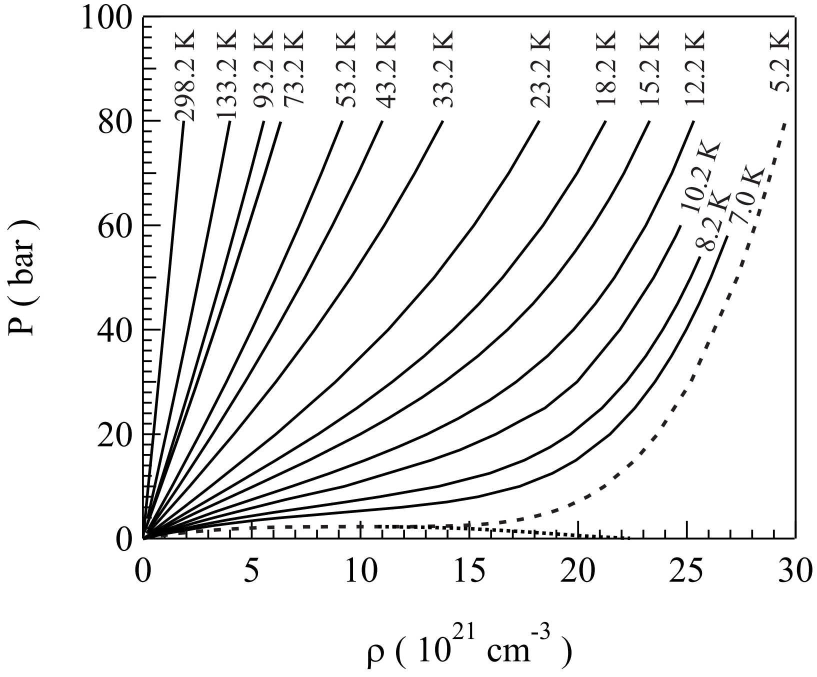

Figure 5.6: $P - \rho$ Phase diagram of He showing several non-critical isotherms (—), the critical isotherm (- - -) and the vapor pressure curve (· · ·).

We were able to measure the ionization energy shift of methyl iodide in He at a temperature of 173 K, but lost signal at lower temperatures indicating that CH_3I (which is a liquid at room temperature) was not soluble in He at low temperatures. As with the room temperature data, the $T = 173$ K isotherm reaches the pressure limit of the cell at a fairly low helium number density of 5×10^{21} cm^{-3}. Nitric oxide, which is a gas at room temperature and has a triple point at 109.50 K, maintained a photoionization signal at 93 K but again left the solution at lower temperatures.

Oxygen showed some promise as a dopant since it stayed in solution at $T = 73$K. However, due to the very positive $V_0(\rho)$ in He (cf. Section 5.1.3), the already relatively high ionization energy of oxygen crossed the LiF window cut-off energy at densities higher than $\rho = 5 \times 10^{21}$ atoms/cm^3.

Ultimately, there is no convenient way of determining the quasi-free electron energy in He and other repulsive gases using dopant field ionization. Hence, field enhanced photoemission (cf. Section 3.2.2), a technique that does not require a dopant, was developed in order to continue the study of $V_0(\rho)$ in repulsive fluids (as well as fluids that are opaque to vacuum ultraviolet light).

5.1.3 Field Enhanced Photoemission: Helium [47]

After field enhanced photoemission was developed and verified with argon [46], we made another attempt to determine $V_0(\rho)$ in He with this new technique. Since He possesses a very low critical temperature of 5.2 K, the closed cycle liquid He cryostat discussed in Section 4.3.2 was installed. With upgrades in place, we were able to obtain precise $V_0(\rho)$ data from low density to the density of the He gas/liquid He I/liquid He II triple point [47]. The work presented here is the first such study.

The noncritical photoemission measurements in He were performed on the $T =$ 14.7 K isotherm. Generally, more temperatures are required to span the entire density range of interest (cf. Fig. 4.4 for example). However, as one can readily see from Fig. 5.6, densities up to the triple point ($\rho_t = 22.4 \times 10^{21}$ atoms/cm^3) can be reached with above-critical temperatures without exceeding the 100 bar pressure limit of the sample cell. The near-critical temperature measurements were performed on the $T = 6.5$ K isotherm. (The near critical isotherm is selected to maximize temperature and pressure stability near the critical point and to minimize the possibility of forming a liquid in the sample cell.) Electric fields were chosen to maximize the field effect but to minimize the probability for electron localization, while not creating dielectric breakdown in the cell. Since the possibility of cavity formation may well increase near the He critical point, the electric fields chosen to measure FEP spectra on the critical isotherm were significantly higher than those used to obtain FEP spectra on the noncritical isotherm. (Schoepe and Rayfield [116] investigated field emission of electrons from helium bubbles (i.e., localized electron states) on the helium surface and concluded that the electric field required to extract a localized electron from a bubble in liquid helium is 150 V/cm at the gas/liquid interface. Thus, the electric fields for measuring field enhanced photoemission were selected to be significantly above this cut-off field threshold.)

Fig. 5.7 presents representative photoemission spectra of Pt in helium measured both at 14.7 K and at 6.5 K at various electric field strengths. Both at low density (e.g., Fig. 5.7a) and at high density (e.g., Fig. 5.7b), a distinct enhancement of the photocurrent as a function of electric field is observed. (The significant decrease in photocurrent between the low density and high density spectra is presumably caused by multiple scattering effects changing $B(T, \rho)$ in eq. (3.22).) Similar series of photoemission spectra were obtained at various helium number densities on the noncritical isotherm (14.7 K) and on the isotherm (6.5 K) near the helium critical temperature of 5.2 K.

Fig. 5.8 presents FEP spectra for the six possible pairwise differences that can be taken between the photoemission spectra shown in Fig. 5.7. Fitting these data with a linear least squares analysis to eq. (3.25) yields intercepts that are shown in Fig. 5.9, as a function of $\sqrt{\Lambda_H} + \sqrt{\Lambda_L}$, for various densities from low density to the density of the gaseous He/liquid He I/liquid He II triple point for the noncritical isotherm (cf. Fig. 5.9a) and for the near-critcal isotherm (cf. Fig. 5.9b). Extrapolating these

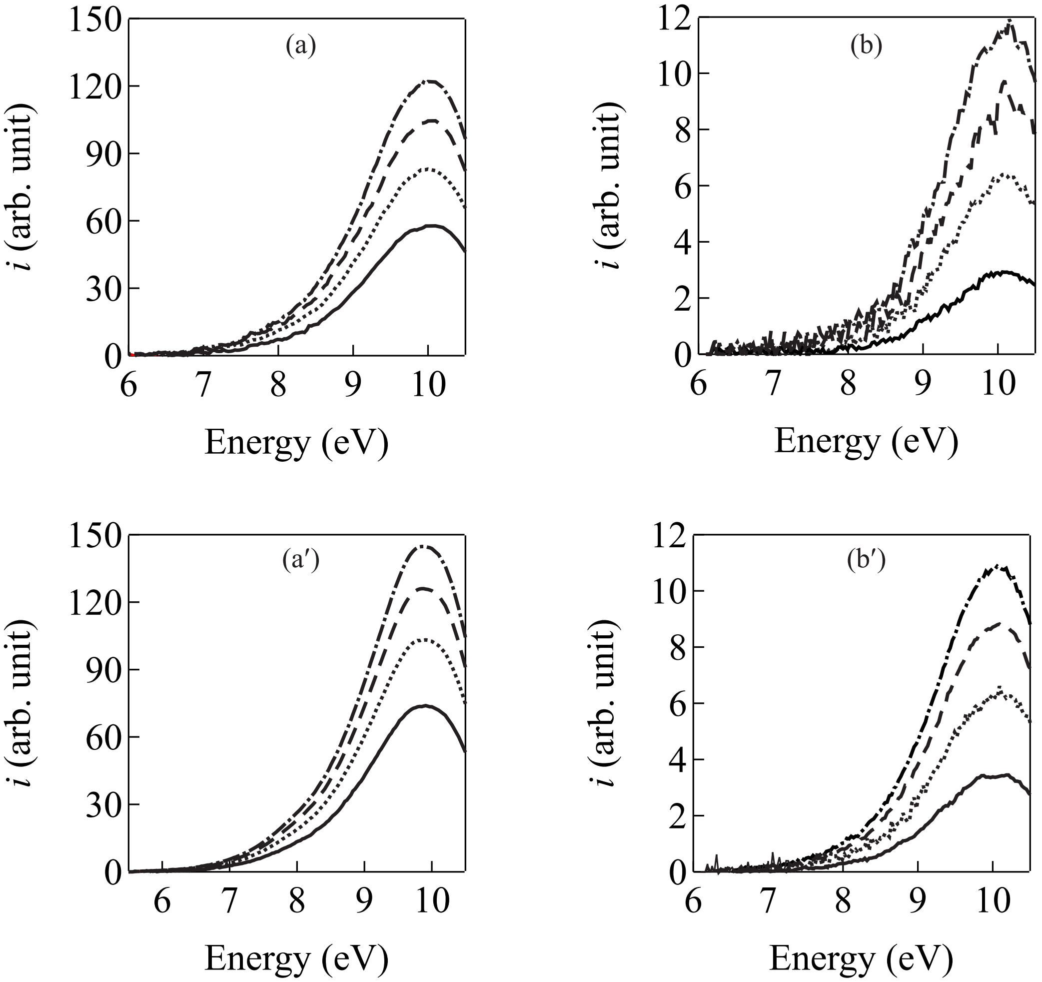

Figure 5.7: Photocurrent as a function of photon energy for helium number densities of (a, a′) 2.0×10^{20} cm^{-3} and (b, b′) 1.8×10^{22} cm^{-3} at temperatures of (a, b) 14.7 K and (a′, b′) 6.5 K, which is near the critical temperature of 5.2 K. In (a, a′) the applied fields are (—) 1.0 kV/cm, (· · ·) 2.0 kV/cm, (– –) 3.0 kV/cm and (– · –) 4.0 kV/cm. In (b) the fields are (—) 4.0 kV/cm, (· · ·) 7.5 kV/cm, (– –) 12 kV/cm and (– · –) 18 kV/cm. In (b′) the fields are (—) 6.0 kV/cm, (· · ·) 10 kV/cm, (– –) 15 kV/cm and (– · –) 20 kV/cm. (Note: The increased noise in (b) was caused by transient noise on the transmission line at SRC, which has since been reduced with a line filter. These spectra were not remeasured, however, since the noise was correctable.)

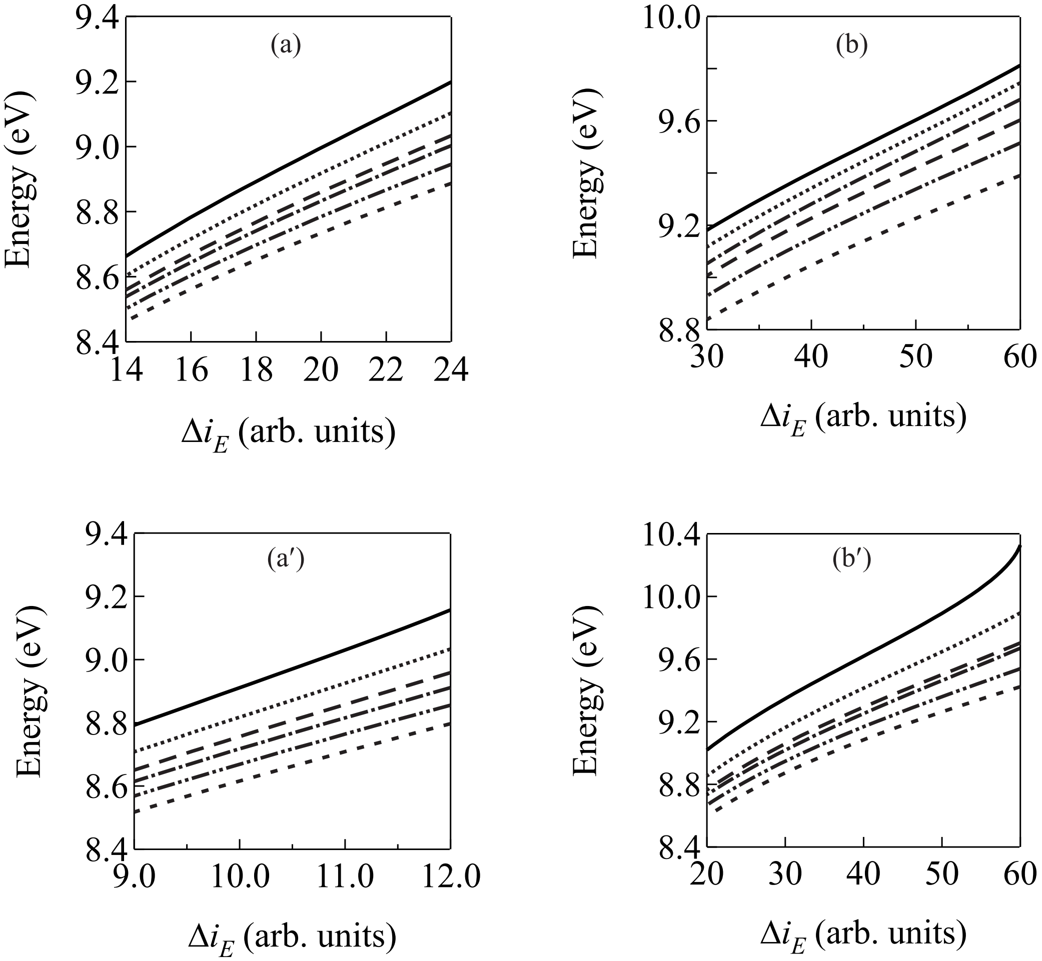

Figure 5.8: Photon energy as a function of $\Delta i_E(\rho)$ for helium number densities of (a, a′) 2.0×10^{20} cm^{-3} and (b, b′) 1.8×10^{22} cm^{-3} at temperatures of (a, b) 14.7 K and (a′, b′) 6.5 K, which is near the critical temperature of 5.2 K. The lines represent the differences in the spectra presented in Fig. 5.7, with the lowest set of fields given by (—) and the highest by (- -). Before taking the differences, each photocurrent spectrum was smoothed using a Gaussian algorithm [117], as implemented in Wavemetrics IgorPro, to reduce noise in the differences.

data sets to zero field yields the work function $\phi(\rho)$. The quasi-free electron energy $V_0(\rho)$ is then obtained from eq. (3.28).

$V_0(\rho)$ in He extracted from eq. (3.28) is presented in Fig. 5.10a as a function of He number density. Similar to $V_0(\rho)$ in Ne inferred from dopant field ionization studies [57], $V_0(\rho)$ in He is strictly positive. (An argument identical to the one presented in Section 5.1.1 can be used to explain why $V_0(\rho)$ in He is always positive.) Unlike the previous results in Ne [57], however, the critical point effect observed in He extends across a broader density range. Thus, the accurate modeling of He represents a significant test for the applicability of the local Wigner-Seitz model [49–57] to repulsive fluids.

The solid lines in Figs. 5.10a and 5.10b show $V_0(\rho)$ obtained from eq. (3.33) in comparison to the experimental data (markers) obtained from field enhanced photoemission (i.e., eq. (3.28)). For the calculations in Fig. 5.10b, the radial distribution functions were were determined using a Lennard-Jones 6-12 potential with parameters $\sigma = 2.556$ Å and $\epsilon/k_B = 10.22$ K. (These parameters were obtained by Aziz *et al.* [118] from fitting thermal conductivity data and viscosity data for He over an extended temperature range of 1.5 to 1475 K.) Unlike the other rare gases [50–55, 57], however, a Lennard-Jones 6-12 potential did not provide the best fit of the local Wigner-Seitz model to the experimental $V_0(\rho)$ data near the critical temperature of He, although this potential could be used to fit the experimental data at noncritical temperatures and densities. The best fit (cf. Fig. 5.10a, lines) of the local Wigner-Seitz approach to the experimental $V_0(\rho)$ data, both at noncritical temperatures and on an isotherm near the critical isotherm, required a more complex exponential-6

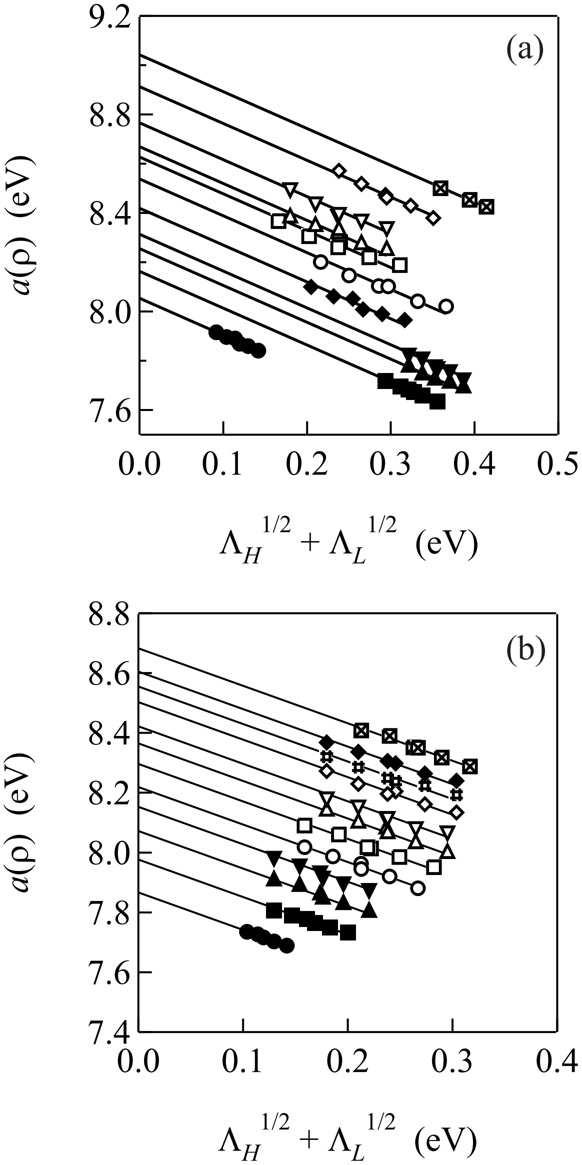

Figure 5.9: The intercept $a(\rho)$ of representative field enhanced photoemission plots (cf. Fig. 5.9, for example), measured at (a) 14.7 K and at (b) 6.5 K (which is near the critical temperature of 5.2 K), as a function of $(\sqrt{\Lambda_H} + \sqrt{\Lambda_L})$. The number densities range from (●) 2.0×10^{20} cm^{-3} to (☒) 2.4×10^{22} cm^{-3} in (a), and from (●) 2.0×10^{20} cm^{-3} to (☒) 1.8×10^{22} cm^{-3} in (b). Each line represents a linear least squares analysis with an intercept that yields $\phi(\rho)$. See text for discussion.

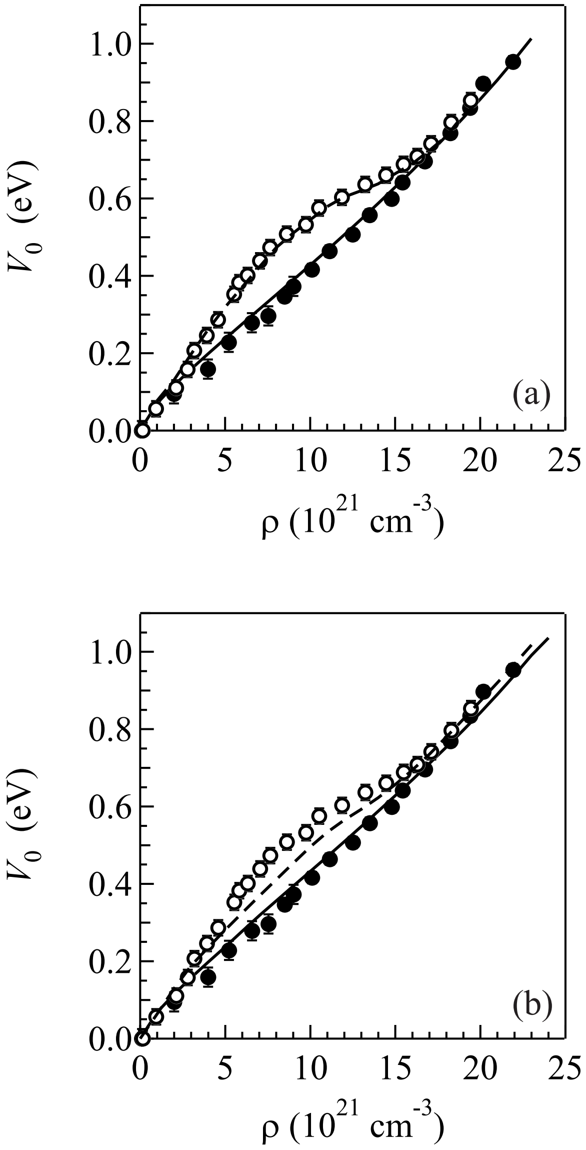

Figure 5.10: The quasi-free electron energy $V_0(\rho)$ in helium determined from eq. (3.28) with data obtained by the method discussed in Section 3.2.2. The solid markers represent data obtained at 14.7 K, while the open markers represent data obtained at 6.5 K, which is near the critical temperature of 5.2 K. The lines are a local Wigner-Seitz calculation with the helium/helium interaction modeled using (a) an exponential-6 potential [119] and (b) a Lennard-Jones 6-12 potential [118]. In the modeling of $V_0(\rho)$, $A = 0.63$ Å [120], (a) $\eta_0 = 0.78$ [47] and (b) $\eta_0 = 0.73$ [47]. See text for discussion.

potential $U(r)$ given by [119]

$$U(r) = \epsilon \left\{ \frac{6}{a-6} \exp\left[a \left(1 - \frac{r}{r_m} \right) \right] - \frac{a}{a-6} \left(\frac{r_m}{r} \right)^6 \right\} . \tag{5.2}$$

Young *et al.* determined $a = 13.1$ by fitting the equation of state of helium to very high pressure. The parameters $\epsilon/k_B = 10.8$ K and $r_m = 2.9673$ Å were determined by Aziz *et al.* [118] from fitting thermal conductivity and viscosity data to a Hartree-Fock dispersion potential, and used by Young *et al.* in the exponential-6 potential to fit the equation of state without need for adjustment. Therefore, the data in Figs. 5.10a and 5.10b not only show that the local Wigner-Seitz model can be extended to very repulsive systems, but also illustrate that the accurate modeling of the critical point effect in $V_0(\rho)$ within the local Wigner-Seitz framework can identify better pairwise intermolecular potentials for dense fluids.

Figs. 5.11a and 5.11b present (a) the ensemble average polarization energy $P_-(\rho)$ of He due to the excess electron and (b) the zero kinetic energy $E_k(\rho)$ of the electron in He computed from eqs. (3.34) and (3.49). The calculations were performed at 14.7 K (—) and at the near critical temperature of 6.5 K (- - -). One can immediately see the origin of the shape and sign of $V_0(\rho)$ in He. The always strictly positive zero-point kinetic energy overwhelms the negative $P_-(\rho)$ over the entire density range. The small atomic radius of He in conjunction with a rather large $|A|$ ensure a very strong $E_k(\rho)$, while the small polarizability of He ensures a very minor contribution from $P_-(\rho)$.

The local Wigner-Seitz approach was successful in modeling the quasi-free electron energy in He across all densities studied. The strikingly broad critical point effect on $V_0(\rho)$ is accurately predicted and is entirely due to the critical effect on the zero-

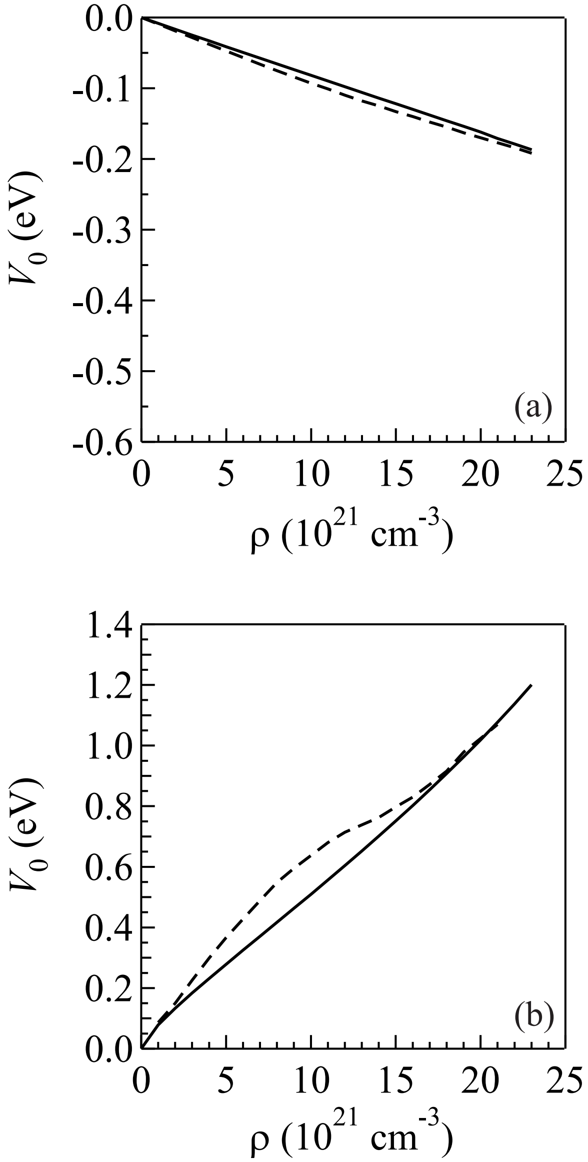

Figure 5.11: (a) The ensemble average electron/He polarization energy $P_{-}(\rho)$ calculated from eq. (3.34), and (b) the zero-point kinetic energy $E_k(\rho)$ obtained from eq. (3.49), as a function of He number density. The black and red lines represent calculations performed at 14.7 K and 6.5 K respectively.

point kinetic energy $E_k(\rho)$ of the quasi-free electron. It is of note that the width of the critical point effect on $V_0(\rho)$ in He is matched by the unusually wide region between the points of inflection (i.e., turning points) of the critical isotherm in the $P-\rho$ He phase diagram (compare Figs. 5.6 and 4.4).

5.2 Molecular Fluids

5.2.1 Nitrogen [58]

Having established field enhanced photoemission as a technique for measuring the quasi-free electron energy in repulsive fluids, and the local Wigner-Seitz approach as a suitable technique of modeling $V_0(\rho)$ in repulsive atomic fluids, our focus turned to nitrogen. We have determined $V_0(\rho)$ in attractive molecules in the past [45, 49] using dopant field ionization. The repulsive N_2 possesses a critical temperature of 126.2 K and would likely not pose a large problem with dopant solubility; however, it is not transparent to vacuum ultraviolet light. Thus $V_0(\rho)$ in N_2 could not be measured with dopant field ionization. The study discussed in this section is the first extensive profile of $V_0(\rho)$ in a repulsive molecular fluid and the first study for a VUV opaque fluid.

Similarly to He, very little experimental $V_0(\rho)$ data exist for N_2. There is a single published measurement of $V_0(\rho)$ determined from photoemission of an electrode in liquid nitrogen [36] that, as shown in Fig. 5.12, is at odds with an existing theoretical estimate by Sakai *et al.* [121] using

$$V_0(\rho) = \frac{2\pi\hbar A}{m_e}\rho + 35\,\frac{\alpha^2}{a_0 R_\alpha}\rho^2\ , \tag{5.3}$$

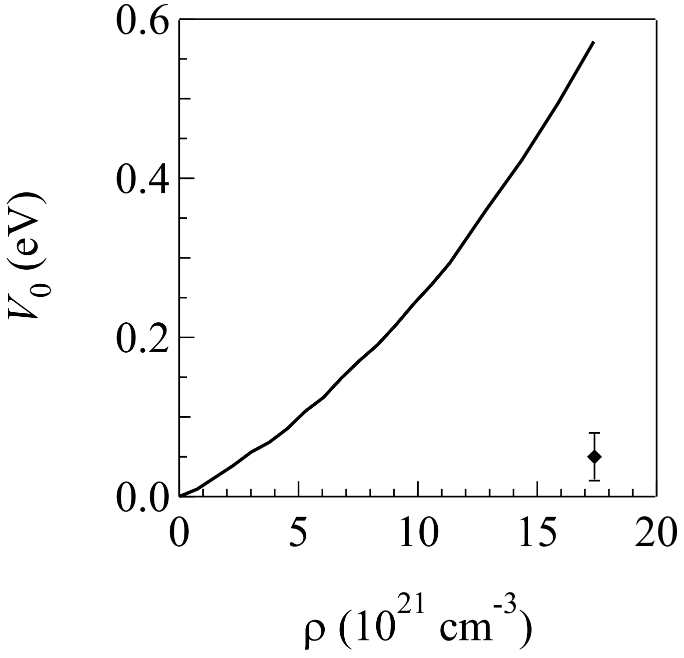

Figure 5.12: The quasi-free electron energy $V_0(\rho)$ in nitrogen as a function of nitrogen number density ρ. (♦) determined from photoemission [36] of an electrode immersed in liquid nitrogen at 77 K. (—) calculated from Eq. (5.3) [121].

where a_0 is the Bohr radius and R_α is a characteristic molecular radius estimated from $A \simeq (\alpha/a_0)^{1/2} \cot(\alpha/a_0 R_\alpha^2)^{1/2}$ [121]. From what we have seen with the quasi-free electron energy in myriad dense fluids, $V_0(\rho)$ cannot be reduced to a simple density dependent equation.

Figs. 5.13 – 5.15 present representative photoemission spectra of a platinum electrode immersed in fluid N_2 at various densities and temperatures and at various electric field strengths. From low density (e.g., Fig. 5.13a) to high density (e.g., Fig. 5.15b), a distinct enhancement of the photocurrent as a function of electric field is observed. Similar series of photoemission spectra were obtained at various nitrogen number densities at noncritical temperatures and on an isotherm near the critical isotherm.

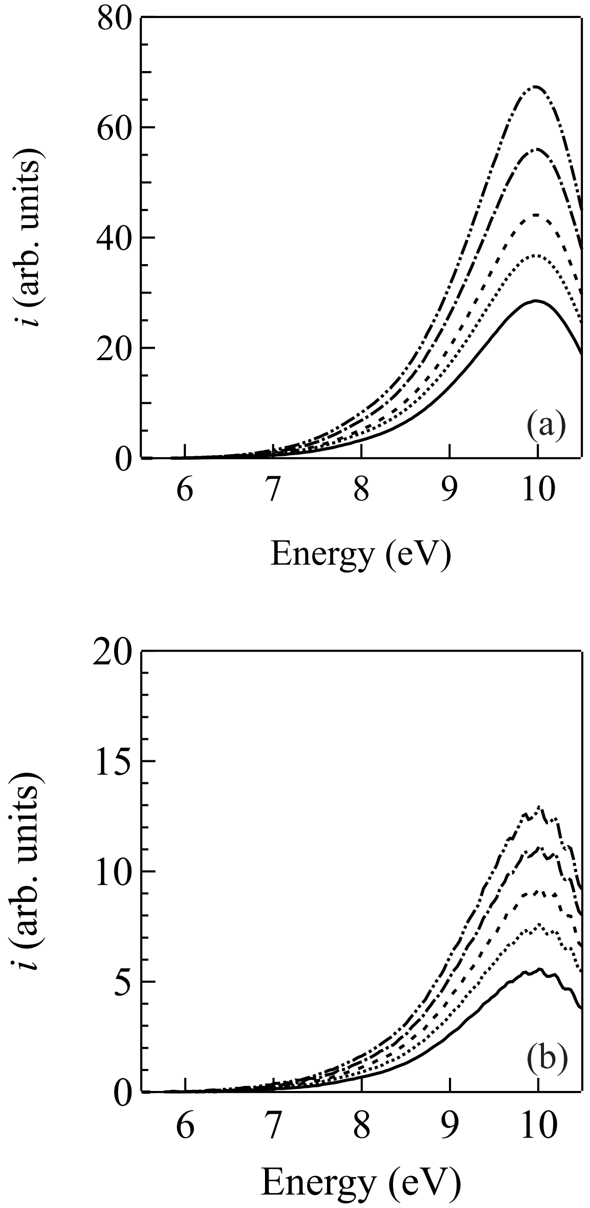

Figure 5.13: Photocurrent as a function of photon energy for N_2 number densities of (a) 0.6×10^{20} cm^{-3} and (b) 1.5×10^{21} cm^{-3} at the noncritical temperature of 132.0 K. In (a), the applied fields are (—) 1.0 kV/cm, (· · ·) 1.5 kV/cm, (– –) 2.0 kV/cm, (– · –) 3.0 kV/cm, and (– · · –) 4.0 kV/cm. In (b), the fields are (—) 4.0 kV/cm, (· · ·) 7.0 kV/cm, (– –) 10 kV/cm, (– · –) 14 kV/cm, and (– · · –) 18 kV/cm.

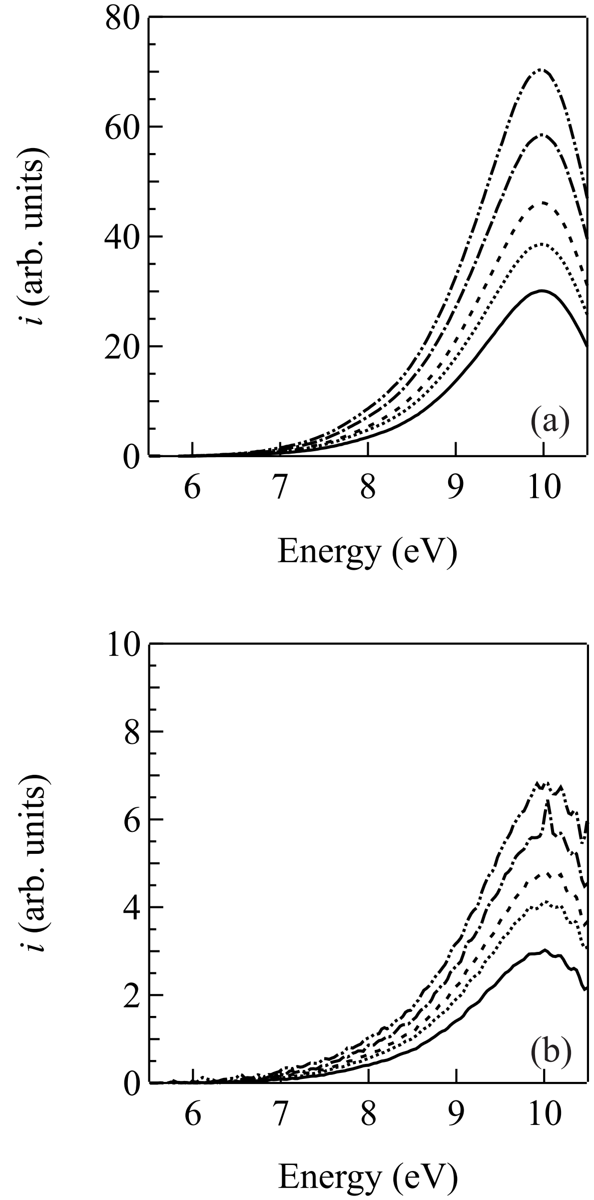

Figure 5.14: Photocurrent as a function of photon energy for N_2 number densities of (a) 0.6×10^{20} cm^{-3} and (b) 5.7×10^{21} cm^{-3} at near critical temperature of 127.0 K. In (a), the applied fields are (—) 1.0 kV/cm, (···) 1.5 kV/cm, (– –) 2.0 kV/cm, (– · –) 3.0 kV/cm, and (– · · –) 4.0 kV/cm. In (b), the fields are (—) 8.0 kV/cm, (···) 13 kV/cm, (– –) 18 kV/cm, (– · –) 25 kV/cm, and (– · · –) 32 kV/cm.

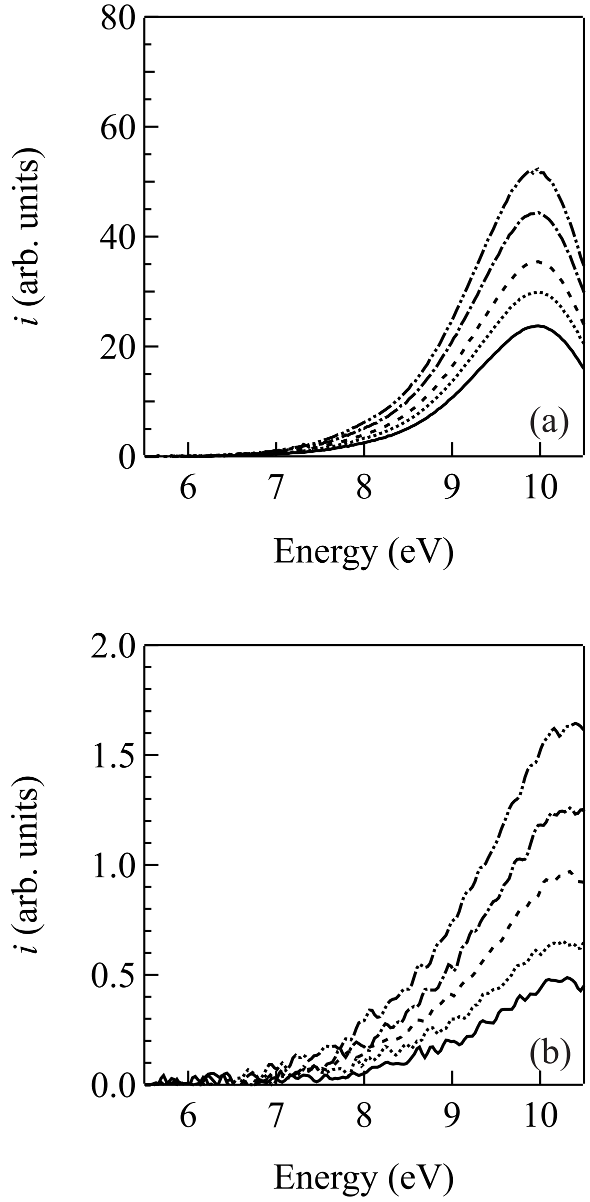

Figure 5.15: Photocurrent as a function of photon energy for N_2 number densities of (a) 0.6×10^{20} cm^{-3} and (b) 1.2×10^{22} cm^{-3} at the noncritical temperature of 123.0 K. In (a), the applied fields are (—) 1.0 kV/cm, (· · ·) 1.5 kV/cm, (– –) 2.0 kV/cm, (– · –) 3.0 kV/cm, and (– · · –) 4.0 kV/cm. In (b), the fields are (—) 13 kV/cm, (· · ·) 16 kV/cm, (– –) 20 kV/cm, (– · –) 25 kV/cm, and (– · · –) 31 kV/cm.

The electric fields for each density were chosen to maximize the signal to noise ratio and to maximize the electric field enhancement of the photocurrent, while minimizing electron localization in N_2 [121–124]. Thus, as the density increased and the temperature decreased, the electric fields applied across the cell also increased. At the highest N_2 densities, the minimum field applied was 26 kV/cm, while the maximum field was 50 kV/cm. In contrast, at low N_2 number densities, similar (or better) signal to noise ratios were obtained with electric fields between 4 kV/cm and 18 kV/cm. Thus, at these high field strengths (which are sufficient to prevent electron trapping), the significant decrease in photocurrent between the low density spectra and the high density spectra in Figs. 5.13 – 5.15 is caused by multiple scattering effects changing $B(T, \rho)$, rather than by electron localization in the fluid.

The spectra presented in Fig. 5.14, which were measured at the near critical temperature of 127.0 K, were obtained in succession to the data sets measured on the two noncritical isotherms of 132.0 K (e.g., Fig. 5.14) and 137.0 K. The small variance in the total photocurrent emitted from the electrode for the low density spectra (cf. Figs. 5.13a and 5.14a) indicates that oxide layer formation from any residual impurity in nitrogen is negligible. (The larger difference in the total photoemitted current in Fig. 5.15a in comparison to Figs. 5.13a and 5.14a was caused by the replacement of the Pt electrode between these measurements due to a crack in the MgF_2 window of the sample cell. When this occurs, the window (including the platinum electrode) is replaced. After baking the vacuum system to ensure a base pressure of low 10^{-8} Torr, new low density spectra are measured for the isotherm in question. Subsequently, these spectra are used to determine a reference ϕ_0 for the new electrode on the isotherm.)

After obtaining Δi_E from Eq. (3.24) for all possible pairwise differences between the photoemission spectra measured at various applied electric fields for each density, the linear regions in the Δi_E data were fitted by least squares analysis to eq. (3.25). Representative FEP intercepts $a(\rho)$ for the noncritical temperatures of 137.0 K and 132.0 K are shown in Figs. 5.16a and 5.16b, respectively, and the near critical temperature of 127.0 K in Fig. 5.16c, plotted as a function of $\sqrt{\Lambda_H} + \sqrt{\Lambda_L}$. (We should note here that figures similar to those presented in Fig. 5.16 also exist for data obtained at temperatures below the critical temperature, but are not shown for brevity. In addition, temperatures below the critical temperature were necessary to achieve densities above 11×10^{21} cm^{-3} while maintaining pressures below 80 bar, since the density change as a function of pressure is small in this thermodynamic region of the N_2 phase diagram (cf. Fig. 4.4). Therefore, only the low density data set (necessary for determining ϕ_0) and a single high density data set were measured for each isotherm below the critical isotherm.)

The quasi-free electron energy $V_0(\rho)$ in N_2 is presented in Fig. 5.17 as a function of N_2 number density ρ. As in the case of the repulsive atomic gases Ne [57] and He [47], but unlike the attractive molecular gases CH_4 [49] and C_2H_6 [49], the quasi-free electron energy in N_2 is strictly positive. However, unlike the quasi-free electron energy in repulsive atomic gases (cf. Figs. 5.3 and 5.10 for example), $V_0(\rho)$ in nitrogen has a significant curvature at medium number densities. Even with this curvature, a substantial critical point effect is observed. Upon comparing Figs. 5.3 and 5.17

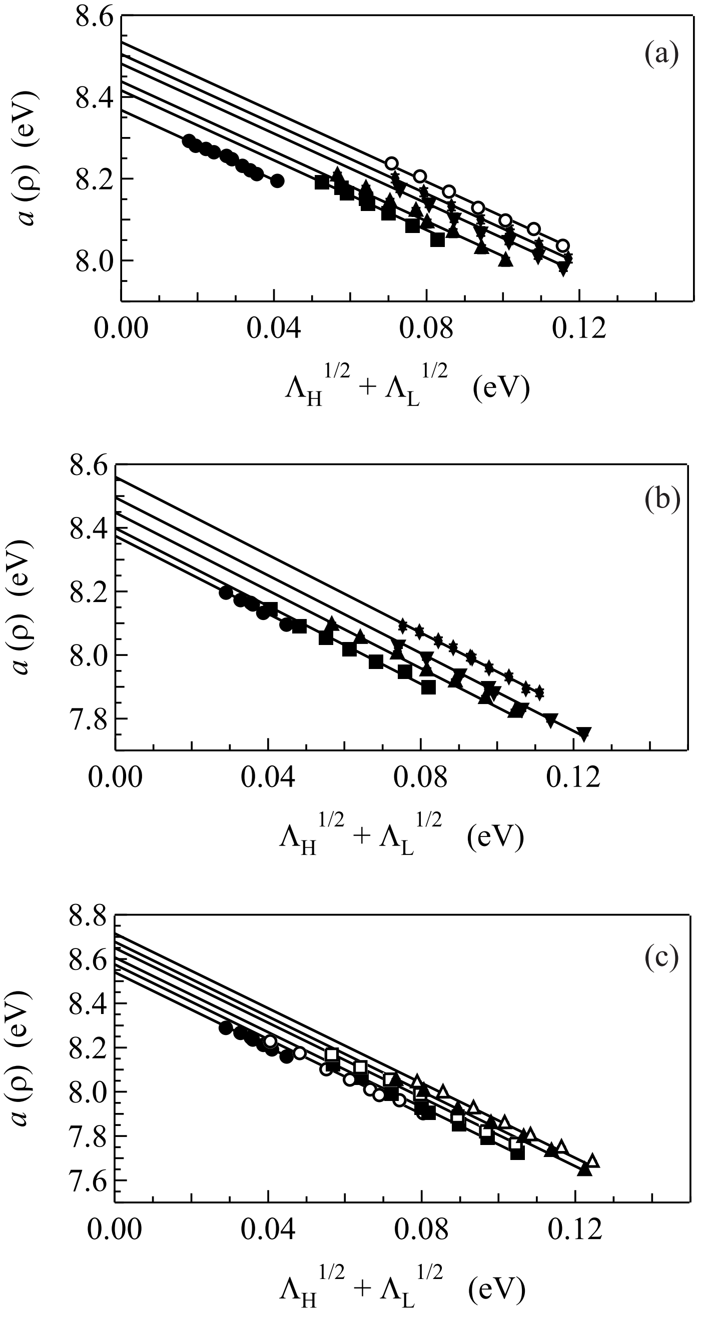

Figure 5.16: The FEP intercepts $a(\rho)$ of representative field enhanced photoemission plots measured at (a) 137.0 K, (b) 132.0 K, and (c) 127.0 K. In all graphs, (•) 0.6×10^{20} cm^{-3}. The density (10^{21} cm^{-3}) ranges are from (■) 2.0 to (○) 9.9 in (a); from (■) 1.0 to 11 in (b); and from (○) 1.1 to 9.9 in (c).

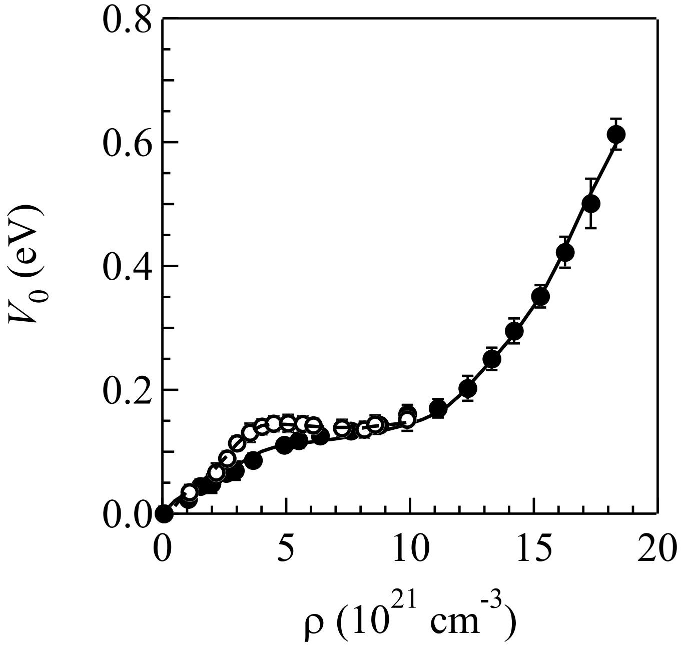

Figure 5.17: The quasi-free electron energy $V_0(\rho)$ in N_2 – determined from eq. (3.28) using field enhanced photoemission – plotted as a function of N_2 number density. The solid markers represent data obtained at noncritical temperatures, while the open markers represent data obtained at 127.0 K, which is near the critical temperature of 126.2 K. The lines are a local Wigner-Seitz calculation. See Section 5.2.1 for discussion.

one can see that the $V_0(\rho)$ predicted by Sakai *et al.* qualitatively agrees with our experimental data. Some features of the $V_0(\rho)$ curve are lost in their model, however, and no critical point effect is predicted.

Figs. 5.18a and 5.18b present the ensemble average electron/nitrogen polarization energy $P_-(\rho)$ and the zero-point kinetic energy $E_k(\rho)$ for the quasi-free electron in N_2 plotted as a function of number density, while the lines in Fig. 5.17 represent $V_0(\rho)$ obtained from eq. (3.33). Since many of the thermodynamic properties of N_2 across a broad temperature and density range can be modeled using a simple Lennard-Jones 6-12 potential [125–127], dense N_2 may be taken to be approximately spherical. Thus, we chose the electron/fluid interaction potential $w_-(r)$ in eq. (3.34) to be identical to that used by us in the successful modeling of $V_0(\rho)$ in previous

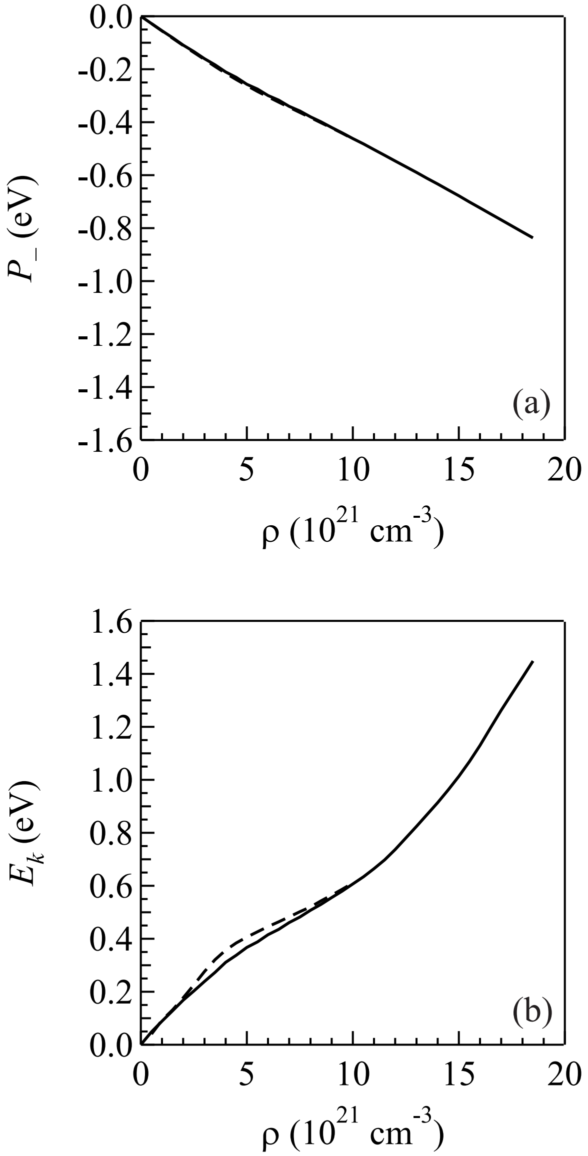

Figure 5.18: (a) The ensemble average electron/N_2 polarization energy $P_{-}(\rho)$ calculated from eq. (3.34) and (b) the zero-point kinetic energy $E_k(\rho)$ obtained from eq. (3.49) plotted as a function of N_2 number density ρ. The solid line represents calculations performed at noncritical temperatures and the dotted line represents those done at 127.0 K ($T_c = 126.2$ K). The N_2/N_2 interaction potential was modeled using a Lennard-Jones 6-12 potential [126], $A = 0.19$ Å [128], and $\eta_0 = 0.83$ [58]. See text for discussion.

atomic and molecular systems [49–55, 57], namely the potential given by eq. (3.35). The radial distribution function parameters were $\sigma = 3.656$ Å and $\epsilon/k_B = 98.94$ K. (Lemmon *et al.* [126] obtained these parameters from an optimization to N_2 viscosity data from low density to the density of the triple point liquid. We selected these parameters because they fit a broad data set [126] to within 2% of experiment.) The scattering length of $A = 0.19$ Å was obtained by Asaf *et al.* [128] from the shift of high-n CH_3I Rydberg states doped into low density N_2 gas. Optimizing η_0 for the best fit to the experimental $V_0(\rho)$ data in Fig. 5.17 gave $\eta_0 = 0.83$.

Clearly, the local Wigner-Seitz model accurately fits the experimentally determined quasi-free electron energy in N_2 at all temperatures. The significant curvature of $V_0(\rho)$ can be understood by comparing $P_-(\rho)$ in Fig. 5.18a with $E_k(\rho)$ in Fig. 5.18b. As was observed for repulsive gases (cf. Figs. 5.11 and 5.4, for example), the strictly positive $E_k(\rho)$ dominates the overall energetics. However, because of the larger polarizability of N_2 ($\alpha = 1.7403$ Å [129]), $P_-(\rho)$ is significantly larger than that of Ne (cf. Fig. 5.4a) and He (cf. Fig 5.11a). In the density range $5 - 10 \times 10^{21}$ cm^{-3}, $P_-(\rho)$ and $E_k(\rho)$ change with equal but opposite rates. Thus, $V_0(\rho)$ shows almost no variation as a function of density in this region.

The success of the local Wigner-Seitz model for $V_0(\rho)$ in both atomic [47,50–55,57] and molecular [49] fluids provides significant insight into the energetics of a quasi-free electron in a dense fluid. Whether $V_0(\rho)$ will be strictly positive, strictly negative, or neither is the result of the competition between the potential energy of polarization of the fluid by the quasi-free electron (i.e., $P_-(\rho)$) and the zero-point kinetic energy of the electron (i.e., $E_k(\rho)$). At high densities, $E_k(\rho)$ will always dominate the energetics, since the interaction range r_b for the quasi-free electron with a single fluid constituent in a high density fluid is small. However, in the low to medium density region, whether $E_k(\rho)$ or $P_-(\rho)$ dominates is subtly determined by a combination of the polarizability of the fluid, the interactions within the fluid as defined by the intermolecular potential, the scattering length of the fluid constituents, and the phase shift due to dynamic polarization in the first solent shell of the fluid.

For example, Ar and N_2 have similar polarizability volumes ($\alpha = 1.6411$ Å^3 for Ar [129] and $\alpha = 1.7403$ Å^3 for N_2 [129]) and, therefore, similar ensemble average electron/fluid polarization energies ($P_-(\rho) = -0.79$ eV [58] and -1.04 eV [50] at the triple point density of N_2 and Ar, respectively). However, $V_0(\rho)$ in argon [50–52, 55] is strictly negative, while that in N_2 is strictly positive. This difference in $V_0(\rho)$ is dominated by η_0, the phase shift arising from the dynamic polarization in the first solvent shell in the fluid. In Ar, $\eta_0 = 0.33$ [50–52, 55], whereas in N_2, $\eta_0 = 0.83$ [58]. In fact, we have observed that the attractive fluids tend to have $\eta_0 < 0.5$ [49–55], while repulsive fluids tend to have $\eta_0 > 0.6$ [47, 57]. Our group is currently in the process of developing molecular dynamics routines to calculate the quasi-free electron energy in order to probe the origin of the phase shift η_0.

While one would not expect the sign of the zero kinetic energy electron scattering length to determine whether the quasi-free electron energy is strictly positive or negative, since only $|A|$ is included in a local Wigner-Seitz calculation, the arguments in Chapter 2 qualitatively predict the sign of $V_0(\rho)$.

Chapter 6

Conclusion

This work presents the experimental and theoretical studies of the quasi-free electron energy $V_0(\rho)$ in Ne, He and N_2. Field ionization of O_2 was used to determine $V_0(\rho)$ in Ne. The field enhanced photoemission technique for directly measuring $V_0(\rho)$ was developed and used to obtain the quasi-free electron energy in He and N_2. Novel critical point effects were observed for the three fluids and were accurately calculated using the recently developed local Wigner-Seitz model.

Dopant field ionization was used to extract the quasi-free electron energy $V_0(\rho)$ from the field dependent shift in the ionization energy $\Delta(\rho)$ of the dopant dissolved in the fluid. $V_0(\rho)$ is extracted by subtracting the ensemble average polarization energy $P_+(\rho)$ of the dopant core in the fluid from $\Delta(\rho)$. Since $P_+(\rho)$ relies on the dopant/fluid and fluid/fluid radial distribution functions, an accurate determination of $V_0(\rho)$ is contingent on accurate dopant/fluid and neat fluid interaction potentials (which can present a problem). The need for an appreciable concentration of the dopant molecule to be reachable by the incoming photons poses another problem, as many repulsive fluids are either opaque to vacuum ultraviolet light or require very low temperatures to reach necessary number densities with pressures below 100 bar. We successfully determined $V_0(\rho)$ in Ne using field ionization, but attempts to apply this technique to He failed as we found it impossible to maintain dopant solubility past a He number density of 5×10^{21} cm^{-3}.

Thus, we developed field enhanced photoemission as a dopant free technique of directly determining $V_0(\rho)$. We utilized Fowler's equation for photoemission from a clean electrode in vacuum. However, unlike previous methods of obtaining $V_0(\rho)$ from this equation, field enhanced photoemission uses a difference of two photoemission spectra recorded at different applied electric fields. This method simplifies Fowler's equation to a linear relationship between the difference in spectra Δi_E and the energy of the incident radiation $h\nu$. The intercept $a(\rho)$ of the linear region with the energy axis yields the density dependent work function $\phi(\rho)$ augmented by the applied electric fields. Linear regression analyses of the intercepts recorded at specific fluid number densities produces the density dependent work functions $\phi(\rho)$. Subtracting the reference work function ϕ_0 from $\phi(\rho)$ gives $V_0(\rho)$. This method yields results with excellent precision, on a par with dopant field ionization. Unlike the results of previous photoemission studies of the quasi-free electron energy, the critical point effect on $V_0(\rho)$ is apparent in the results presented here.

The results in He, Ne and N_2 were accurately modeled using the local Wigner-Seitz approach. Within the local Wigner-Seitz model, the quasi-free electron energy $V_0(\rho)$ is given as a sum of the ensemble average adiabatic electron polarization energy $P_-(\rho)$, the zero-point kinetic energy of the electron $E_k(\rho)$ and the thermal correction $(3/2)k_BT$. The fluids presented in this work are a significant test of the local Wigner-Seitz model, since this approach was originally developed for attractive fluids. As was demonstrated in Chapter 5, the local Wigner-Seitz calculations of $V_0(\rho)$ for these fluids are in excellent agreement with experiment.

The increase in $V_0(\rho)$ around the critical point observed for attractive fluids is again seen in repulsive fluids. Increased fluid constituent clustering around the critical point causes an enhancement in the radial distribution function $g(r)$ which in turn produces a decrease in $P_-(\rho)$ and an increase in $E_k(\rho)$. However, the favorable effect on the polarization energy is minor because it is determined from an integration along the full range of $g(r)$. $E_k(\rho)$, on the other hand depends only on the first peak of $g(r)$. Thus the critical effect on $E_k(\rho)$ always dominates.

Unlike the quasi-free electron energy in attractive fluids, $V_0(\rho)$ in the repulsive fluids studied thus far is strictly positive. This is easily explained by recognizing that the smaller radii of the repulsive fluids produce a large positive $E_k(\rho)$, while the lower polarizability of these fluids ensures a small negative $P_-(\rho)$.

Fig. 6.1 presents the quasi-free electron energy in Ne, He and N_2 as a function of reduced fluid number density $\rho_r \equiv \rho/\rho_c$, with ρ_c being the critical density of the fluid. One can see that while the quasi-free electron energy is strictly positive and the positive critical point effect on $V_0(\rho)$ is observed in all three fluids, the shapes of the curves are very distinct. The subtle interplay of the electron polarization energy and the zero-point kinetic energy of the electron determines the shape. One can see that the smaller $E_k(\rho)$ in Ne and N_2, which possess smaller zero kinetic energy electron scattering lengths, ensures that the rise of $V_0(\rho)$ with respect to density is less rapid than it is for the more repulsive He. One can also observe that the density range on which the critical point effect is apparent is significantly broader in He.

We have developed field enhanced photoemission to allow for the collection of precise quasi-free electron energy measurements in very repulsive and opaque fluids.

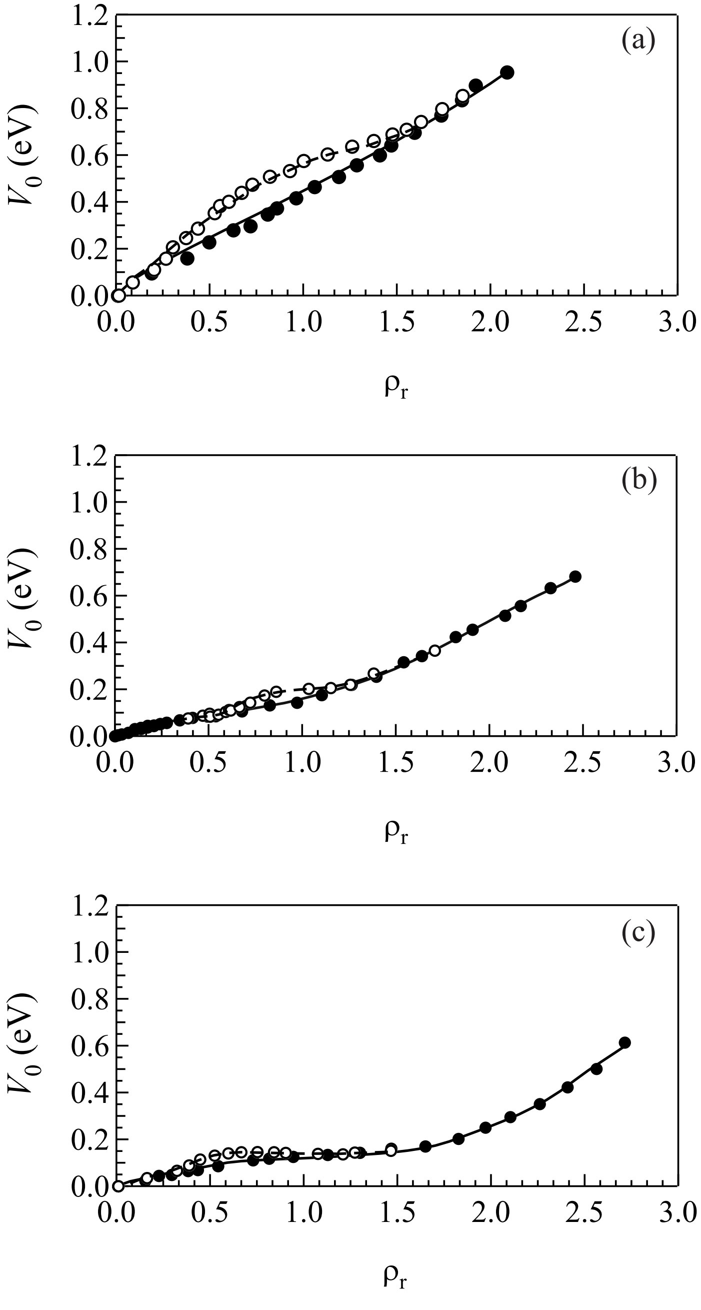

Figure 6.1: The quasi-free electron energy $V_0(\rho)$ in (a) He [47], (b) Ne [57], and (c) N_2 [58] plotted versus reduced density $\rho_r \equiv \rho/\rho_c$. Solid markers represent data obtained on noncritical isotherms while open markers represent data obtained on an isotherm near the critical isotherm. The lines are a local Wigner-Seitz calculation.

We have also shown that the local Wigner-Seitz approach is an excellent way to model $V_0(\rho)$ in these fluids. Now that a reliable measurement technique exists, our group shall move on to determining $V_0(\rho)$ in the diatomic hydrogen series (i.e., H_2, D_2 and HD) as well as in polar fluids CO, NO, NO_2 and N_2O. The hydrogen series could not have been studied with field ionization since introducing a reactive dopant molecule (O_2 would be the only possible dopant) into high density hydrogen under a high electric field is problemmatic. We are curious as to whether an isotope effect on the quasi-free electron energy will be observed, as well as to whether or not the fermionic nature of HD will produce a change in $V_0(\rho)$. The polar diatomic molecules also could not have been studied in the past because they are strong absorbers in the vacuum ultraviolet spectral range.

No changes to the experimental method will be required in these subsequent studies. The theoretical approach, however, will likely have to be altered in order to model $V_0(\rho)$ in polar fluids. The excess electron will polarize the fluid, changing the orientation of polar molecules and thus requiring a more complex electron/fluid interaction potential than that described by eq. (3.35). However, one might be able to simplify the problem by applying a large electric field, thereby ensuring a molecular orientation in the fluid that is largely unperturbed by the excess electron. Then, the interaction potential for a polar diatomic molecule could be expressed as a sum of electron/partially negative atom and electron/partially positive atom interaction potentials. Once $g(r)$ for polar fluids is correctly modeled, it is possible that the zero-point kinetic energy of the electron could be calculated in the same manner it is for atoms and nonpolar molecules, provided that the zero energy electron scattering length of the polar molecule is known.

More sophisticated computer simulation methods of determining radial distribution functions may be required for polar molecules. As the molecular geometry of the fluids becomes more complicated, the screening functions and radial distribution functions will become increasingly difficult to calculate using integral methods. At that point, it will likely be simpler to calculate the ensemble average polarization energy of the excess electron using molecular dynamics. Of course, an agreement will have to be reached between the new calculation results, the experimental data and previous local Wigner-Seitz calculations. Studies of $V_0(\rho)$ in Ar and in He will be performed using molecular dynamics to ensure that the results are consistent with previous findings and the findings presented here.

Once a new calculation technique is established, we can begin to probe the energetics of more complicated fluids with the added benefit of being able to study fluid cavity formation (cf. Section 3.3.2). The predicted energy of the electron cavity could then be verified with infrared measurements. Additionally, computational studies of the solvated electron should shed some light onto the nature of the dynamic polarization phase shift η_0, which at this point is determined empirically.

References

[1] C. L. Phelps, N. G. Smart and C. M. Wai, "Past, present, and possible future applications of supercritical fluid extraction technology,"J. Chem Ed. 73, 1163 (1996), and references therein.

[2] J. R. Dean, ed., *Applications of Supercritical Fluids in Industrial Analysis* (Springer, New York, 1998), and references therein.

[3] E. Kiran and J. F. Brennecke, ed., *Supercritical Fluid Engineering Science*, No. 514 in *ACS Symposium Series* (American Chemical Society, Washington, D.C., 1995).

[4] E. Kiran, P. G. Debenedetti, and C. J. Peters, ed., *Supercritical Fluids: Fundamentals and Applications* (Springer-Verlag, Berlin, 2008).

[5] K. W. Hutchenson and N. R. Foster, ed., *Innovations in Supercritical Fluids*, No. 608 in *ACS Symposium Series* (American Chemical Society, Washington, D.C., 1995).

[6] L. B. Davenhall and J. B. Rubin, "Composition and method for removing photoresist materials from electronic components," Patent No. US 6,403,544 B1.

[7] P. York," Strategies for particle design using supercritical fluid technologies," PSTT 2, 430 (1999).

[8] J. R. Williams and T. Clifford, eds., *Supercritical Fluids: Methods and Protocols* (Humana Press, New Jersey, 2000), and references therein.

[9] T. J. Bruno and J. F. Ely, ed., *Supercritical Fluid Technology: Reviews in Modern Theory and Applications* (CRC, Boca Raton, 1991).

[10] A. S. Gopalan, C. M. Wai and H. K. Jacobs, ed., *Supercritical Carbon Dioxide: Separations and Processes*, No. 860 in *ACS Symposium Series* (American Chemical Society, Washington, D.C., 2003).

[11] R. Noyori, "Supercritical fluids: introduction," Chem. Rev. 99, 353 (1999).

[12] J. R. Dean, ed., *Extraction Methods for Environmental Analysis* (Wiley, New York, 1998), and references therein.

[13] P. R. Loconto, ed., *Trace Environmental Quantitative Analysis: Principles, Techniques and Applications* (Marcel Dekker, New York, 2001), and references therein.

[14] S. A. Westwood, ed., *Supercritical Fluid Extraction and its use in Chromoatographic Sample Preparation* (Springer-Verlag, Berlin, 2007).

[15] V. K. Jain, "Supercritical Fluids Tackle Hazardous Wastes," Env. Sci. Tech. 27, 806 (1993).

[16] K. Anton and C. Berger, eds., *Supercritical Fluid Chromatography with Packed Columns* (Marcel Dekker, New York 1997), and references therein.

[17] M. Poliakoff, J. M. Fitzpatrick, T. R. Farren, and P. T. Anastas, "Green Chemistry: Science and Politics of Change," Science 297, 807 (2002).

[18] I. T. Horváth and P. T. Anastas, "Introduction: green chemistry." Chem. Rev. 107, 2167 (2007).

[19] I. T. Horváth and P. T. Anastas, "Innovations and green chemistry," Chem. Rev. 107, 2169 (2007).

[20] L. H. Keith, L. U. Gron, and J. L. Young, "Biocatalysis in Supercritical Fluids, in Fluorous Solvents, and under Solvent-Free Conditions," Chem. Rev. 107, 2695 (2007).

[21] Y. -Pi Sun, ed., *Supercritical Fluid Technology in Material Science and Engineering: Synthesis, Properties and Applications* (Dekker, New York, 2002).

[22] Y. Arai, T. Sako, and Y. Takebayashi, ed., *Supercritical Fluids: Molecular Interactions, Physical Properties, and New Applications* (Springer-Verlag, Berlin, 2002).

[23] J. P. Cason, K. Khambaswadkar, and C. B. Roberts,"Supercritical Fluid and Compressed Solvent Effects on Metallic Nanoparticle Synthesis in Reverse Micelles," Ind. Eng. Chem. Res. 39, 4749 (2000).

[24] Y. Zhang and C. Erkey, J. Supercritical Fluids 38, 252 (2006), and references therein.

[25] I. Pasquali, R. Bettini and F. Giordano, "Supercritical fluid technologies: An innovative approach for manipulating the solid-state of pharmaceuticals," Adv. Drug Delivery Rev. 60, 399 (2008), and references therein.

[26] I. Pasquali, R. Bettini and F. Giordano, "Solid-state chemistry and particle engineering with supercritical fluids in pharmaceutics," European J. of Pharmaceutical Sciences 27, 299 (2006), and references therein.

[27] J. F. Brennecke and J. E. Chateauneuf,"Homogeneous Organic Reactions as Mechanistic Probes in Supercritical Fluids," Chem. Rev. 99, 433 (1999).

[28] S. A. Egorov and E. Rabani, "Chemical equilibrium in supercritical fluids: Solvent effects on the dimerization equilibrium constant," J. Chem. Phys. 116, 8447 (2009).

[29] S. C. Tucker, "Solvent Density Inhomogeneities in Supercritical Fluids," Chem. Rev. 99, 391 (1999), and references therein.

[30] I. T. Steinberger, in: *Electronic Excitations in Liquefied Rare Gases*, W. F. Schmidt, E. Illenberger, ed. (Am. Sci. Publ., Valencia, 2005), and references therein.

[31] A. K. Al-Omari, *Field Ionization as a Technique to Determine Electronic Properties of Fluids*, Ph.D. dissertation, University of Wisconsin Madison, Madison, WI, 1996, and references therein.

[32] R. Reininger, U. Asaf, I. T. Steinberger, S. Basak, "Relationship between the energy V_0 of the quasi-free-electron and its mobility in fluid argon, krypton, and xenon," Phys. Rev. B 28, 4426 (1983).

[33] A. O. Allen, W. F. Schmidt, "Determination of the energy level V_0 of electrons in liquid argon over a range of densities," Z. Naturforsch. 37a, 316 (1982).

[34] W. von Zdrojewski, J. G. Rabe, W. F. Schmidt, "Photoelectric determination of V_0-values in solid rare gases," Z. Naturforsch. 35a, 672 (1980).

[35] B. Halpern, J. Lekner, S. A. Rice, R. Gomer, "Drift velocity and energy of electrons in liquid argon," Phys. Rev. 156, 351 (1967).

[36] W. Tauchert, H. Jungblut, W. F. Schmidt, "Photoelectric determination of V_0 values and electron ranges in some cryogenic liquids," Can. J. Chem. 55, 1860 (1977).

[37] R. Reininger, U. Asaf, I. T. Steinberger, "The density dependence of the quasi-free electron state in fluid xenon and krypton," Chem. Phys. Lett. 90, 287 (1982).

[38] A. K. Al-Omari, K. N. Altmann, R. Reininger, "Determination of the conduction band energy minimum in fluid argon by means of field ionization," J. Chem. Phys. 105, 1305 (1996).

[39] A. K. Al-Omari, R. Reininger, "Density dependence of the ionization potential of H_2S in argon," J. Electron Spectrosc. Relat. Phenom. 79, 463 (1996).

[40] A. K. Al-Omari, R. Reininger, "Density dependence of the ionization potential of CH_3I in krypton and of the quasi-free electron energy in krypton," J. Chem. Phys. 103, 4484 (1995).

[41] A. K. Al-Omari, R. Reininger, "Density dependence of the ionization potential of CH_3I in argon and of the quasi-free electron energy in argon," J. Chem. Phys. 103, 506 (1995).

[42] K. N. Altmann, R. Reininger, "Density dependence of the conduction-band minimum in fluid krypton and xenon from field ionization of $(CH_3)_2S$," J. Chem. Phys. 107, 1759 (1997).

[43] J. Meyer, R. Reininger, "Electric-field ionization of high Rydberg states and vertical ionization potential of an impurity in dense fluid argon," Phys. Rev. A 47, R3491 (1993).

[44] J. Meyer, *Elektronische Eigenschaften Dotierter Gase und Flüssigkeiten* (Electronic Properties of Dense Gases and Liquids), Ph.D. dissertation, Universität Hamburg, 1992, and references therein.

[45] Xianbo Shi, *Energy of the quasi-free electron in atomic and molecular fluids*, Ph.D. dissertation, Graduate Center – CUNY (2010), and references therein.

[46] Y. Lushtak, C.M. Evans and G.L. Findley, "Field enhanced photoemission: a new technique for the direct determination of the quasi-free electron energy in dense fluids,"Chem. Phys. Lett. 515, 190 (2011).

[47] Y. Lushtak, Samantha Dannenberg, “Quasi-free electron energy in near critical point helium,” C.M. Evans and G.L. Findley, Chem. Phys. Lett. 538, 46 (2012).

[48] Xianbo Shi, Luxi Li, Gina M. Moriarty, C. M. Evans, G. L. Findley, “Energy of the quasi-free electron in low density Ar and Kr: extension of the local Wigner-Seitz model,” Chem. Phys. Lett. 454, 12 (2008).

[49] X. Shi, L. Li, G. L. Findley, C. M. Evans, “Energy of the excess electron in methane and ethane near the critical point,” Chem. Phys. Lett. 481, 183 (2009).

[50] C. M. Evans, G. L. Findley, “Energy of the quasi-free electron in argon and krypton,” Phys. Rev. A 72, 022717 (2005).

[51] C. M. Evans, G. L. Findley, “Energy of the quasi-free electron in supercritical argon near the critical point,” Chem. Phys. Lett. 410, 242 (2005).

[52] C. M. Evans, G. L. Findley, “Field ionization of C_2H_5I in supercritical argon near the critical point,” J. Phys. B: At. Mol. Opt. Phys. 38, L269 (2005).

[53] Luxi Li, C. M. Evans, G. L. Findley, “Energy of the quasi-free electron in supercritical krypton near the critical point,” J. Phys. Chem. A 109, 10683 (2005).

[54] Xianbo Shi, Luxi Li, C. M. Evans, G. L. Findley, “Energy of the quasi-free electron in xenon,” Chem. Phys. Lett. 432, 62 (2006).

[55] Xianbo Shi, Luxi Li, C. M. Evans, G. L. Findley, “Energy of the quasi-free electron in argon, krypton and xenon,” Nucl. Inst. Meth. A 582, 270 (2007).

[56] C. M. Evans, Y. Lushtak, X. Shi, L. Lo, G. L. Findley, “Temperature effects on the perturber induced shift of dopant ionization energies in He and Ne,” Chem. Phys. Lett. 505, 16 (2011).

[57] C. M. Evans, Y. Lushtak and G. L. Findley, “Energy of the quasi-free electron in dense neon,” Chem. Phys. Lett. 501, 202 (2011).

[58] Y. Lushtak, C. M. Evans and G. L. Findley, “The energy of the quasi-free electron in near critical point nitrogen,” Chem. Phys. Lett. 546, 18 (2012).

[59] D. F. Coker, B. J. Berne, D. Thirumalai, “Path integral Monte Carlo studies of the behavior of excess electrons in simple fluids,” J. Chem. Phys. 86, 5689 (1987).

[60] J. Jornter, A. Gaathon, “Effects of phase density on ionization processes and electron localization in fluids,” Can. J. Chem. 55, 1801 (1977).

[61] C. E. Krohn, J. C. Thompson, “Comments on electronic energy levels for photoinjection into polar fluids,” Phys. Rev. B 20, 4365 (1979).

[62] U. Schindewolf, “Physical and chemical properties of dissolved electrons (excess electrons),” Angew. Chem. Int Ed. Engl. 17, 887 (1978).

[63] B. E. Springett, J. Jortner, M.H. Cohen, “Stability criterion for the localization of an excess electron in a nonpolar fluid,” J. Chem. Phys. 48, 2720 (1968).

[64] J. Levine, T. M. Sanders Jr."Anomalous electron mobility and complex negative ion formation in low-temperature helium vapor," Phys. Rev. Lett. 8, 159 (1962).

[65] J. L. Levine, T. M. Sanders Jr., "Mobility of electrons in low-temperature helium gas," Phys. Rev. 154, 138 (1967).

[66] A. R. P. Rau, in *Photophysics and Photochemistry in the Vacuum Ultraviolet*, edited by S. P. McGlynn, G. L. Findley and R. H. Huebner (D. Reidel Publishing Company, 1985), and references therein.

[67] E. Fermi, "Sopra lo spostamento per pressione delle righe elevate delle serie spettrali (Concerning the shift of the high lines of spectral series due to pressure effects)," Nuovo Cimento 11 157 (1934).

[68] V. A. Alekseev, I. I. Sobel'man, "A spectroscopic method for the investigation of elastic scattering of slow electrons," Zh. Eksp. Teor. Fiz. 49, 1274 (1965).

[69] A. M. Köhler, R. Reininger, V. Saile, G. L. Findley, "Density effects on high-n molecular Rydberg states: CH_3I in He, Ne, Ar and Kr," Phys. Rev. A 35, 35 (1987).

[70] A. M. Köhler, V. Saile, R. Reininger, G. L. Findley, "Sudden and adiabatic polarization effects in doped rare gases," Phys. Rev. Lett. 60, 2727 (1988); errata 61, 1327 (1988).

[71] U. Asaf, W. S. Felps, K. Rupnik, S. P. McGlynn, G. Ascarelli, "Density effects on high-n molecular Rydberg states: CH_3I and C_6H_6 in H_2 and Ar," J. Chem. Phys. 91, 5170 (1989).

[72] U. Asaf, J. Meyer, R. Reininger, I. T. Steinberger, "High Rydberg states of methyl iodide perturbed by nitrogen: a mutual cancellation of shift terms," J. Chem. Phys. 96, 7885 (1992).

[73] J. Meyer, R. Reininger, U. Asaf, "Spectral shift of autoionizing high-n Rydberg states of iodomethane in dense argon: a photoionization study," Chem. Phys. Lett. 173, 384 (1990).

[74] J. Meyer, R. Reininger, U. Asaf, I. T. Steinberger, "Autoionization spectra of CH_3I in dense gaseous methane, ethane, and propane observed by photoconduction," J. Chem. Phys. 94, 1820 (1991).

[75] U. Asaf, I. T. Steinberger, J. Meyer, R. Reininger, "Electron scattering in dense CO_2 gas: photoionization spectra of CH_3I perturbed by CO_2," J. Chem. Phys. 95, 4070 (1991).

[76] C. M. Evans, *Subthreshold Photoionization in Molecular Dopant/perturber Systems*, Ph.D. dissertation, Louisiana State University, 2001, and references therein. See also C. M. Evans, J. D. Scott, G. L. Findley, Rec. Res. Dev. Chem. Phys. 3, 351 (2002).

[77] I. T. Steinberger, U. Asaf, G. Ascarelli, R. Reininger, G. Reisfeld, M. Reshotko, "Extrinsic photoconduction and Rydberg states due to a methyl iodide impurity in xenon," Phys. Rev. A 42, 3135 (1990).

[78] I. Messing, J. Jortner, "Adiabatic polarization energy in a simple dense fluid," Chem. Phys. 24, 183 (1977).

[79] E. Wigner, F. Seitz, "On the constitution of metallic sodium," Phys. Rev. 43, 804 (1933).

[80] E. Wigner, F. Seitz, "On the constitution of metallic sodium. II," Phys. Rev. 46, 509 (1934).

[81] Thomas F. Miller III, "Isomorphic classical molecular dynamics model for an excess electron in a supercritical fluid", J. Chem. Phys, 129 194502 (2008).

[82] A. M. Köhler, *Density Effects on Rydberg States and Ionization Energies of Molecules*, Ph.D. Dissertation, Universität Hamburg, Hamburg, Germany, 1987, and references therein.

[83] E. W. Grundke, D. Henderson, R. D. Murphy, "Evaluation of the Percus-Yevick theory for mixtures of simple liquids," Can. J. Phys. 51, 1216 (1973).

[84] J. Lekner, "Motion of electrons in liquid argon," Phys. Rev. 158, 130 (1967).

[85] A. K. Al-Omari, R. Reininger, D. L. Huber, "Polarization energy distribution of a positive ion in liquid argon," Phys. Rev. Lett. 74, 820 (1995).

[86] A. K. Al-Omari, R. Reininger, D. L. Huber, "Polarization energy distribution for impurity molecules in dense gases," J. Chem. Phys. 109, 7663 (1998).

[87] J. G. Kirkwood, "Statistical mechanics of fluid mixtures," J. Chem. Phys. 3, 300 (1935).

[88] B. E. Springett, J. Jortner, M. H. Cohen, "Stability criterion for the localization of an excess electron in a nonpolar fluid," J. Chem. Phys. 48, 2720 (1968).

[89] B. Plenkiewicz, P. Plenkiewicz, J. -P. Jay-Gerin, "Conduction-band energy V_0 of an excess electron in liquid krypton," Phys. Rev. A. 39, 2070 (1989).

[90] B. Plenkiewicz, J. -P. Jay-Gerin, P. Plenkiewicz, G. B. Bachelet, "Conduction band energy of excess electrons in liquid argon," Europhys. Lett. 1, 455 (1986).

[91] J. Meyer, R. Reininger, "Electric-field ionization of high Rydberg states and vertical ionization potential of an impurity in dense fluid argon," Phys. Rev. A 47, R3491 (1993).

[92] E. Guth and C. J. Mullin, "Electron Emission of Metals in Electric Fields I. Explanation of the Periodic Deviations from the Schottky Line," Phys. Rev. 59 575 (1941).

[93] E. Guth and C. J. Mullin, "Electron Emission of Metals in Electric Fields II. Field Dependence of the Surface Photo-Effect," Phys. Rev. 59, 867 (1941).

[94] R. H. Fowler, "The analysis of photoelectric sensitivity curves for clean metals at various temperatures," Phys. Rev. 38, 45 (1931).

[95] Ashcroft, N. David Mermin, *Solid State Physics* (Brooks/Cole Belmont, CA, 2010).

[96] L. A. Dubridge, "The Photoelectric and Thermionic Work Funciton of Outgassed Platinum," Phys. Rev. 31, 236 (1928).

[97] H. S. W. Massey, E. H. S. Burhop, *Electronic and Ionic Impact Phenomena Vol. 1* (Clarendon Press, Oxford, 1969).

[98] P. Attard, "Spherically inhomogeneous fluids. I. Percus-Yevick hard spheres: osmotic coefficients and triplet correlations," J. Chem. Phys. 91, 3072 (1989).

[99] T. R. Strobridge, "The thermodynamic properties of nitrogen from 64 to 300 K between 0.1 and 200 atmospheres," Tech. Note 129, Nat. Bur. Std. (U.S.) (1962).

[100] R. D. McCarty and R. B. Stewart, "Advances in thermophysical properties at extreme temperatures and pressures," Papers Presented at Symposium on Thermophysical Properties 84 (1965).

[101] A. L. Gosman, R. D. McCarty, J. G. Hust, "Thermodynamic properties of argon from the triple point to 300 °K at pressures to 1000 atmospheres," Tech. Note 27, Nat. Bur. Std. (U.S.) (1969).

[102] R. D. McCarty, "Thermodynamic properties of helium-4 from 2 to 1500 K at pressures to 108 Pa," J. Phys. Chem. Ref. Data 2, 923 (1973).

[103] R. T. Jacobsen, R. B. Stewart, M. Jahangiri, "Thermodynamic properties of nitrogen from the freezing line to 2000 K at pressures to 1000 MPa," J. Phys. Chem. Ref. Data 15, 735 (1986).

[104] E. B. Gordon and B. M. Smirnov, "Processes in condensed inert gases involving excess electrons," J. Exp. Theor. Phys. 98, 924 (2004).

[105] A. Henglein, "Electron reactivity as a function of phase," Can. J. Chem. 55, 2112 (1977).

[106] F. M. Mourits, F. H. A. Rummens, "A critical evaluation of LennardJones and Stockmayer potential parameters and of some correlation methods," Can. J. Chem. 55, 3007 (1977).

[107] P. T. Sikora, "Combining rules for spherically symmetric intermolecular potentials," J. Phys. B: At. Mol. Opt. Phys. 3, 1475 (1970).

[108] A. Garcia-Vela, J. Rubayo-Soneira, G. Delgado-Barrio, and P. Vilarreal, "Quasiclassical dynamics of the I_2-Ne_2 vibrational predissociation: A comparison with experiment," J. Chem. Phys. 104, 8405 (1996).

[109] Encycloaedia Britannica: noble gas. http://www.britannica.com/EBchecked/topic/416955/noble-gas (accessed Jan 17, 2013).

[110] U. Asaf and I. T. Steinberger, "The energies of excess electrons in helium," Chem. Phys. Lett. 128, 91 (1986).

[111] W. T. Sommer, "Liquid helium as a barrier to electrons," Phys. Rev. Lett. 12, 271 (1964).

[112] M. A. Woolf and G. W. Rayfield, "Energy of negative ions in liquid helium by photoelectric injection," Phys. Rev. Lett. 15, 235 (1965).

[113] J. A. Northby and J. T. M Sanders, "Photoejection of electrons from bubble states in liquid helium," Phys. Rev. Lett. 18, 1184 (1967).

[114] T. Miyakawa and D. L. Dexter, "Interpretation of photoejection experiments and the well depth of electronic bubbles in liquid helium," Phys. Rev. A 1, 513 (1970).

[115] D. G. Onn and M. Silver, "Injection and thermalization of hot electrons in solid, liquid, and gaseous helium at low temperatures," Phys. Rev. A. 3, 1773 (1971).

[116] W. Schoepe and G. W. Rayfield, "Tunneling from electronic bubble states in liquid helium through the liquid-vapor interface," Phys. Rev. A 7, 2111 (1973).

[117] P. Marchand and L. Marmet, "Binomial smoothing filter: A way to avoid some pitfalls of least squares polynomial smoothing," Rev. Sci. Inst. 54, 1034 (1983).

[118] R. A. Aziz, V. P. S. Nain, J. S. Carley, W. L. Taylor, G. T. McConville, "Accurate intermolecular potential for helium," J. Chem. Phys. 70, 4330 (1979).

[119] D. A. Young, A. K. McMahan, M. Ross, "Equation of state and melting curve of helium to very high pressure," Phys. Rev. B 24, 5119 (1981).

[120] H. P. Saha, "*Ab initio* calculation of scattering length and cross sections at very low energies for electron-helium scattering," Phys. Rev. A 48, 1163 (1993), and references therein.

[121] Y. Sakai, W. F. Schmidt, A. G. Khrapak, "Self-trapping of electrons in liquid nitrogen," IEEE Trans. Dielec. Elec. Ins. 1, 4 (1994).

[122] L. Frommhold, "Resonance scattering and the drift motion of electrons through gases," Phys. Rev. 172, 118 (1968).

[123] T. Wada, G. R. Freeman, "Electron localization in dense nitrogen vapor," J. Chem. Phys. 72, 6726 (1980).

[124] N. Gee, M. A. Floriano, T. Wada, S. S. S. Huang, G. R. Freeman, "Ion and electron mobilities in cryogenic liquids: Argon, nitrogen, methane, and ethane," J. Appl. Phys. 57, 1097 (1985).

[125] J. G. Powles, K. E. Gubbins, "The intermolecular potential for nitrogen," Chem. Phys. Lett. 38, 405 (1976).

[126] E. W. Lemmon, R. T. Jacobsen, "Viscosity and thermal conductivity equations for nitrogen, oxygen, argon, and air," Int. J. Thermophys. 25, 21 (2004).

[127] A. Elkamel, R. D. Noble, "A statistical mechanics approach to the separation of methane and nitrogen using capillary condensation in a microporous membrane," J. Membrane Sci. 65, 163 (1992).

[128] U. Asaf, J. Meyer, R. Reininger, I. T. Steinberg, “High Rydberg states of methyl iodide perturbed by nitrogen: A mutual cancellation of shift term,” J. Chem. Phys. 96, 7885 (1992).

[129] R. H. Orcutt, R. H. Cole, “Dielectric constants of imperfect gases. III. atomic gases, hydrogen, and nitrogen,” J. Chem. Phys. 46, 697 (1967).